ANNUAL TRANSACTIONS

THE NORDIC RHEOLOGY SOCIETY

VOLUME 33
2025

PAPERS PRESENTED AT

Joint Conference of

THE NORDIC RHEOLOGY SOCIETY

and

THE GERMAN RHEOLOGICAL SOCIETY

at the Bundesanstalt für Materialforschung und -prüfung (BAM) in Berlin,

June 10- 12, 2025

Editor: Herimonja A. Rabenjafimanantsoa

THE NORDIC RHEOLOGY SOCIETY

The Nordic Rheology Society engages people interested in rheology in the Nordic countries. The society has approximately 140 members. The objective of the society is to promote and propagate rheology at all levels by building a broad forum where academia and industry, in their applicational and theoretical guises can meet, share and discuss ideas to their mutual benefit. The Nordic Rheology Society represents the Nordic countries in the International Committee of Rheology (ICR).

The elected officers of the society are:

President:
Dr. Olli-Ville Laukkanen, Research Scientist, VTT Technical Reaserch Center, Finland.

Secretary:
Dr. Norbert Raak, University of Copenhagen, Denmark.

Treasurer:
Kasra Amini, KTH Royal Institute of Technology, Sweden.

ICR-representative:
Prof. Roland Kádár, Chalmers University of Technology, Sweden.

For further information about the Nordic Rheology Society and membership application please contact:

Dr. Olli-Ville Laukkanen, Research Scientist, VTT Technical Reaserch Center, Finland.
Email: nrs@nordicrheologysociety.org

Website: nordicrheologysociety.org

ISBN 978-82-692721-6-1
ISSN 1601-4057

Preface

This issue of this 33rd volume of the *Annual Transactions of the Nordic Rheology Society* (ATNRS) comprises the papers and posters presented at the joint conference organized by the Nordic Rheology Society (NRS) and the Deutsche Rheologische Gesellschaft (DRG) in Berlin in June 10-12, 2025. The aim was to gather rheologists and enhance the exchange of knowledge between researchers, users, application specialists and instrumentation manufacturers in the Nordic countries, Germany and beyond.

The conference organizing commitee consisted of Prof. Ulrich Handge, Dr. Olli-Ville Laukkanen, Prof. Mats Stading,and Prof. Roland Kádár from TU Dortmund, VTT Finland, RISE & Chalmers University in Sweden, and Chalmers University in Sweden, respectively. The conference secretaries and contact were assured by Karolina Alibegovic from Bundesanstalt für Materialforschung und -prüfung (BAM), Germany and Norbert Raak from University of Copenhagen, Denmark.

The plenary lecture was given by Prof. Maria Charalambides who is a Professor in Mechanics of Materials at the Department of Mechanical Engineering at Imperial College London.

The year's Annual Business Meeting of the society was held in Gelber Saal.

A short course for everyone interested in rheology was conducted on the morning of June 10th. The course was held by Dr.-Ing. Joachim Kaschta and Prof. Andreas Wierschem. A good knowledge of the fundamentals of rheology were given which were considered to make it easier on "How to identify and to avoid measurement errors".

This year the Carl Klason Award was given to Prof. Mats Stading for his tireless contributions to the basic understanding of rheological phenomena and to the application of rheology. His lecture on "From fluid to solid research" is also inserted in this issue.

This year's Young Rheologist was awarded to Julie Frost Dahl. This award is given to a young person, who has made outstanding work in basic or applied rheology at the graduate or postgraduate level. Her lecture on "Measure, understand and predict structure formation in anisotropic plant-based foods - using rheology" is also included in this issue.

The present volume contains 11 oral and 2 poster submissions from Nordic countries and worldwide. The received contributions are divided according to the conference sessions into 'Advances in Rheological Methods', 'Suspensions, Composites, and Multiphase Materials', 'Food and Biopolymer Rheology', 'Polymer Rheology', 'Biopolymer Rheology', 'Engineering Rheology', 'Non-Newtonian Fluid Mechanics' and 'Poster Presentations'. The manuscripts will be accessible online as PDF files on the website: `https://nordicrheologysociety.org/AnnualTransactions/`.

Finally, in editing this Annual Transaction, I would like to extend my appreciation to the contributors of the present volume, the reviewers, the sponsors, exhibitors, chair of the sessions, and the society's board members for their contributions, help and cooperation. I would also like to thank our plenary lecturer for her contribution.

The preparation of this volume was made using LaTeX processing code.

Dr. Herimonja A. Rabenjafimanantsoa
University of Stavanger
Norway
May 2025

Contents 2025

Keynote Speaker

Carl Klason Rheology Award Lecture

NRS Young Rheologist Award Lecture

Advances in Rheological Methods

Suspensions, Composites, and Multiphase Materials

Food and Biopolymer Rheology

Polymer Rheology

Biopolymer Rheology

Engineering Rheology

Non-Newtonian Fluid Mechanics

Poster Presentations

Keynote Speaker

Developing enabling tools for design of better, healthier and tastier food products

Maria Charalambides

Department of Mechanical Engineering, Imperial College London, UK

m.charalambides@imperial.ac.uk

Foods are amongst the most complex materials that one can study in terms of material mechanics. Yet if we are to deliver innovations in food production, we need understanding for how such complex materials behave rheologically under various loading and environmental conditions (strain rate/time, temperature). Only then we can provide solutions to the several, pressing challenges related to food, including a shift to sustainable, nutritious and enjoyable food products with a lower environmental impact, healthier human outcomes and positive sensory perceptions.

This talk will summarise our research related to the human digestion process of starch based foods which crucially affects the rate of release of nutrients in the gastrointestinal tract. We show how constitutive laws are calibrated through independent tests and then used as inputs in Finite Element (FE) models to simulate food structure breakdown during the gastric process. Parameters related to diffusion, reaction and mechanical deformation parameters are calibrated using experimental data. Peristaltic waves are simulated via displacement boundary conditions on the stomach wall, while chemical loading is represented by a mass field of gastric fluids.

Furthermore, our studies related to the food oral process of chocolate will be presented. We show how microstructure can impact the macroscopic response and the whole sequence of events during the oral process, providing physical insight towards understanding consumer sensory perception of this popular product.

Maria Charalambides

Maria Charalambides (PhD, DIC, CEng, FIMechE) is a Professor in Mechanics of Materials at the Department of Mechanical Engineering at Imperial College London. She is the current President of British Society of Rheology. Amongst Maria's research interests is mechanics of soft solids and particulate polymeric composites, rheological characterisation and modelling of soft solids found in various applications such as in foods, plastic bonded and granular explosives, paints and plastics in art conservation, adhesives, foams and mechanical recycling of plastic packaging. She leads the Soft Solids research group. Maria has published over 100 papers and has received funding from both industry and Research Councils UK. Her published research includes material modelling and mechanical characterisation, micromechanics models of particulate filled composites as well as cellular and porous structures, experimental and numerical modelling of industrial food processes as well as oral and gastric processes and fracture and deformation in paint and adhesive coatings.

Carl Klason Rheology Award Lecture

FROM FLUID TO SOLID RESEARCH

Mats Stading[1,2]

[1]RISE Research Institutes of Sweden, Gothenburg, Sweden
[2]Chalmers University of Technology, Gothenburg, Sweden

ABSTRACT

Rheology offers profound insights into various applications, from healthcare to environmental sustainability. This contribution explores the role of rheology in understanding biobased fluids, gels and solid melts. In the context of fluids, rheology e.g. helps addressing swallowing difficulties in the aging population by adjusting the viscosity of beverages to the impaired bodily swallowing functions. Experimental instruments such as the Gothenburg Throat Model helps analysing fluid rheology during swallowing and non-invasive nano-rheology provides insights into the oral phase of eating.

For gels rheological behaviour is closely connected to gel microstructure and a combination of rheology and microscopy reveals the relationships in real time.

In the area of biopolymer melts, rheology elucidates the behaviour of protein melts in intricate processes such as when fibres spontaneously for on cooling of a protein melt. The resulting fibrous structure resembles that of meat and is utilise in producing plant-based meat analogues.

In the same spirit, plant-based polymers can mimic properties of plastics yet retaining their food status. This is utilised in edible barriers as well as in constructs for tissue engineering of cultured meat. Ultimately, rheology may not be the answer to every question, but is a powerful tool that can unlock the secrets to healthy aging as well as contributing to mitigate global warming.

INTRODUCTION

The area ranging from fluid to solid is huge and this contribution will be limited to biological system, and further mainly to edible biopolymer systems. You will find a short introduction to the respective materials addressed.

FLUIDS

Healthy individuals apply highly unconscious, but very well coordinated strategies for oral processing and swallowing. The digestive tract shares the throat with the airways which means that we unconsciously close the entrance to the airways and hold our breath while fluid, or a food bolus passes over it. However, for an increasing proportion of the population swallowing causes problems. Swallowing disorders, or dysphagia, affects almost half of the population

older than 70 who will require an intake of thickened beverages to slow down the flow and give time for the body to perform the necessary actions. The general conclusion is that higher viscosity is better as long as the fluid does not become sticky[1].

The rheological properties of both beverages and food boluses are important for safe swallowing. We have previously demonstrated that fluid elasticity is important[2] and contributes to fluid cohesion. This is in itself a "fluid" term that expresses the resistance of a bolus to break up into smaller drops. The term is more often used than it is well defined. The action is nevertheless important as smaller droplets have a higher risk of entering the airways. Management of dysphagia requires texture-modification of solid food and the properties of the bolus reflects the degree of modification[3,4]. In order to study the flow during swallowing the velocity can either be measured non-invasively in-vivo using an ultrasonic transducer[5], or be studied in laboratory models of the human throat[6,7], see **Fig. 1.**

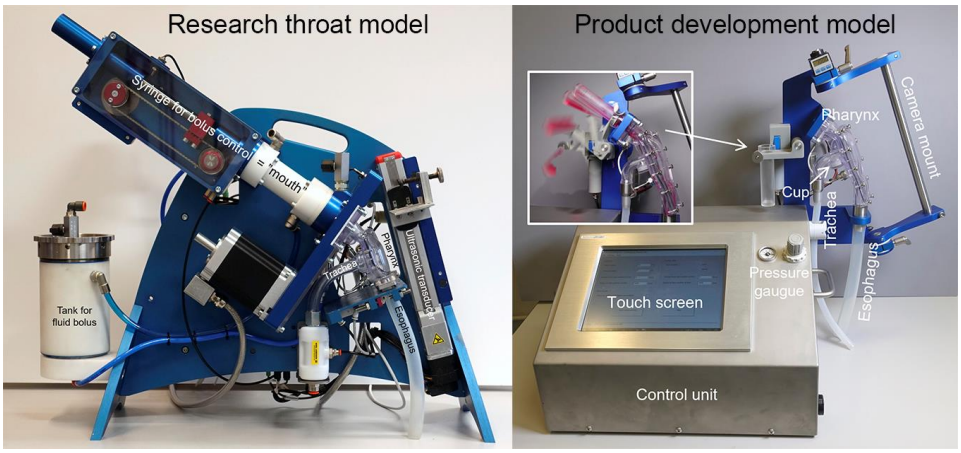

FIGURE 1: Two models of the human throat, "The Gothenburg Throat". a) research model[6], and b) product development model[7].

GELS

Gels are fascinating materials that exhibit both solid and liquid properties. It has been said "the colloidal condition, the gel, is one which is easier to recognize than to define" [8], but there are rheology-based definitions showing that it is indeed possible to define[9]. Understanding the gel-structure relationship is crucial for applications in food, pharmaceuticals as well as tissue engineering. Rheology helps us explore how the structure of gels affects their mechanical properties and functionality.

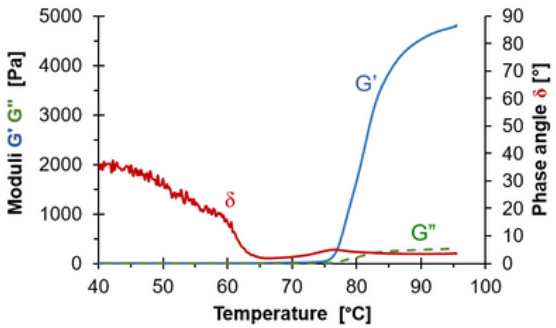

FIGURE 2: Storage modulus G′, loss modulus G″ and phase angle δ for egg white as a function of increasing temperature.

As an example, **Fig. 2** shows how egg white forms a gel with increasing temperatures, which is what we observe when we boil an egg. At room temperature, the egg white appears to be a liquid even if the phase angle δ is low and therefore may already appear to be a gel. As the temperature increases, the storage modulus G′ increases faster than the loss modulus G″ and when the albumin in the egg white coagulates and forms a three-dimensional network, G′ becomes much larger than G″. This can be followed thanks to the instrument being able to keep the deformation sufficiently small not to break any structure. **Fig. 2** shows that the egg white solidifies just above 75°C when the storage modulus G′ rises sharply. However, the phase angle shows that the egg white already at a low temperature has a structure (δ<40°) and that gel formation is underway already below 75°C.

MELTS

In the rheology area, melt rheology has been mainly studied for petroleum-based polymers. These have a substantial use in e.g. plastics and consumer products, and also possible to produce well-defined polymer fractions e.g. for testing constitutive models. Biopolymers are rarely well-defined and depend on botanical or zoological source, preparation, growing conditions etc. There is, however, a trend towards replacing petroleum-based polymer with biopolymers in materials, and another trend in replacing animal biopolymers such as protein with plant-based ones.

The food industry is undergoing a significant shift towards plant-based meat alternatives, driven by consumer concerns about sustainability, health, and animal welfare [5, 6]. Among these alternatives, plant-based meat analogues are particularly popular due to their reasonable price, availability, and cultural acceptance [7]. To enhance consumer appeal, it is important for these analogues to replicate the texture, taste, sensory and nutritional profiles of animal meats. The high-moisture extrusion (HME) process is the most common method used to create a fibrous, meat-like structure. Currently, fibrous analogues are commercially produced proteins form soy, pea and wheat using HME. This process involves forming a protein melt at high moisture content, temperature, and pressure, followed by active cooling upon exit[10-12], see **Fig. 3**. Factors such as extrusion temperature, die geometry, flow rate and the rheological properties of the protein melt influence the flow behaviour. The formation of fibrous structures with varying degrees of anisotropy is affected by the flow behaviour in the extruder, particularly in the cooling die [13-16]. It is known how to produce the fibres but still not exactly why they are formed.

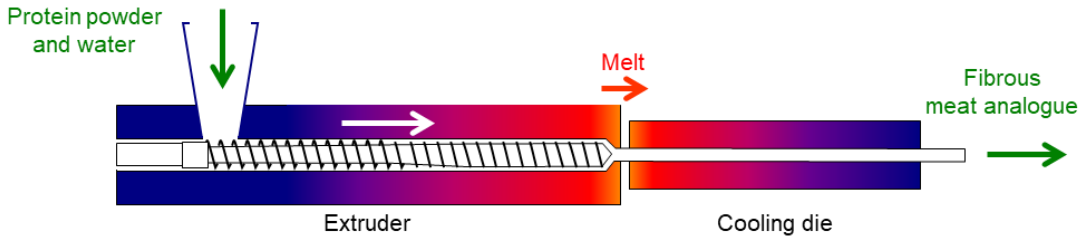

FIGURE 3: Principle of the high-moisture extrusion process for making plant-based meat analogues.

In order to develop meat analogues with predictable and desirable properties, optimising the process and tuning the rheological properties will be necessary. However, measuring the rheological properties of meat analogues at conditions relevant for extrusion is a challenge due

to the inabilities of conventional rheometers to measure at high temperature and pressure, typically up to 150°C and 5-10 bar, and to avoid moisture loss at elevated temperature[17]. Recent findings show that a closed cavity rheometer can determine rheological properties of plant-based proteins, at least in small-amplitude oscillatory shear (SAOS), [18-20] and it may potentially be capable of performing steady shear measurements in the future [21]. There are also recent publications where ultrasonic flow profiling [13] and high-pressure cells [22] have been utilised.

CONCLUSIONS

This is quite a general contribution and gives a helicopter perspective of the area of rheology of biopolymer systems, and as such does not provide specific conclusions. However, one general conclusion is that rheology often plays a crucial role in processing as well as in food and medical applications. Rheology has a direct implication even on global challenges such as the ageing population and global heating. It is also safe to conclude that there is still much to do in modelling of rheological mechanisms as well as in experimental techniques.

REFERENCES

1. Newman R, Vilardell N, Clavé P, Speyer R. Effect of Bolus Viscosity on the Safety and Efficacy of Swallowing and the Kinematics of the Swallow Response in Patients with Oropharyngeal Dysphagia: White Paper by the European Society for Swallowing Disorders (ESSD). journal article. *Dysphagia*. 2016;31(2):232-249. doi:10.1007/s00455-016-9696-8
2. Nystrom M, Waqas Muhammad, Margareta Bulow, Olle Ekberg, Stading M. Effects of rheological factors on perceived ease of swallowing. *Appl Rheol*. 2015;25(6)
3. Stading M, Miljkovic A, Andersson J, Matsuo K. Bolus rheology of texture adjusted food—Effect of age. *Journal of Texture Studies*. 2023;54(6):824-834. doi:https://doi.org/10.1111/jtxs.12789
4. Stading M. Bolus rheology of texture-modified food – effect of degree of modification. *J Text Stud*. 2021;52:540-551. doi:10.1111/JTXS.12598
5. Qazi WM, Ekberg O, Wiklund J, Mansoor R, Stading M. Simultaneous X-ray Video-Fluoroscopy and Pulsed Ultrasound Velocimetry Analyses of the Pharyngeal Phase of Swallowing of Boluses with Different Rheological Properties. *Dysphagia*. 2020/02/11 2020;doi:10.1007/s00455-020-10092-4
6. Stading M, Waqas MQ, Holmberg F, Wiklund J, Kotze R, Ekberg O. A Device that Models Human Swallowing. *Dysphagia*. 2019/10/01 2019;34(5):615-626. doi:10.1007/s00455-018-09969-2
7. Stading M, Andersson A, Holmberg F. A mechanical model of the human throat for swallowing rheology. *Annual Transactions of the Nordic Rheology Society*. 2021;29
8. Lloyd DJ, In D. Colloid chemistry. *red Alexander J), The Chemical Catalog Co, New York*. 1926;1
9. Almdal K, Dyre J, Hvidt S, Kramer O. Towards a phenomenological definition of the term 'gel'. *Polymer Gels and Networks [0966-7822]*. 1993;1(1):5-17.
10. Cheftel JC, Kitagawa M, Quéguiner C. New protein texturization processes by extrusion cooking at high moisture levels. *Food Rev Int*. 1992/01/01 1992;8(2):235-275. doi:10.1080/87559129209540940
11. Jones OG. Recent advances in the functionality of non-animal-sourced proteins contributing to their use in meat analogs. *Curr Opin Food Sci*. 2016/02/01/ 2016;7:7-13. doi:https://doi.org/10.1016/j.cofs.2015.08.002
12. Wittek P, Zeiler N, Karbstein HP, Emin MA. High Moisture Extrusion of Soy Protein: Investigations on the Formation of Anisotropic Product Structure. *Foods*. 2021/01/06/ 2021;10(1):102. doi:10.3390/foods10010102
13. Kaunisto E, Tsegaye B, Kotzé R, Wiklund J, Kádár R, Stading M. Towards in-line rheology measurement of protein melts during high moisture extrusion by pulsed ultrasound velocimetry. *J Food Eng*. 2025:in press.
14. Kaunisto E, Wassén S, Stading M. A thermodynamical finite element model of the fibre formation process during extrusion of high-moisture meat analogues. *J Food Eng*. 2024/02// 2024;362:111760. doi:10.1016/j.jfoodeng.2023.111760

15. Van Der Sman RGM, Van Der Goot AJ. Hypotheses concerning structuring of extruded meat analogs. *Curr Res Food Sci*. 2023 2023;6:100510. doi:10.1016/j.crfs.2023.100510
16. Sandoval Murillo JL, Osen R, Hiermaier S, Ganzenmüller G. Towards understanding the mechanism of fibrous texture formation during high-moisture extrusion of meat substitutes. *J Food Eng*. 2019/02// 2019;242:8-20. doi:10.1016/j.jfoodeng.2018.08.009
17. Tsegaye B, Barman S, Bovagne L, et al. Rheological properties of pea protein melts used for producing meat analogues. *Appl Rheol*. 2025:in press.
18. Schreuders FKG, Sagis LMC, Bodnár I, Erni P, Boom RM, Van Der Goot AJ. Small and large oscillatory shear properties of concentrated proteins. *Food Hydrocoll*. 2021/01// 2021;110:106172. doi:10.1016/j.foodhyd.2020.106172
19. Wittek P, Zeiler N, Karbstein HP, Emin MA. Analysis of the complex rheological properties of highly concentrated proteins with a closed cavity rheometer. *Appl Rheol*. 2020/01/01/ 2020;30(1):64-76. doi:10.1515/arh-2020-0107
20. Emin MA, Quevedo M, Wilhelm M, Karbstein HP. Analysis of the reaction behavior of highly concentrated plant proteins in extrusion-like conditions. *Innov Food Sci Emer Technol*. 2017/12// 2017;44:15-20. doi:10.1016/j.ifset.2017.09.013
21. Ellwanger F, Georgantopoulos CK, Karbstein HP, Wilhelm M, Azad Emin M. Application of the ramp test from a closed cavity rheometer to obtain the steady-state shear viscosity. *Appl Rheol*. 2023/05/05/ 2023;33(1):20220149. doi:10.1515/arh-2022-0149
22. Sägesser C, Mair T, Braun A, Dumpler J, Fischer P, Mathys A. Application of a shear cell for the simulation of extrusion to test the structurability of raw materials. *Food Hydrocolloids*. 2025/03// 2025;160:110736. doi:10.1016/j.foodhyd.2024.110736

This award is given to a person who has made outstanding contributions to the basic understanding of rheological phenomena and/or the application of rheology.

Professor **Mats Stading** has his main research activities at RISE Research Institutes of Sweden and is also Adjunct Professor at Industrial and Materials Science at Chalmers University of Technology, both located in Gothenburg, Sweden. He has an MSc degree in Engineering Physics and has then widened his scope with a PhD in biophysics and a post-doc in tissue engineering at MIT. Since then, he is back in Gothenburg for positions at Chalmers and RISE.

Professor Stading is internationally active leading research projects in Europe, Africa and Asia. Within rheology, he has been active in the Nordic Rheology Society board since the start of the Society and was also President and board member of the European Society of Rheology.

His research involves rheology applied to biopolymer fluids, gels and melts. Current hot topics include plant protein melts for meat replacement and foods with safe swallowing for seniors.

Congratulations to Prof. Mats Stading on this fantastic achievement!

NRS Young Rheologist Award Lecture

Measure, Understand and Predict Structure Formation in Anisotropic Plant-Based Foods – using Rheology

Julie Frost Dahl, Milena Corredig

Department of Food Science, Aarhus University, Denmark

Julie.Dahl@IFF.com

Imagine you're developing a new plant-based food product. Which ingredients should you use? What process parameters should you select? You plan a set of experiments: adjust one ingredient, run the process; tweak a parameter, run the process again. Sounds time-consuming and resource-intensive, doesn't it? This is, however, how many plant-based meat analogues, produced by high-moisture extrusion (HME), reach the shelves.

As HME is a closed system, we cannot open it up and see what happens inside during processing. Instead, we often rely on evaluating what comes out. But what marks a good final product? HME produces anisotropic products, meaning they have directionally dependent structural properties. But how can we capture this anisotropy? At which length scale is it important? To answer these questions, the first part of the work focuses on how to properly **measure** important quality attributes using rheology and complementary techniques.

So, what if we don't limit ourselves to characterizing structures post-extrusion? How can we evaluate the material properties during processing? This can be done by employing a closed cavity rheometer (CCR) to simulate HME conditions using Large Amplitude Oscillatory Shear (LAOS) rheology. The second part of the work focuses on linking CCR rheological data to post-extrusion structural quality, to establish correlations that deepen our understanding of structure formation during HME.

Additionally, a high-throughput capability of the CCR enables data-driven research approaches. The last part of the work uses compositional data to **predict** the rheological properties of plant-based biopolymer mixes. It demonstrates machine learning as a solution to reduce the trial-and-error approach in product development, enhancing our **understanding** of system dynamics and accelerating the improvement of future plant-based food products.

The year's winner of the NRS Young Rheologist Award is **Julie Frost Dahl**.

The Young Rheologist Award is given to a young person, who has made outstanding work in basic or applied rheology at the graduate or postgraduate level.

Julie has recently completed her PhD at Aarhus University, Denmark under the supervision of Milena Corredig. In her research, she developed strategies for characterising and predicting anisotropic food structures, which are of great relevance for novel foods such as meat analogues. She now works as a scientist at IFF in Brabrand, Denmark.

Congratulations on this great and well-deserved achievement, Julie!

Advances in Rheological Methods

MEASURING FIRST NORMAL STRESS DIFFERENCE AT HIGH SHEAR RATES VIA CAPILLARY RHEOMETER

Dr.-Ing. Joachim Sunder

GOETTFERT GmbH, D-74722 Buchen, Germany

ABSTRACT

First normal stress difference is commonly measured in cone-plate geometries up to the shear rates of around 10 s^{-1} with rotational rheometers. At higher shear rates the measurement is limited either by the torque or normal force threshold of the instrument or by some material related limitations e. g. edge fracture. A new Normal Stress die designed to simultaneously measure steady-state shear viscosity and first normal stress difference at higher shear rates (>>10 s^{-1}) via capillary rheometer is first introduced.

Measured data of first normal stress difference are then correlated to the onset of flow instabilities like shark skin of plastics and poor extrusion of rubber compounds detected by Garvey die. Here dimensionless numbers introduced to increase selectivity. First normal stress difference measurement also opens an easy and effective way to analyse the die drool effect.

NORMAL STRESS DIE DESCRIPTION AND VALIDATION

The normal stress die was developed in collaboration with Karlsruhe Institute of Technology (KIT), institute for Chemical Technology and Polymer Chemistry (ITCP)[1].

Normal Stress die is composed of two parts, slit part and radial part: See **Fig 1**. Steady-state shear viscosity is measured in the slit part and first normal stress difference is measured in the radial part.

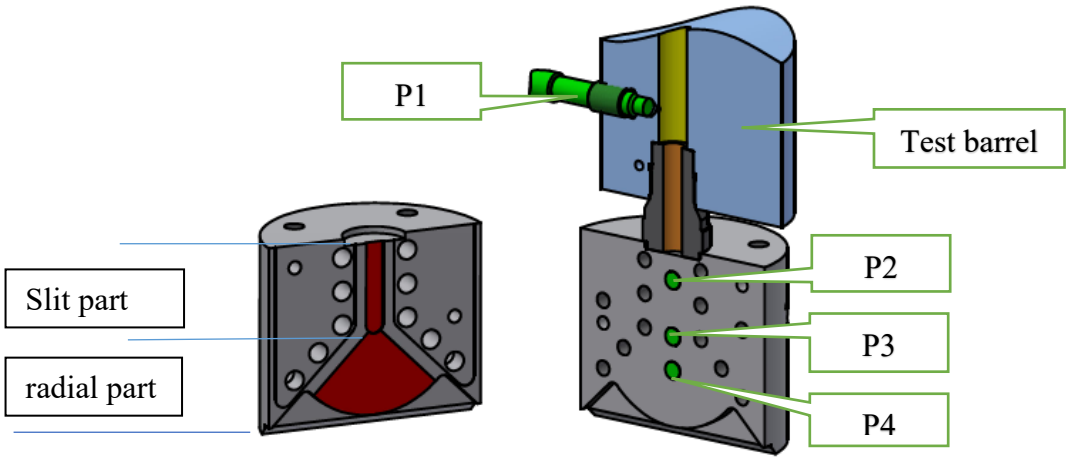

FIGURE 1: Open parts of the slit-radial die. (a) Channel half and (b) Sensor half.

Steady-state viscosity is calculated slit part: See Eq (**1**). The Bagley correction is not necessary since the pressure is measured with the pressure difference of the pressure transducers inside

the die (P_3-P_2). The steady-state viscosity is obtained after Weissenberg-Rabinowitsch correction.

$$\eta_a = \frac{\sigma_a}{\dot{\gamma}_a} = \frac{\Delta P_{slit}}{L}\frac{H^3\,W}{12Q} \tag{1}$$

Elongation viscosity is calculated using the Cogswell model from the entrance pressure loss measured between P1 in the barrel and the extrapolated pressure at the entry of the capillary extrapolated from pressure P2 and P3.
First normal stress difference is calculated in the radial part of the Normal Stress die by Eq (2).

$$\langle N\rangle = 0.1\left[-r_2\frac{P4-P3}{r_3-r_2}+\frac{(2n+1)}{n}\left[\frac{Q}{\pi h^2 r_2}\frac{2n+1}{n}\right]^{n-1}\right] \tag{2}$$

Where $\langle N\rangle$ is the average first normal stress, r_2 and r_3 are the radii in which the second and third pressure sensors are located, Q is the volumetric flux, P3 and P4 are the pressure values of third and fourth pressure sensors, h is the height of radial part and n is the power law index.

Steady-state first normal stress difference as a function of shear rate is obtained from transient shear experiment with 13 mm cone-plate geometry and Normal Stress die at 230 °C for polypropylene: see **Fig. 2**.

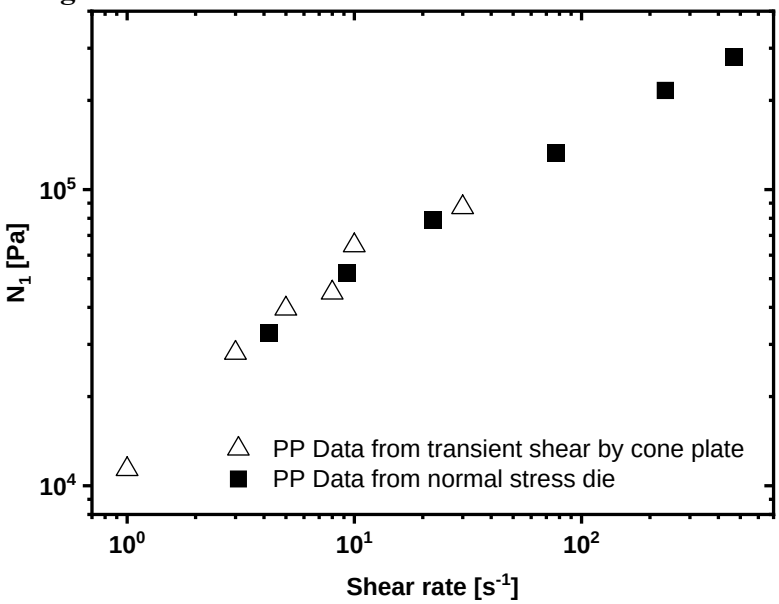

FIGURE 2: First normal stress difference from different methods vs shear rate for LDPEs at 230 °C.

FLOW INSTABILITIES AND FIRST NORMAL STRESS DIFFERENCE

The prediction of flow instabilities is one of the target tasks in extrusion quality. The effect of rheological properties like viscosity, entrance pressure loss/elongation viscosity and 1st normal stress difference is first illustrated using the measurement with normal stress die at 6 LDPE and detected flow instabilities. Flow instabilities are detected with the shark skin die developed in collaboration with KIT[2] mounted on a capillary rheometer with the geometry of 3/0.3/30 mm/mm/mm W/T/L slit die. Bagley and Weissenberg-Rabinowitsch corrected steady-state shear viscosity of the samples at 180 °C. is plotted versus shear rate: See **Fig 3**. Data of sample

3-4 and sample 5-6 show about the same behaviour. The onset of instabilities in a 3/0.3/30 mm/mm/mm W/T/L slit die at 180 °C is reported in **TABLE 1.**

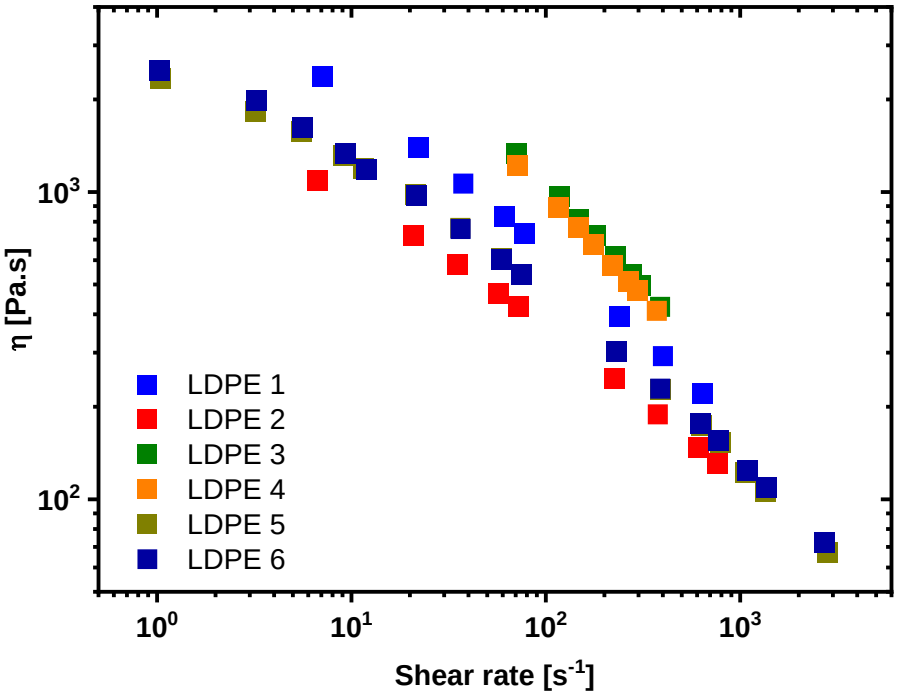

FIGURE 3: Steady-state shear viscosity vs shear rate of LDPEs obtained from slit part of the normal stress die at 180 °C.

TABLE 1: The onset of instabilities for different LDPEs at 180 °C.

Material	Onset of instabilities (Shear rate) at 180 °C with slit die [s^{-1}]	
LDPE 1	250	
LDPE 2	Not seen	
LDPE 3	20	
LDPE 4	80	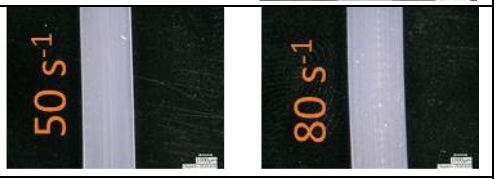
LDPE 5	Not seen	
LDPE 6	500	

Viscosity data cannot differentiate between samples in the same order as detected by shark skin analysis. Entrance pressure loss shows a better differentiation of the samples in regard of flow instabilities but cannot fully differentiate between the samples.

The measurement of 1st normal stress difference can differentiate between the samples. To enlarge the differences the data are divided by entrance pressure loss, which also influences instabilities. The number N_1/dP_e is dimensionless and plotted vs shear rate for the 6 LDPEs; See **Fig. 4**. The data show the same ranking as the data in table 1. The ratio of N_1/dP_e gets higher when the onset of instabilities happens at higher shear rates.

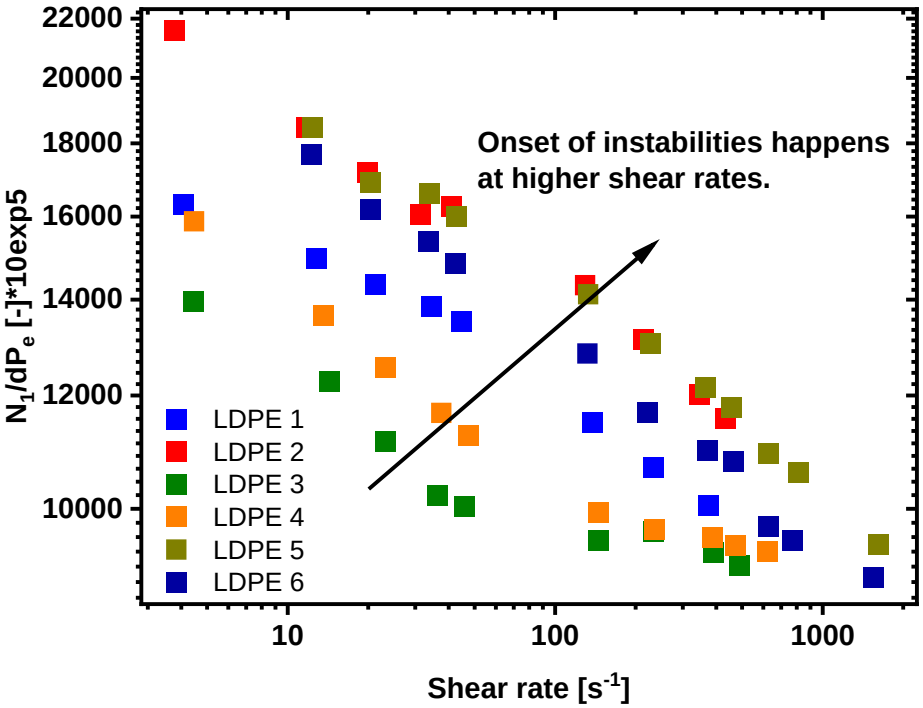

FIGURE 4 First normal stress difference divided by entrance pressure loss (dP_e) as a function of shear rare at 180 °C for different LDPEs.

NORMAL STRESS DATA COMPARED WITH GARVEY DIE EVALUATIONS

The quality of rubber extrusion compounds can be analyses by Garvey die measurement. The method is done in a manual operated time-consuming procedure with often even manual evaluation. This time-consuming evaluation of extrudate quality by Garvey die is performed on four different rubber compounds[3]: See **Fig.5**. Two pairs of material one with good and one with bad extrusion quality can be seen. The materials are then also measured by normal stress die in a much shorter time and evaluation just takes a mouse klick. The data of 1st normal stress difference divided by entrance pressure loss plotted versus shear rate and shows a similar tendency as the previous example, extrusion quality gets better with increasing ratio of N_1/dP_e: See **Fig6**. Garvey die measurement**: See Fig 5,** is made at one just one throughput and has to be repeated several times to evaluate different throughputs while the measurement performed by normal stress die: See Fig.6, is made at different shear rates within one filling of the test barrel.

Ratings:			45				
bad	1	Compound number	swell	edge	surf.	corn.	Sum
acceptable	2	4	1	1	1	1	4
good	3	7	3	3	4	4	14
excellent	4	11	1	2	1	3	7
		14	4	4	4	4	16

FIGURE 5: Gavey die evaluation from 4 rubber compounds at one throughput – shear rate

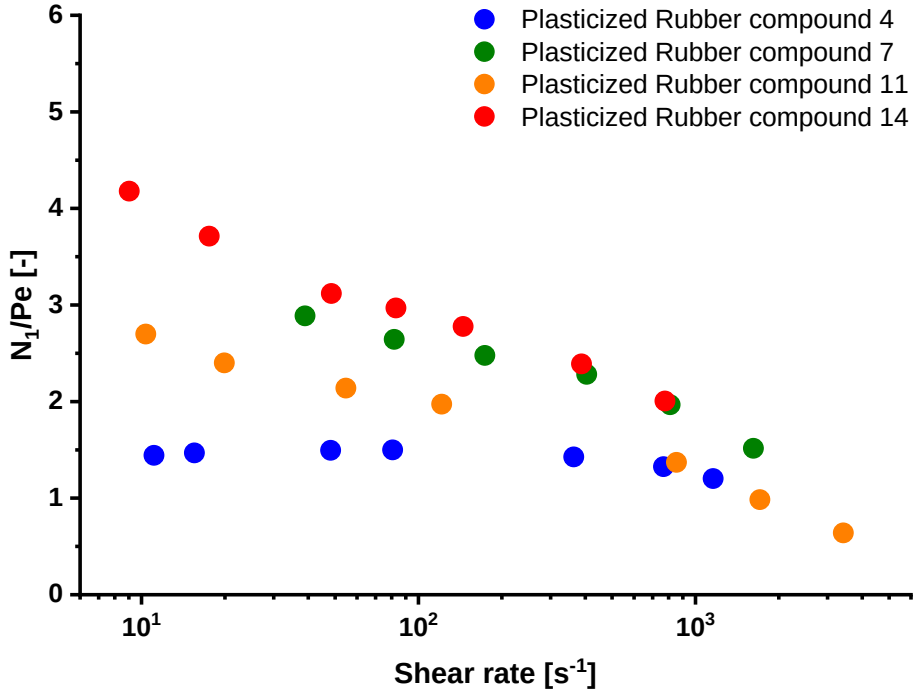

FIGURE 6: First normal stress difference divided by entrance pressure loss (dP_e) as a function of shear rare for four different rubber compounds

NORMAL STRESS DIFFERENCE AND DIE DROOL EVALUATIONS

Some polymers depose a part of the mass flow to the die lip. By a longer extrusion period the deposits grow and frequently some parts break and cause defects at the extrudate. This phenomenon is also called "die drool" or "die bleed". The effect is also analyzed on some HDPE relating to their and molecular structure[4]. Differences in molecular structure also lead to differences in 1st normal stress difference.

Die drool is analyzed on 4 different HDPE and measured with Normal stress die: See **Fig. 7**. Die Drool was analyzed at Shear rate 500 1/s at 170°C for 2h extrusion. Sample 1 and 2 show nearly no die drool, while sample 3 shows slightly more. Only sample 4 clearly shows die drool under these conditions. 1st normal stress difference itself shows increasing values for increasing

tendency of die drool build up, but sample 4 is no so much differentiated. There the data of 1st normal stress difference are also divided by entrance pressure loss. Now sample 4 clearly differs from the other sample: See **Fig.7**.

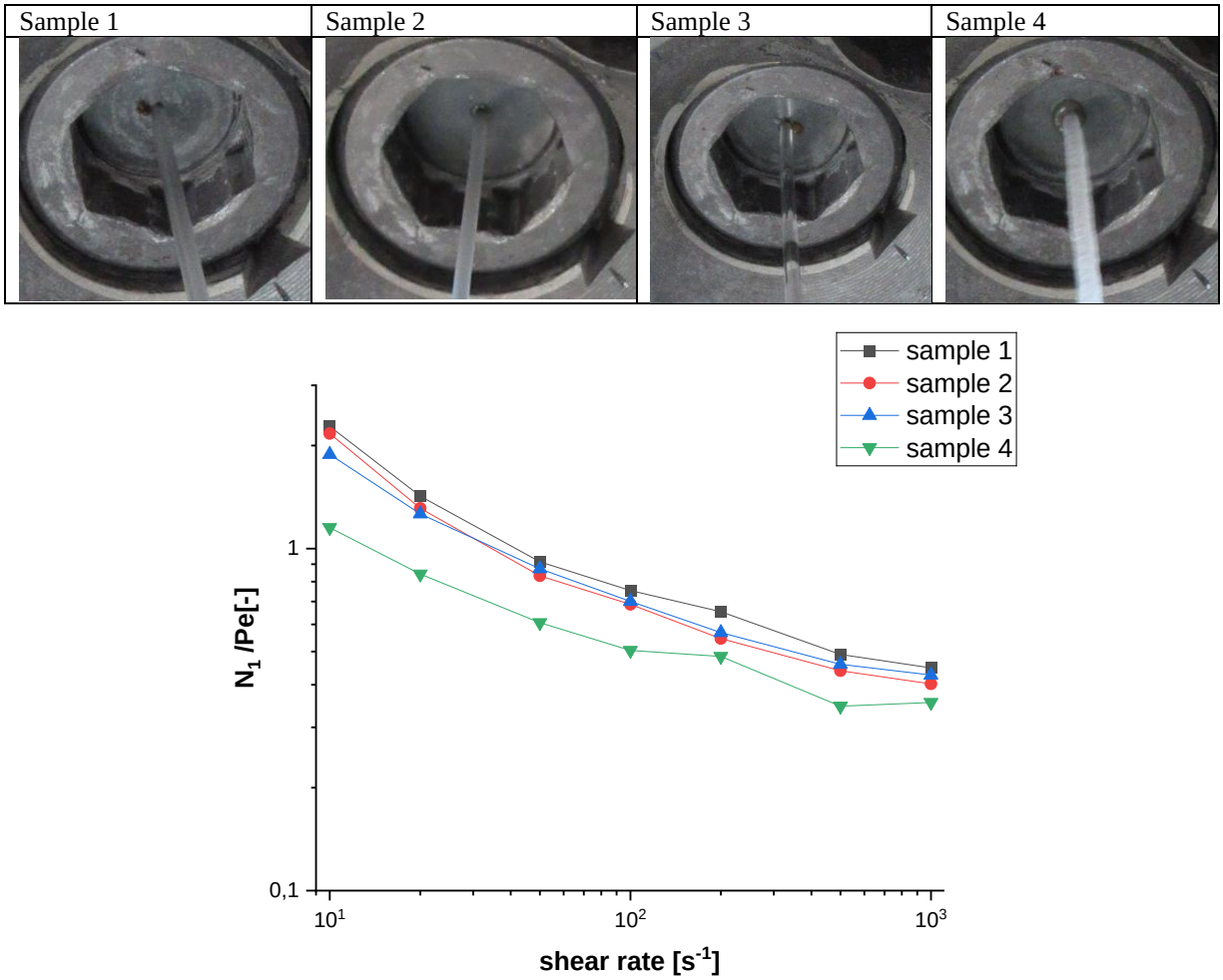

FIGURE 7: Die drool measurement at shear rate 500 1/s and first normal stress difference divided by entrance pressure loss (dP_e) as a function of shear rare for four HDPE samples

CONCLUSIONS

Normal Stress die can simultaneously measure steady-state shear viscosity, elongation viscosity and first normal stress difference. The viscosity obtained from the slit part of Normal Stress die after Weissenberg-Rabinowitsch correction matches the viscosity measured with capillary dies after Bagley and Weissenberg-Rabinowitsch corrections. Elongation viscosity is derived from the entrance pressure into the die. First normal stress difference obtained from Normal Stress die at high shear rates follows the same trend as transient shear data at low shear rates. Thus, a good accordance between the data of normal stress die and transient shear data is visible. Normal stress die allows an effective determination of normal stress at high shear rates and closer to the processing shear rates which was not possible with conventional technique.

Further the onset of instabilities is correlated to first normal stress difference and entrance pressure drop (graph of N_1/dP_e vs shear rate). The materials with lower N_1/dP_e for the same shear rate, show onset of instabilities at lower shear rates.
For rubber compounds extrudate defect measured by Garvey die are also first normal stress difference and entrance pressure drop (graph of N_1/dP_e vs shear rate). Materials with lower N_1/dP_e for the same shear rate, show an extrudate with more defects.
Finally, N_1/dP_e is correlated to die drool phenomenon. Materials with lower N_1/dP_e data show a higher tendency to die drool build up.

BIBLIOGRAPHY

1. Masood Khabazian Esfahani, Christos K. Georgantopoulos, Ingo F.C. Naue, Joachim Sunder, Manfred Wilhelm, A new slit-radial die for simultaneaously measuring steady stae visvosity and first normal stress difference of viscoelastic liquids via capillary rheometry. J. *Appl. Polym. SCi 2022;e52094.* https://doi.org/10.1002/app.52094.
2. Susanna Filipe, Iakovos Vittorias, Manfred Wilhelm. Experimental Correlation between Mechanical Non-linearity in LAOS Flow and Capillary Flow Instabilities for Linear and Branched Commercial Polyethylenes. Macromol.Mater. Eng. 2008, 293, 57-65. https://doi.org/10.1002/mame.200700194.
3. E. Borchardt, T. Ruckert, H. Schönfeld, Tests performed at Continental 2017
4. Martin Zatloukal, Jan Musil, Investigation of Die Drool Phenomenon for Linear HDPE Melts Havin Identical Polydispersity Index but Different MZ and MZ+1 Avarage Molecular Weight, SPE Extrusion Division, Paper of the Month 05/2012

.

Suspensions, Composites, and Multiphase Materials

RHEOLOGICAL AND TECHNOLOGICAL ASPECTS OF UV CURING THICK POLYMER LAYERS WITH FIBER REINFORCEMENT

Michael Müller-Pabel[1], Johann Faust[1], Florian Schmidt[1], Eckart Kunze[1], Maik Gude[1]

[1]Dresden University of Technology, Institute of Lightweight Engineering and Polymer Technology, Holbeinstr. 3, 01307 Dresden, Germany

ABSTRACT

UV curing allows energy-efficient and fast resin solidification for many different applications. By combining suitable photoinitiators and light-emitting diode (LED) light sources, cure depths of more than 1 mm have become available, which makes UV curing also a promising candidate for the development of innovative manufacturing technologies including fiber-reinforced polymers (FRP). This contribution suggests experimental methods that help to understand the interaction between process parameters, curing behavior and resulting material properties of a novel UV resin. UV-rheology is used to replicate close to reality process conditions during curing as well as to analyze the underlying phenomena including the mechanical and the volumetric material behavior. When investigating thick polymer layers, opposing effects such as heat accumulation within the resin volume and limited penetration depth of the UV light need to be taken into account. Both effects will have influence on the reaction rate and at the same time affect the optical properties of the resin. By evaluating UV-rheological experiments in conjunction with additional experimental data obtained in UV-DSC, a holistic understanding of the governing phenomena during UV curing of thick reinforced and unreinforced polymers becomes possible.

INTRODUCTION

Industrial applications of photopolymerization reactions can be found in versatile fields like additive manufacturing[1], dental medicine and coating[2]. All these have in common that they require curing of layers with a thickness of less than 200 µm. In the course of efficiency increases in light-emitting diode (LED) technology[3] and the development of new photoinitiators[4], the use of ultraviolet (UV) light has proven to be a promising mechanism that enables extremely short reaction times (< 1 s) as well as use of cheap and unheated tools which allows significantly improved energy efficiency[5]. The usability of UV-resins in processing of fiber-reinforced polymers (FRP) was demonstrated for pultrusion[6], resin injection[7], additive manufacturing[8] and prepreg processing[9]. It was shown that energy-efficient curing of layers of more than 10 mm is possible[10]. However, the basic process-property-relationships governing those technologies is still missing, which is why no guidelines for definition of process windows are available. To fully exploit the potential of UV curing in FRP processing, the interaction mechanisms between radiation transport, curing reaction and temperature development need to be understood. UV-rheology can help to answer these questions. In previous studies UV-rheology was used to analyze the cure behavior of UV-resins destined for stereolithography (SLA)[1,11] and Digital Light Processing (DLP)[12]. Due to the focus on thin layers of less than 200 µm, some aspects were neglected that are of crucial importance for curing thick layers (> 1 mm) and FRPs. This includes exothermal heat and the spatial distribution of optical properties. In order to adapt established rheological methods to the analysis of UV-resins,

additional information about the thickness-dependent reaction kinetics and curing speed is required. To meet these requirements, within this contribution rheological and calorimetric measurements are combined to characterize the UV curing properties of a vinyl ester resin. To demonstrate feasibility of UV curing FRP, a winding process was set up and used for manufacturing of composite sleeves. During these trials different process parameters including winding speed and light intensity were varied in order to validate the previously derived process window.

MATERIALS AND METHODS

The resin system analysed in this study is the vinyl ester resin Raylok C1101 (supplied by Allnex GmbH). The recommended wavelength for UV-light curing is 365 nm. A DELOLOX 80 in combination with a DELO-UNIPRO Light control unit is used for this purpose.

UV-DSC measurements were conducted with a Mettler Toledo DSC 3+ and the corresponding UV-equipment. Open Aluminium crucibles with a volume of 40 µl, an isothermal temperature of 25 °C and a nitrogen purge gas rate of 20 ml/min were selected. UV-rheology tests were performed with an Anton Paar MCR 502 being equipped with a bottom glass plate (P-ETD 300) as well as a hub (H-ETD 300), both of them heated electrically. Disposable plates with a diameter of 25 mm were used. The measurements were performed in oscillation mode with a frequency of 10 Hz and an amplitude of 0.05 %. Normal force control was activated in order to detect shrinkage induced volume change after gelation. Prior to all DSC and rheology measurements, the light intensity at the sample position was determined with a DELOLUXcontrol light intensity meter.

Winding experiments were performed with the winding machine (Bolenz & Schäfer) at the ILK and monitored by thermography using a VarioCAM HD (supplied InfraTec GmbH).

RESULTS

UV-DSC measurements

To gain insight into the radiation-dependent curing behaviour of the selected resin system, preliminary UV-DSC measurements with varying sample mass and irradiation parameters were conducted at room temperature ($T_R = 25.00$ °C). It was found that due to the high reactivity, it is necessary to prevent excessive heat release, as a temperature increase of more than 1 K contradicts basic principles of calorimetry, Table 1. It was concluded that the use of small a sample mass m (~2 mg), a low intensity I (20 mW/cm²) and a short irradiation time t_I (0.1 s), resulting in an energy dose E per pulse of 2 mJ/cm², is suited to control the curing reaction.

TABLE 1: sample peak temperatures T_{Smax} measured in UV-DSC at a ref. temperature $T_R = 25.00$ °C

Sample mass m /mg	Intensity I / mW/cm²	Irradiation time t_I /s	Energy dose per pulse / mJ/cm²	Sample peak temperature T_{Smax} /°C
6.05	950	1.0	950	39.98
4.06	950	1.0	950	35.52
2.23	950	1.0	950	31.97
1.29	950	1.0	950	28.51
4.96	475	1.0	475	39.47
5.06	95	1.0	95	36.06
5.14	950	0.1	95	29.47
2.92	20	0.1	2	25.32

Subsequently, measurements with multiple consecutive pulses of 2 mJ/cm² were performed. The time span between the pulses was chosen according to the peak height and the time required for the heat flow to return to the baseline. As can be seen in Fig. 1, both the measured heat flow and the corresponding reaction rate depend on the pulse number. From pulse 1 to pulse 5 the reactivity increases and subsequently declines indicating that almost no further crosslinking takes place after 10 pulses. Summing up the measured enthalpy values results in a total heat release of 173 J/g, which corresponds to a degree of cure of 35 %. This low value can be explained by the vitrification effect as the measurements took place at 25 °C, which is far below the ultimate glass transition temperature of 152 °C indicated in the datasheet.

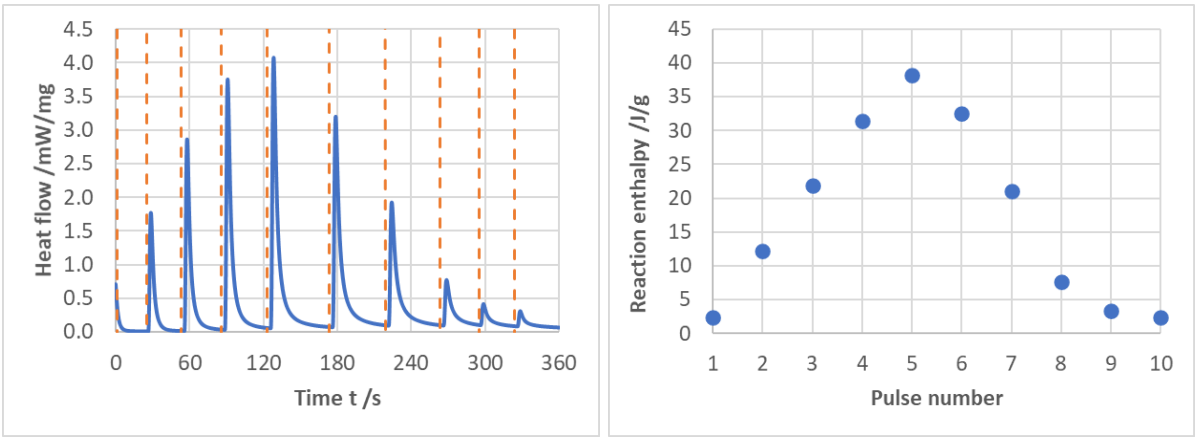

FIGURE 1: Results of UV-DSC measurements with light pulses of $I = 20$ mW/cm² and $t_I = 0.1$ s

UV-rheology measurements

Given the good controllability of the UV curing reaction by pulsating irradiation demonstrated with the UV-DSC measurements, this method is also favoured for the UV-rheology tests. In this case, a uniform dwell time of 10 s was inserted between the pulses of $t_I = 0.1$ s and $I = 20$ mW/cm². In order to investigate the influence of different sample volumes, the initial gap d_0 was varied between 0.25 mm and 2.05 mm. The number of pulses applied was varied in dependence on the gap distance. The results of the shear storage modulus G' and the volumetric shrinkage β calculated based on the time-dependent gap $d(t)$:

$$\beta = \left[1 + \frac{1}{3}\left(\frac{d(t) - d_0}{d_0}\right)\right]^3 - 1 \quad (1)$$

are shown in Fig. 2. A clear dependence of the mechanical and the volumetric properties on layer thickness can be deduced from the diagrams. While at low d_0 values (between 0.25 mm and 0.40 mm) the increase of the storage modulus and the onset of shrinkage starts after 4 pulses (40 s), the required energy dose increases exponentially at higher d_0 values. At $d_0 = 2.05$ mm a total of 32 pulses (320 s) is required to reach gelation. This behaviour corresponds to the behaviour predicted by the Beer-Lambert law[1].

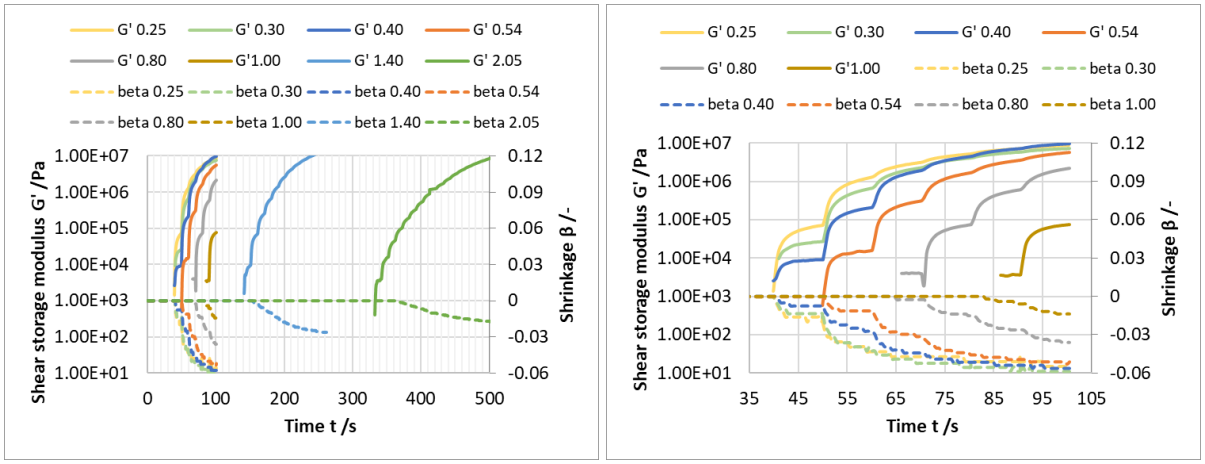

FIGURE 2: Left: thickness-dependent shear storage modulus and shrinkage measured during UV-rheological measurements with pulsing irradiation ($I = 20$ mW/cm² and $t_I = 0.1$ s) and intermediate dwell times of 10 s, right: zoom into the early test phase

The data from Fig. 2 can be further used to construct the working curves shown in Fig. 3, left, and mathematically described by[12]:

$$C = D_p \cdot ln\left(\frac{E}{E_c}\right), \tag{2}$$

where, C is the cure depth, D_p represents the penetration depth and E_c is the critical energy dose required to achieve gelation of a layer with infinitesimal thickness.

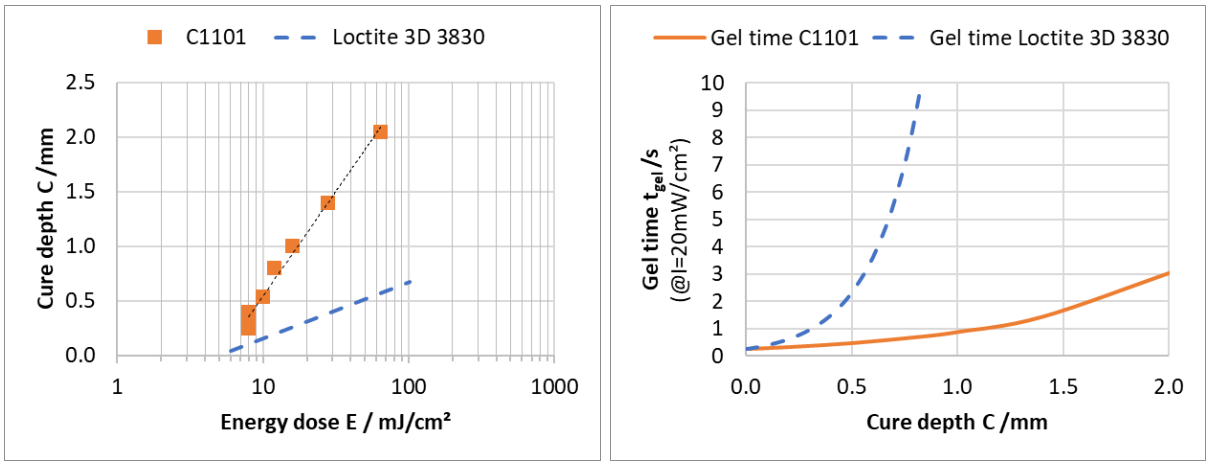

FIGURE 3: Left: working curve data and right: calculated thickness-dependent gel time at continuous irradiation with an intensity of 20 mW/cm² (values for Loctite resin are calculated based on data taken from literature[1])

Deriving D_p and E_c from the working curve (Fig. 3, left) gives $D_p = 0.82$ mm and $E_c = 5.21$ mJ/cm². To illustrate the deep cure ability of the investigated resin, the working curve of another commercial resin which is recommended for use in SLA (Loctite 3D 3830) is plotted in the same diagram. As can be seen, the Raylok C1101 allows largely improved deep cure when compared to the Loctite system. By rearranging Eq. 2 it is possible to calculate the thickness-dependent gel time for a given irradiation intensity:

$$t_{gel} = \frac{E_c}{I} \cdot exp\left(\frac{C}{D_p}\right) \quad (3)$$

Inserting the investigated gap values d_0 into the cure depth C and assuming a constant light intensity $I = 20$ mW/cm², yields the theoretical gel times shown in Fig. 3, right. As can be seen, both resins show comparable gel times at layer thicknesses below 0.1 mm. At higher thicknesses, however, C1101 clearly outperforms the Loctite system in terms of gel time. These results indicate that the mechanical properties shown (cf. Fig. 2) must be interpreted with regard to thickness gradients, especially if the measurements were performed at gaps above 1 mm. The temperature development of the resin due to the exothermal reaction is another source of error, which is not completely understood until now and needs further investigation (cf. Table 1).

Winding trials

In order to demonstrate the usability of the investigated resin system, a UV-light equipped winding process with glass fibre reinforcement was set up (Fig. 4, left) to manufacture FRP sleeves with an inner diameter of 100 mm and a thickness of 20 mm. To translate the high UV curing speed into high production speed, the use of a two-step process is necessary. During the first step, the glass fibre roving with a thickness of 0.2 mm is impregnated with the UV-resin and subsequently placed on the mandrel. The desired degree of cure after this step is close to gelation but still in a liquid state. During the second step, the succeeding layer will be placed partially on top of the preceding layer, which leads to gelation of the latter while ensuring sufficient tack between both layers. To ensure this stepwise curing, the required energy dose during one exposure to the UV light is set to a value slightly below 5 mJ/cm² (cf. Fig. 3, left). Winding speeds of 5 m/min, 10 m/min, 15 m/min, 30 m/min, 45 m/min and 60 m/min were employed. Given the diameter of the light cone of 20 mm these result in irradiation times of 0.24 s, 0.12 s, 0.08 s, 0.04 s, 0.027 s and 0.02 s. The light intensity was adjusted accordingly.

The winding process was monitored with the help of a thermographic camera in order to detect the heat release at the surface of the impregnated fibres (Fig. 4, right). After completion of the lay-up, the sleeves were post-cured by irradiation with higher intensity.

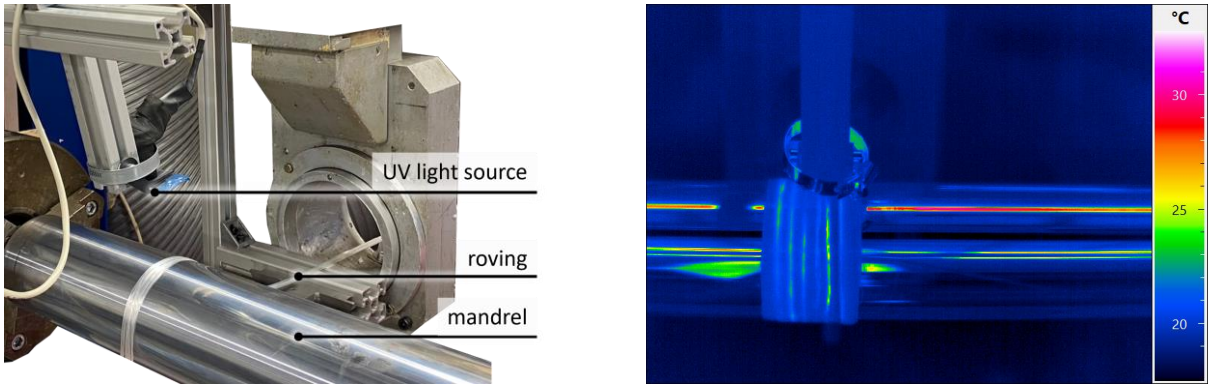

FIGURE 4: Left: main components of the UV-winding process, right: thermogram during lay-up

CONCLUSION

UV curing represents a promising and versatile option for energy-efficient and fast manufacturing of FRP with continuous fibres. While feasibility was shown for some processes, the underlying phenomena including heat transport and light penetration are only poorly

understood. This is mainly due to the fact that previous investigations are limited to thin layers. This contribution highlights some of the challenges associated with deep cure and suggests experimental approaches to give insight into the process-dependent material behaviour. Special attention was paid to the interpretation of UV-rheology measurements and the contribution of thickness effects. By applying the gathered knowledge to a UV-winding process, it was shown that the selected resin system can be employed for fast manufacturing of high-performance lightweight structures. Future work should focus on in-depth analysis of the reaction kinetics, which was shown to be temperature- and irradiation-dependent, as well as on determination of the temperature- and cure-dependent absorption coefficients of the constituents.

ACKNOWLEDGEMENTS

Funding was provided by the German Federal Ministry for Economics and Climate Action (BMWK) on the basis of decisions by the German Bundestag within the joint research projects “SWaT” (grant number 20M2112F)

REFERENCES

1. Rehbein, T. Experimental Characterization and Material Modeling of Photopolymers in Additive Manufacturing. Dissertation, Universität der Bundeswehr München, München, 2022. https://athene-forschung.rz.unibw-muenchen.de/doc/143903/143903.pdf (accessed 2024-07-16).
2. Lee, J. H.; Prud'homme, R. K.; Aksay, I. A. Cure depth in photopolymerization: Experiments and theory. *J. Mater. Res.* **2001**, *16* (12), 3536–3544. DOI: 10.1557/JMR.2001.0485.
3. Kneissl, M.; Seong, T.-Y.; Han, J.; Amano, H. The emergence and prospects of deep-ultraviolet light-emitting diode technologies. *Nat. Photonics* **2019**, *13* (4), 233–244. DOI: 10.1038/s41566-019-0359-9.
4. Zhou, J.; Allonas, X.; Ibrahim, A.; Liu, X. Progress in the development of polymeric and multifunctional photoinitiators. *Progress in Polymer Science* **2019**, *99*, 101165. DOI: 10.1016/j.progpolymsci.2019.101165.
5. Abliz, D.; Duan, Y.; Steuernagel, L.; Xie, L.; Li, D.; Ziegmann, G. Curing Methods for Advanced Polymer Composites - A Review. *Polymers and Polymer Composites* **2013**, *21* (6), 341–348. DOI: 10.1177/096739111302100602.
6. Saenz-Dominguez, I.; Tena, I.; Sarrionandia, M.; Torre, J.; Aurrekoetxea, J. Effect of ultraviolet curing kinetics on the mechanical properties of out of die pultruded vinyl ester composites. *Composites Part A: Applied Science and Manufacturing* **2018**, *109*, 280–289. DOI: 10.1016/j.compositesa.2018.03.015.
7. Çava, K.; İpek, H.; Uşun, A.; Aslan, M. Examine the mechanical properties of woven glass fiber fabric reinforced composite plate manufactured with vat-photopolymerization. *Polymer Composites* **2024.** DOI: 10.1002/pc.28955.
8. Kunze, E.; Müller-Pabel, M.; Weißenborn, O.; Luft, R.; Faust, J.; Geller, S.; Gude, M. Experimental studies for the additive manufacturing of continuous fiber reinforced composites using UV-curing thermosets. *ESAFORM 2021* **2021.** DOI: 10.25518/esaform21.3807.
9. G. Pérez-de-Eulate, N.; Iztueta, A. A.; Gondra, K.; Vallejo, F. J. Influence of the Fibre Content, Exposure Time, and Compaction Pressure on the Mechanical Properties of Ultraviolet-Cured Composites. *J. Compos. Sci.* **2020**, *4* (1), 30. DOI: 10.3390/jcs4010030.
10. Garra, P.; Dietlin, C.; Morlet-Savary, F.; Dumur, F.; Gigmes, D.; Fouassier, J.-P.; Lalevée, J. Photopolymerization processes of thick films and in shadow areas: a review for the access to composites. *Polym. Chem.* **2017**, *8* (46), 7088–7101. DOI: 10.1039/C7PY01778B.
11. Rau, D. A.; Reynolds, J. P.; Bryant, J. S.; Bortner, M. J.; Williams, C. B. A rheological approach for measuring cure depth of filled and unfilled photopolymers at additive manufacturing relevant length scales. *Additive Manufacturing* **2022**, *60*, 103207. DOI: 10.1016/j.addma.2022.103207.
12. Hofstetter, C.; Orman, S.; Baudis, S.; Stampfl, J. Combining cure depth and cure degree, a new way to fully characterize novel photopolymers. *Additive Manufacturing* **2018**, *24*, 166–172. DOI: 10.1016/j.addma.2018.09.025.

Rheological and Mechanical Properties of TPU Composites Reinforced with Silver-Coated Copper Flakes

Mohor Mihelčič[1], Alen Oseli[1], Lidija Slemenik Perše[1*]

[1]University of Ljubljana, Laboratory of Experimental Mechanics, Ljubljana, Aškerčeva ulica 6, 1000, Ljubljana, Slovenia

ABSTRACT

The study investigates the preparation of conductive thermoplastic polyurethane (TPU) composites using a twin-screw extrusion, focusing on the effects of silver-coated copper (Cu@Ag) particles as conductive fillers. The rheological, mechanical, and electrical properties of the composites were characterized as a function of filler volume concentration. The rheological analysis enabled the determination of a percolating network formation, which is important both for processing the composites and for mechanical reinforcement in the solid state. With increasing Cu@Ag loading, the composites exhibited pronounced changes in viscoelastic behaviour. The results of the mechanical tests show that increasing filler concentration of the Cu@Ag filler in the TPU polymer affects the mechanical properties, i.e., an increase in the storage moduli (E') and loss moduli (E'') was observed, resulting in a more brittle structure of the composite. Furthermore, the electrical conductivity increased sharply to 46.7 S/m at the highest filler concentration. The results showed that geometrical and electrical percolation thresholds were similar, occurring at ~15 vol.%. These results highlight the crucial role of filler loading in tailoring the conductive and viscoelastic properties of functional TPU composites.

INTRODUCTION

Composite materials have several advantages over metals, especially in applications where customized properties and shapes are of great importance. Therefore, much attention is given to the study of polymer-based composites where the effect of the pigment filler loadings has been varied[1,2]. This is particularly important in the production of electrically and thermally conductive polymer composites. Since polymer matrix is usually non-conductive, conductive filler particles or conductive polymers must be added to improve the conductivity. Such conductive filler particles can be metallic, carbon-based, ceramic or metal-coated. Copper (Cu) is a promising metal as a conductive filler as it is inexpensive and abundant. However, Cu particles are prone to oxidation, which significantly reduces the electrical conductivity, therefore, the surface of these particles must be protected from oxidation. To reduce surface oxidation and consequently improve the conductivity of Cu particles, their surface can be protected with silver (Ag), creating a core-shell (Cu@Ag)[3] structure. To improve conductivity of a non-conductive material, a network of conductive particles must be established. This

network forms at certain volume fraction, known as the "percolation threshold", which depends on various factors (type, shape, size of the filler, etc.). However, higher filler concentration can have a negative impact on the properties of the polymer matrix. In our previous study[2], where unmodified and modified Cu-based flakes were used as fillers in a polyethylene matrix, increased concentration of the flakes increased the hardness but drastically reduced the toughness, leading to the brittleness of the final composite.

The presented research is focus on the influence of different filler volume concentrations (0 – 40 vol.%.) of conductive silver-coated copper particles (Cu@Ag) incorporated into TPU polymer, where the rheological, morphological and electrical properties were investigated in order to determine the geometrical and electrical percolation thresholds.

EXPERIMENTAL

The composites were made of polyether-based thermoplastic polyurethane - TPU (Elastollan 1195A, BASF, Germany) with a density of ρ_{TPU} = 1.15 g/cm^3 and silver-coated copper flakes - Cu@Ag (eConduct Cu 340500, Eckart, Germany). The Cu@Ag flake-shaped particle size was d_{50} = 42 µm. The mass concentration, Φ_m, of Ag coating material on Cu particle was Φ_m = 5%. The TPU-based composites with different volume concentrations Cu@Ag filler, i.e., Φ_{vol} = 0 – 40 vol.%, were prepared by melt processing at 215 °C in a twin-screw extruder (Xplore Micro compounder MC 15 HT, The Netherlands), using a counter-rotating mode. For each composition, the dosing time was 5 min at a screw speed of 50 rpm and a mixing time of 5 min at a screw speed of 75 rpm. During mixing, the melt was purged with N_2 gas to prevent oxidation of the surface of the Cu@Ag particles. The TPU polymer was pre-dried at 90°C for 3 hours before the extrusion process. Subsequently, the melt was transferred into the injection molding piston, heated at 210 °C and then molded into a final shape with an injection pressure of 5-6 MPa for 10 s and holding pressure of 7-8 MPa (depending on the filler concentration) for an additional 10 s. Two different sample geometries were prepared for the characterization, i.e., disk-shaped samples for the rheological characterization with a diameter of 25 mm and a thickness of 1.5 mm, while DMA test bars with a length of 60 mm, a width of 10 mm and a thickness of 1 mm were produced for mechanical and electrical characterization.

The rheological analysis of the TPU-based composites was performed with a rheometer (MCR302, Anton Paar, Graz, Austria) at a constant temperature of 210 °C with a plate-plate sensor geometry (25 mm diameter) and a gap of 1 mm. Rotational tests under destructive shear conditions were performed using the triangular method. The viscoelastic properties of the investigated composites were determined by frequency sweep tests in the range of 100 Hz to 0.01 Hz. The measurements were performed in the linear viscoelastic range, using a strain excitation of 0.01-0.04%, depending on the particle concentration, while a strain excitation of 10% was used for pure TPU polymer. The results are presented as the average value of 3 replicates for each composite tested.

The dynamic mechanical analysis (DMA) was used to determine the mechanical reinforcement of the TPU-based composites filled with Cu@Ag particles. The tests were performed in bending mode using a 3-point bending sensor geometry in the temperature range of -10 °C to 70 °C with a heating rate of 3 °C/min under an inert nitrogen atmosphere by using a MCR702 rheometer (Anton Paar, Graz, Austria). Before measurements, all samples were annealed at 60 °C for 9 hours and cooled to room temperature at 0.1 °C/min in a nitrogen atmosphere. In addition, the measurements were carried out in the linear viscoelastic range with a strain excitation of 0.1%. The results of the DMA tests are presented as the average value of 3 repetitions for each composite tested.

The conductive performance of composites was determined at room temperature using a custom-built 4-wire DC measuring rig coupled with a Keithley 237 measure unit (Keithley Instruments, Solon, OH, USA). Conductivity (σ) through the sample was determined by measuring current at excitation voltages ranging from -120 V to 120 V. Conductivity results represent an average of 3 repetitions for each material.

RESULTS

Optical microscopy

The surface microstructure of the injection molded TPU/Cu@Ag composites at volume concentrations (Φ_{vol} = 0 – 40 vol.%) was investigated using optical microscopy (AxioScope 2, Carl Zeiss, Germany). Figure 1 shows that the amount of irregular, flaky Cu@Ag particles on the surface increases with increasing volume concentration of the filler, which also increased the roughness of the moulded sample. It was also found that the surfaces of the flakes were not uniformly covered with Ag coating material as the Cu uncoated particles have a copper-like colour, the Cu@Ag flakes appear grey.

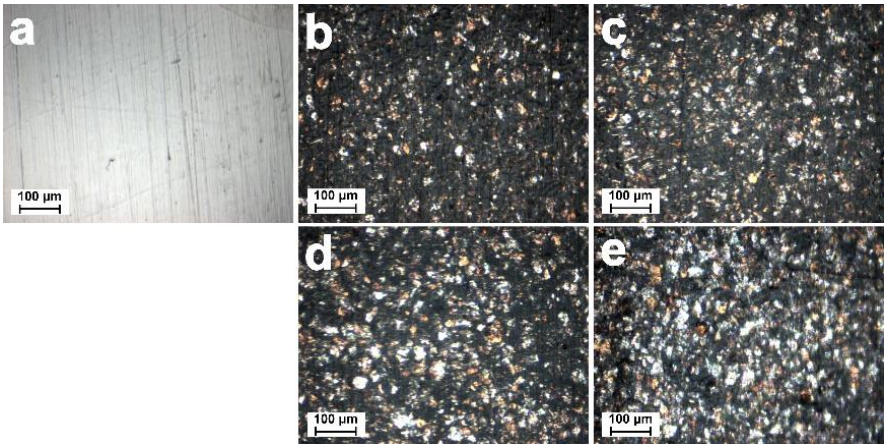

FIGURE 1: TPU-based composites with different volume concentrations of the Cu@Ag fillers.

Oscillatory tests: frequency sweep

The particle interactions in polymer composites and its network formation was observed with rheological characterization. Viscoelastic behaviour, i.e., storage modulus (G′), loss modulus (G″) and complex viscosity (η^*) were determined as a function of frequency in the linear viscoelastic range at a constant temperature of 210 °C.

The frequency-dependent viscoelastic response of TPU/Cu@Ag filled composites are presented in Fig. 2A. The results show that in the entire frequency range investigated the TPU exhibits a flow-like behavior (G″ > G′), while all composites exhibit a solid-like behavior (G′ > G″). The transition from liquid- (G″ > G′) to solid-like (G′ > G″) behaviour was only observed with the addition of 10 vol.% of Cu@Ag particles to TPU polymer, where the cross-over frequency ω_{co} (G′ = G″) was 11.4 Hz. The dynamic moduli of the composites were significantly higher than those of pure TPU and increased with the increasing concentration of Cu@Ag particles, indicating a significant influence of particles in the TPU polymer. The high increase in G′ indicates the geometrical entanglement of particles and the formation of a network in the polymer matrix. Moreover, the viscous response of the composite was hindered and an increase in G″ by five orders of magnitude at the highest concentration of Cu@Ag particles was observed. Figure 2B shows that at low frequencies, the highly filled Cu@Ag/TPU composites

exhibited significantly higher complex viscosity (six orders of magnitude) than pure TPU polymer. This is consistent with the established understanding that particle-particle interactions and network formation dominate the viscoelastic properties of polymer composites at low frequencies[4].

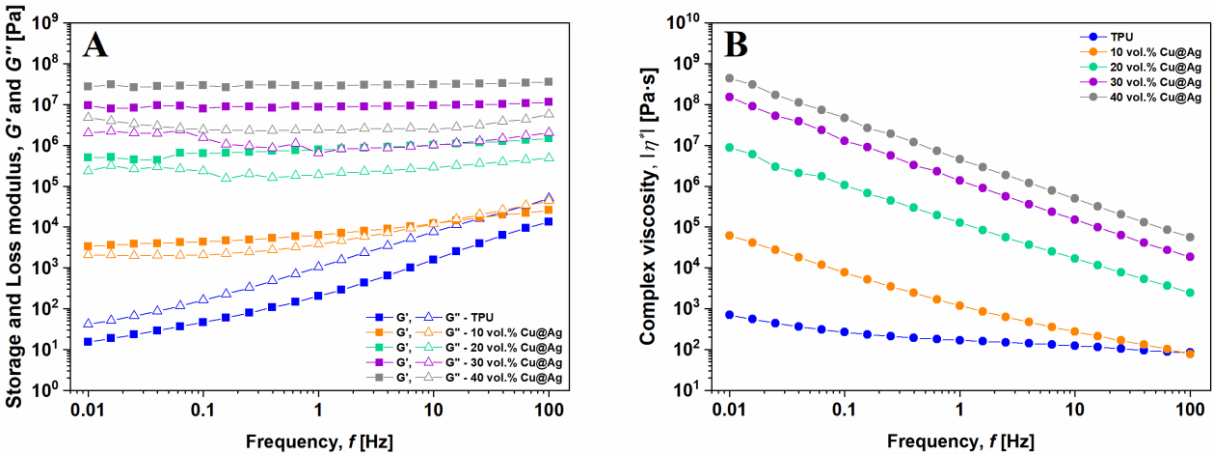

FIGURE 2: Viscoelastic behaviour of TPU-based composites with different volume concentrations of the Cu@Ag fillers.

Network formation in the investigated composites was evaluated by analyzing the low-frequency region, i.e., complex viscosity (η^*) at 0.01 Hz, as a function of Cu@Ag volume concentration Φ_{vol} (Fig 3). The results show that the critical volume concentration (geometrical percolation point) at which the particles become geometrically entangled in the polymer matrix was $\Phi_{v,crit}$ ~15 vol.%. This value is twice as high as for the LDPE polymer matrix filled with Cu@Ag flakes ($\Phi_{vol,crit}$ ~ 7.5 vol.%) and the same as for LDPE/Cu composite[2]. After the network was established (above $\Phi_{vol,crit}$), the long-range interactions between the particles predominate, which significantly influence the viscoelastic response and functionality of the material.

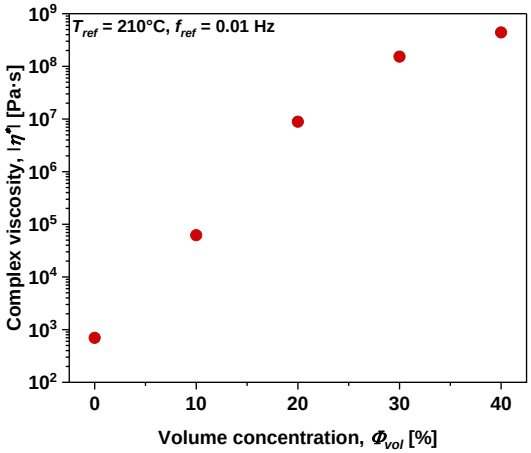

FIGURE 3: Viscoelastic behaviour of TPU-based composites with different volume concentrations of the Cu@Ag filler.

Mechanical behaviour

Dynamic Mechanical Analysis (DMA) is a powerful tool for characterizing the mechanical properties of TPU-based polymer composites. In the temperature range between -10°C and 70°C, the influence of the addition of Cu@Ag filler on the mechanical properties was determined using the 3-point bending mode. The measurements were performed under low load

(linear viscoelastic region), which resulted in small deformations that did not damage the sample.

The temperature dependence of the extensional storage (E') and extensional loss (E'') modulus of Cu@Ag filled composites at different filler concentrations is presented in Fig. 4A. For all composites, E' was approximately one decade higher than E'' over the whole temperature range investigated. The increase in modulus is related to the presence of particles that contribute to the reinforcement of the TPU polymer matrix by forming a network. It was also observed that E' decreased with increasing temperature for all samples, reflecting a transition from a rigid to a more flexible state. The difference in E' and E'' ratio with increasing temperatures suggests that TPU polymer has more soft segments. The glass transition point of soft segments ($T_{g,soft}$) for TPU was at -36.2°C (determined from differential scanning calorimetry (DSC) - not shown here). Below T_g the polymer behaves like a rigid material with high stiffness. Above T_g, polymer becomes more flexible and exhibits viscoelastic behaviour, with the hard segments in the TPU contributing to maintaining structural integrity at higher temperatures.

The values of *E' and E''* moduli increased with the increase in the filler content at the same temperature (Fig. 4B). Increasing the filler content enhances the interfacial adhesion between the filler and matrix, leading to higher matrix stiffness and improved stress transfer at the interfaces.

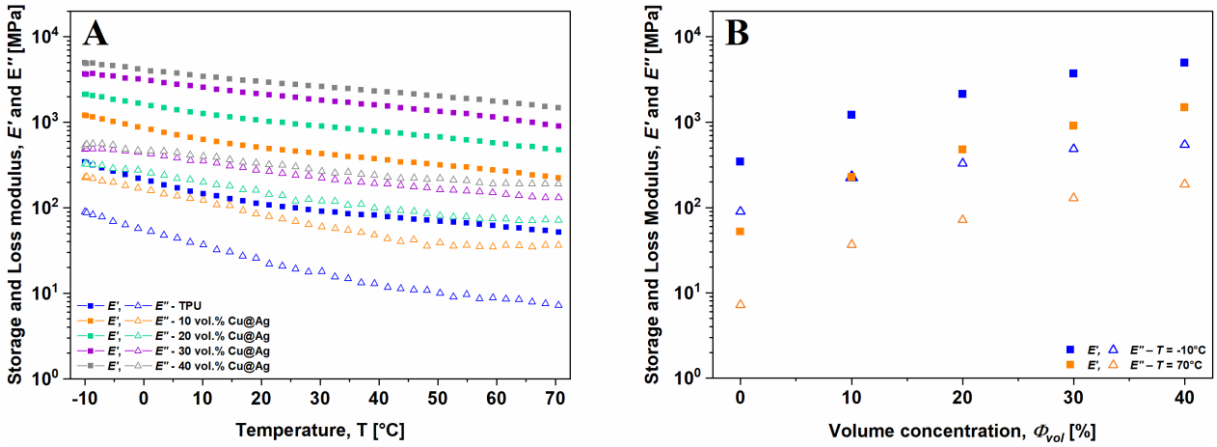

FIGURE 4: Viscoelastic properties of TPU-based composites (A) and *E', E''* values at -10°C and 70°C (B) at different volume concentrations of the Cu@Ag filler.

Electrical conductivity

The electrical conductivity of TPU-based composites filled with different volume concentrations of Cu@Ag particles is shown in Fig. 5. The results indicate that the pure TPU polymer is non-conductive, while the addition of conductive particles to the polymer matrix increases the conductivity of the composite. The conductive network starts to develop at 10 vol.%, while a higher increase was observed at 20 vol.% Cu@Ag loading. The maximum conductivity (46.7 S/m) was reached at 40 vol.% Cu@Ag loading.

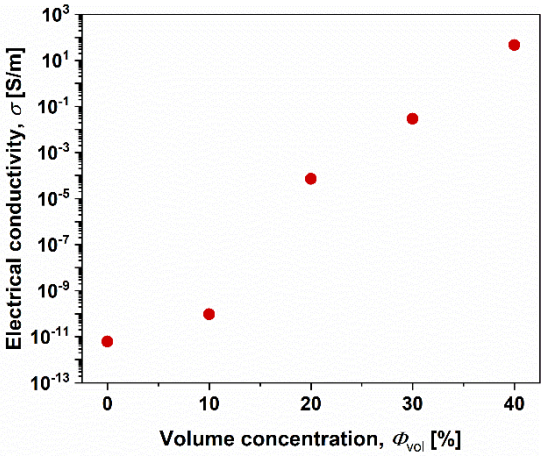

FIGURE 5: Electrical conductivity of TPU-based composites with different volume concentrations of the Cu@Ag filler.

According to the percolation theory, the transition from insulator to conductor in the polymer or polymer composite is determined by the percolation threshold, i.e., the critical volume concentration at which the conductive pathways are formed in the polymer composite. For the TPU polymer matrix filled with Cu@Ag particles, the percolation threshold was observed at pigment loading of ~15 vol.%. Similar values for electrical conductivity have already been observed when copper particles were added to semi-crystalline low-density polyethylene (LDPE) polymer[2,5,6] and to amorphous PMMA[7], where it was reported that the percolation threshold begins to establish between 10 and 20 vol.% copper. Kim et al. investigated the addition of copper particles to CNT/TPU composite material used as a conductive filament for 3D printing. The addition of copper particles further reduced the resistivity at lower CNT concentrations, but this effect decreased at higher concentrations. The volume resistivity (ρ) of the polymer composite TPU/CNT (19.2 wt.%)/Cu (23 wt.%) was 0.12 Ω/cm. However, at high concentrations of CNT and Cu fillers, the composites become more brittle[8].

Several factors influence the concentration of filler particles required to achieve conductive pathways within the composite material (percolation threshold), including particle size and shape, the presence of surface coatings on the copper particles, and the type of polymer used. Furthermore, the higher concentration (i.e., 10 wt.%) of the silver coating on the copper flakes improves the electrical percolation threshold, which decreased to 7.5 vol.%[2]. This means that a better oxidation protection of the copper pigment particles has formed, thus enhancing the formation of electrical pathways through the polymer composite.

CONCLUSION

This study investigated the influence of silver-coated copper (Cu@Ag) filler particles on the rheological behavior, mechanical properties, and electrical conductivity of thermoplastic polyurethane (TPU) composites. The composites were prepared with different concentrations of Cu@Ag filler, ranging from 0 to 40 vol.%, by twin-screw extrusion. The samples were afterwards injection molded into suitable shapes for further characterization.

The incorporation of Cu@Ag filler into TPU polymers significantly improves their viscoelastic properties, as observed by increased storage (G') and loss (G") moduli as well as complex viscosity compared to neat TPU. This improvement is due to the fact that the filler reduces the free volume of the polymer and thus restricts chain mobility while promoting

macromolecular adsorption on the filler surface, further hindering chain movement and thus increasing viscoelasticity. The DMA analysis has shown that the mechanical properties of TPU/Cu@Ag composites were significantly affected by increasing filler concentration and temperature. The non-conductive TPU polymer becomes electrically conductive as the volume concentration of the Cu@Ag filler increases, reaching a maximum value of $\sigma = 46.7$ S/m at the highest volume concentration of filler. The electrical percolation threshold of TPU/Cu@Ag composites was determined to be at ~15 vol.% filler concentration. These results highlight the crucial role of filler concentration in tailoring TPU composites for applications requiring balanced mechanical and electrical performance, used for flexible electronics and EMI shielding.

ACKNOWLEDGMENTS

The authors acknowledge the financial support of the Slovenian Research Agency (research core funding No. P2-0264).

REFERENCES

(1) Oseli, A.; Tomković, T.; Hatzikiriakos, S. G.; Vesel, A.; Arzenšek, M.; Rojac, T.; Mihelčič, M.; Slemenik Perše, L. Carbon Nanotube Network Formation and Configuration/Morphology on Reinforcing and Conductive Performance of Polymer-Based Nanocomposites. *Compos. Sci. Technol.* **2023**, *237*, 110010. https://doi.org/https://doi.org/10.1016/j.compscitech.2023.110010.

(2) Mihelčič, M.; Oseli, A.; Rojac, T.; Slemenik Perše, L. Surface Modification of Copper-Based Flakes for Conductive Polymer Composites. *Polymers*. 2024. https://doi.org/10.3390/polym16121620.

(3) Cao, X. G.; Zhang, H. Y. Preparation of Silver-Coated Copper Powder and Its Oxidation Resistance Research. *Powder Technol.* **2012**, *226*, 53–56. https://doi.org/10.1016/j.powtec.2012.04.012.

(4) Rueda, M. M.; Auscher, M. C.; Fulchiron, R.; Périé, T.; Martin, G.; Sonntag, P.; Cassagnau, P. Rheology and Applications of Highly Filled Polymers: A Review of Current Understanding. *Prog. Polym. Sci.* **2017**, *66*, 22–53. https://doi.org/10.1016/j.progpolymsci.2016.12.007.

(5) Molefi, J. A.; Luyt, A. S.; Krupa, I. Comparison of the Influence of Copper Micro- and Nano-Particles on the Mechanical Properties of Polyethylene/Copper Composites. *J. Mater. Sci.* **2010**, *45* (1), 82–88. https://doi.org/10.1007/s10853-009-3894-9.

(6) Alvarez, M. P.; Poblete, V. H.; Pilleux, M. E.; Fuenzalida, V. M. Submicron Copper-Low-Density Polyethylene Conducting Composites: Structural, Electrical, and Percolation Threshold. *J. Appl. Polym. Sci.* **2006**, *99* (6), 3005–3008. https://doi.org/https://doi.org/10.1002/app.23013.

(7) Poblete, V. H.; Alvarez, M. P. Mechanical, Electrical, and Glass Transition Behavior of Copper–PMMA Composites. *Crystals*. 2023. https://doi.org/10.3390/cryst13030368.

(8) Kim, H.; Yoo, H.; Shin, S.; Cho, J.; Han, S.-W.; Lee, I. Development of a TPU/CNT/Cu Composite Conductive Filament with a High CNT Concentration. *Int. J. Precis. Eng. Manuf.* **2023**, *24* (2), 265–271. https://doi.org/10.1007/s12541-022-00712-4.

Food and Biopolymer Rheology

RHEOLOGY IN FIBRE FORMATION FOR MEAT-ANALOGUES DATA ANALYSIS OF PROTEIN MELT RHEOLOGY DATA

Sandra Barman[1], Erik Kaunisto[1] and Mats Stading[1,2]

[1]RISE Research Institutes of Sweden, Gothenburg, Sweden
[2]Chalmers University of Technology, Gothenburg, Sweden

ABSTRACT

Global meat consumption increased four-fold during the last fifty years, while population doubled[1]. Even if the increase in European meat consumption has slowed (currently 80 kg per capita, twice the world average), it is forecasted to increase by 10% more to 2030[2–4]. The increase in meat eating is also nutritionally alarming as excessive consumption has been linked to health problems, such as coronary heart disease and certain cancers[5].

Fibrous, meat-like analogues are today commercially produced from soy, pea and wheat, utilizing an extruder to form a protein melt at high moisture content, high temperature and high pressure with subsequent active cooling on exit. A common denominator for the fibre formation in meat-analogues and plastics is that it is known **how** to produce the fibres but not exactly **why** they are formed. Consequently, it is still difficult to utilize the full potential of these techniques.

The current hypothesis on the mechanisms responsible for the fibre formation contribute to understanding but are not sufficient to fully describe the formation and cannot be used to predict fibre formation ability of protein melts thus hampering the use of more sustainable protein sources. Overall, the hypotheses range from "physical"[6–8], describing mechanisms in terms of fluid dynamics, heat transfer and phase separation, to "chemical" emphasizing the chemical interactions between protein chains or polymer crystallites.

This contribution will focus on rheology of the protein melts, and especially on how to use state-of-the-art statistical analysis to determine the influence of temperature, protein and moisture content on rheological properties of the melts.

INTRODUCTION

The food chain is responsible for 25% of global greenhouse gas emissions, with meat production alone accounting for 14.5%[9]. Food production heavily relies on natural resources, and 75% of arable land in Europe and North America is dedicated to meat production. Between 1961 and 2009, global meat consumption doubled, and with the growing population, it is expected to continue rising until at least 2050[2]. This trend is concerning from a nutritional standpoint, as excessive meat consumption has been linked to health issues such as coronary heart disease and certain cancers[5,10].

In the past five years, sales of plant-based meat analogues have surged, despite production methods being established since the early 1990s[11]. Today, fibrous analogues are commercially produced from soy, pea protein, and wheat gluten protein using an extruder to create a protein melt at high moisture content, temperature, and pressure, followed by active cooling upon exit[12–14]. These products are commonly known as High-Moisture Meat Analogues (HMMA). While the production process for HMMA fibres is understood, the exact mechanisms behind their formation remain unclear, limiting the full potential of these techniques.

This contribution will focus on the evaluation of rheological data of plant-protein melts[15] in order to determine the contribution of temperature, protein and moisture content using state-of-the-art statistical analysis.

MATERIAL AND METHODS

Sample preparation

Pea protein isolate with 86% protein content, (Roquette Pisane M9, Lestrem, France) was mixed with 15% pea fibre (Cosucra Swelite Warcoing, Hainaut, Belgium) and fed into an extruder (Brabender TwinLab-F 20/40, Duisburg, Germany) where water was added to 60-68% of the total weight. The mixture was heated and sheared in the extruder to 100°C to form a melt and extruded into a 13 mm cylinder which was air cooled instead of going into the cooling die, se **Fig. 1**. The same mixture is known to form a fibrous structure when heated to 150°C with subsequent cooling to ~80° in the cooling die.

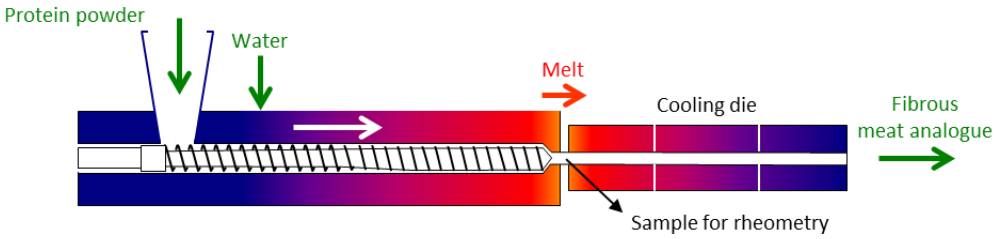

FIGURE 1: Principle of meat HMMA extrusion and sample preparation.

Rheometry

An HR 30 rheometer (TA Instruments, New Castle, DE, USA) was used for Small Amplitude Oscillatory Shear (SAOS) analysis, equipped with a 25 mm-diameter parallel plate system. Both plates were temperature controlled, and the measuring system was enclosed in a solvent-trap enclosure. Slices 13 mm in diameter and 2 mm thick were cut using a vacuum holder[16] and placed in the measuring gap. The gap was actively adopting to changes in samples volume with temperature. Mechanical spectra at 0.1-30 Hz were recorded during heating at 10°C intervals to give complex modulus as a function of angular frequency.

Statistical modelling

A variety of machine and statistical learning methods are available for analysing and interpreting data of the type presented in this study[17,18]. These range from classical methods such as linear regression and ANOVA, to more contemporary methods including regularized regression, random forests and neural networks.

We will use models from the generalized additive mixed model (GAMM) framework[19,20]. The specific formulation of model components within this framework depends on whether a frequentist or Bayesian approach is taken. In essence, however, the GAMM framework allows

for including smooth components as functions of predictor variables. These can be both parametric and non-parametric, and linear and non-linear. Regularization of smooth, non-linear effects ensure that models are not overfit to data. The framework also accommodates non-Gaussian outcome distributions and supports modelling hierarchical and time-dependent structures using random components. The GAMM framework functions as an extension of classical statistical techniques, such as linear regression and ANOVA, encompassing these as special cases[21,22].

GAMM offer greater flexibility than classical statistical regression models, enabling the extraction of complex patterns within data. There is however a trade-off between flexibility and interpretability[17,23]. Compared to highly flexible machine learning methods such as random forests or neural networks, GAMMs tend to be more interpretable while still capturing nonlinear relationships. While highly flexible models like the mentioned machine learning methods may be preferable for large datasets due to their predictive power, for medium sized datasets such as the one presented here, GAMMs strike a good balance between flexibility and interpretability.

We formulate two models to capture the influence of temperature (T), moisture content (MC), protein concentration (PC) and experiment (E). Both models are formulated related to $1/T$ and $1/MC$ due to connections with physically motivated Arrhenius equations. The first model includes non-linear smooth effects of $1/T$ and $1/MC$ and random effects of PC and E, formulated as

$$\log(G_i^*) = f_T(1/T_i) + f_{MC}\left(1/MC_{E_i}\right) + \mu_{PC_i} + \mu_{E_i} + \epsilon_i. \qquad (M1)$$

Each individual observation is indexed by $i = 1, \dots, 252$. For every observation i, the corresponding complex modulus G_i^* is recorded, along with the temperature T_i at which the measurement was made. Additionally, each observation is linked to one of 42 experiments, denoted by an experiment identifier $E_i \in (1, \dots, 42)$. Associated with each experiment are two variables: moisture content MC_{E_i} and protein concentration PC_{E_i}. In the model, f_T and f_{MC} represent smooth functions of the inverse temperature and inverse moisture content, respectively. The terms μ_{PC_i} and μ_{E_i} denote random effects, capturing variation by fitting individual intercepts for each protein concentration level and each experiment. Residual errors ϵ_i are assumed to follow a normal distribution. Note that without the components f_T and f_{MC}, model (M1) reduces to a classic ANOVA model.

The second model instead includes linear effects of $1/T$ and $1/MC$,

$$\log(G_i^*) = \beta_T/T_i + \beta_{MC}/MC_{E_i} + \mu_{PC_i} + \mu_{E_i} + \epsilon_i. \qquad (M2)$$

Variable ranges used in the experiments are $T = 40$, 50, 60, 70, 80, 90°C for temperature and $PC = 75\%$, 80%, 85% for protein concentration. Five levels of added water were recorded, 60, 62, 64, 66 and 68%, and moisture content MC was recorded for each experiment.

This setup of using models of increasing complexity is a standard method for evaluating how much complexity is needed in a model[24]. A third model formulation is possible, where both linear components $1/T$ and $1/MC$ and non-linear components $f_T(1/T)$ and $f_{MC}(1/MC)$. We denote this model $(M3)$. Model $(M1)$ and $(M3)$ are in practice the same. Model formulation $(M3)$ has the advantage that the model $(M3)$ is nested within (M3), which simplifies assessment of whether the inclusion of non-linear components is warranted.

The models are fitted using the R package *mgcv*[25,26]. The adjusted R^2_{adj} is used as a measure of model fit. To quantify the contribution from each predictor, a model with (full model) and

without (sub-model) the predictor is fitted, and the difference in R^2_{adj} between the two models is used to quantify the contribution from the predictor. The difference is denoted δR^2_{adj}. More details are available in Tsegaye et al[15].

RESULTS AND DISCUSSION

Statistical analysis

The statistical analysis allows us to quantify the size and statistical significance of effects of individual variables, the non-linear nature of each effect, and potential interactions between variables. We also assess the importance of allowing for non-linear effects compared to using linear effects.

Table 1 and Table 2 shows the importance (R^2_{adj}) and statistical significance (p-value) of each variable in model (M1) and model (M2), respectively (Table 1 and Table 2 are reproduced from Tsegaye et al.[15]).

Evaluating if the non-linear smooth effects are actually needed is in part a subjective judgement. The non-linear components of model (M3) are statistically significant (p-value $< 1e-16$), but in general statistical significance does not necessarily imply practical significance. Comparing the model with non-linear components (model (M1)) and the model with linear components (model (M2)) in time and moisture content, model (M1) has R^2_{adj} 99.2% while model (M2) has R^2_{adj} 98.3%. Thus, there is definitely a non-linear component in the fitted relationships, but we leave to the reader the decision of whether the effect of the non-linear component is considerable enough to warrant choosing model (M1) over the simpler model (M2). Fig. 1a) and b) provides more detail about the fitted non-linear effects and how they differ from linear effects (Fig. 1 is reproduced from the Supplementary material of Tsegaye et al.[15].).

The non-linear effects in Fig. 1 show that the effect of temperature, $f_T(1/T) \in [-0.48,0.61]$, is roughly three times the size of the effect of moisture content, $f_{MC}(1/MC) \in [-0.17,0.11]$). The size of the effect of experiment, $\mu_{E_i} \in [-0.18,0.27]$), is between moisture content and temperature. This also fits with the ordering shown in Table 1.

This means that effects we have not measured have a relatively large impact on the variation of the complex modulus G^* between different experiments. When controlling for these effects using μ_{E_i}, however, the complex modulus is explained almost fully by temperature and moisture content. Note that the random effect μ_{E_i} serves the same function as random effects in ANOVA, which controls for grouping / hierarchical structure in the data is not explicitly modelled using covariates.

This indicates that unmeasured factors significantly contribute to the variability observed in the variation of rheological behaviour across experiments. However, once these influences are accounted for through the inclusion of the random term μ_{E_i}, the variation can be largely explained by temperature and moisture content as indicated by the high R^2_{adj}-values. Importantly, μ_{E_i} functions similarly to random effects in ANOVA, taking into account grouped or hierarchical nature of the data when that structure is not directly captured through explicitly included variables like temperature and moisture content.

To conclude, we show that regression within the GAMM framework, which extends classical ANOVA and linear regression, can reveal non-linear, physically motivated relationships between experimental variables and rheological behaviour. We find that relationships involving temperature T and moisture content MC approximate Arrhenius type

behaviour, i.e. they are log-linear with respect to $1/T$ and $1/MC$, even when non-linear effects are permitted. The strength of the effect is found to follow temperature > moisture content > protein concentration, with protein concentration showing no statistically significant effect.

Table 1 Non-linear mixed models (model (M1)).

Model component	δR^2_{adj}	p-value
Temperature	88.0 %	$< 10^{-16}$
Moisture content	3.6 %	0.0002
Protein content	0.1 %	0.79
Experiment	7.8 %	$< 10^{-16}$

Table 2 Linear mixed models (model (M2)).

Model component	δR^2_{adj}	p-value
Temperature	87.9 %	$< 10^{-16}$
Moisture content	3.6 %	0.00005
Protein content	0.1 %	0.82
Experiment	9.4 %	$< 10^{-16}$

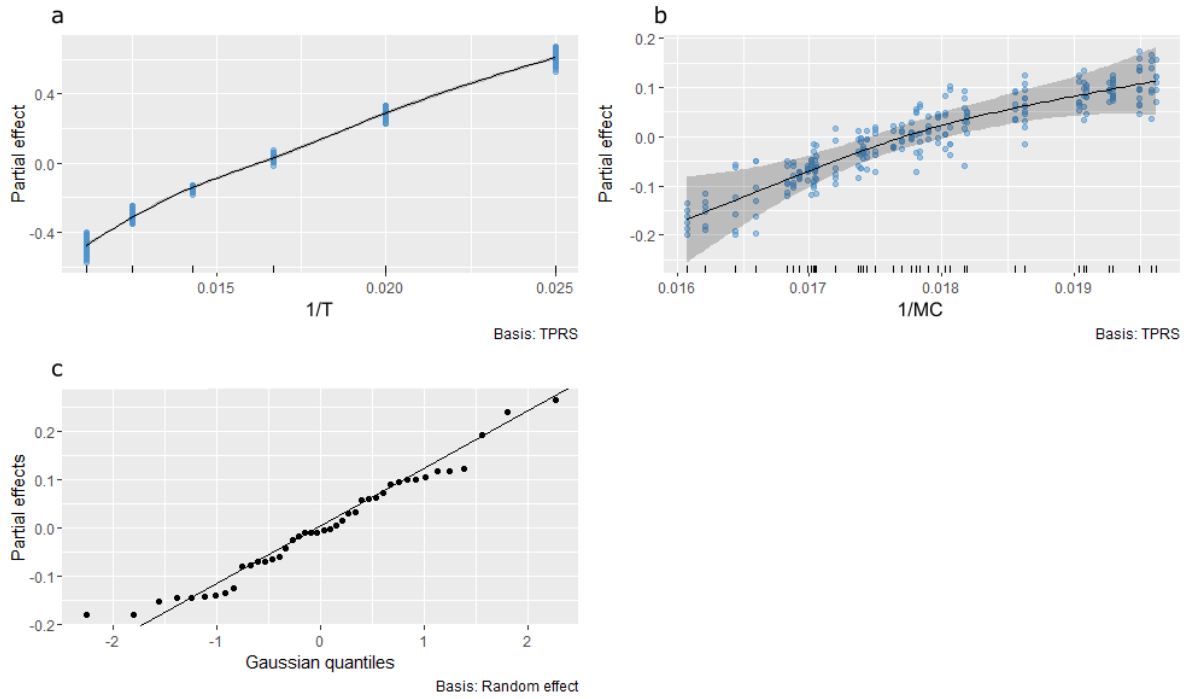

FIGURE 1: Fitted non-linear effects for (a) temperature, $f_T(1/T)$ and (b) moisture content, $f_{MC}(1/MC)$,, and quantile-quantile plot of (c) the random effect μ_{E_i} of experiment. Panels (a) and (b) show partial residuals (blue dots) and confidence bounds for the fitted non-linear effect. The confidence bounds are so close to the fitted non-linear effect in (a) that they are not visible. Fitted effects for protein concentration are excluded from the visualization as it was not significant. The figure was created using the *draw*-function from the *gratia*-package in R[27].

REFERENCES

(1) Weis, T. SFSGEC - Meatification and the Madness of the Doubling Narrative. *Can. Food Stud. Rev. Can. Études Sur Aliment.* **2015**, *2* (2), 296–303. https://doi.org/10.15353/cfs-rcea.v2i2.105.

(2) Steinfeld, H. *Livestock's Long Shadow - Environmental Issues and Options*; Food and Agriculture Organization of the United Nations (FAO), 2006. http://www.fao.org/3/a0701e/a0701e00.htm (accessed 2021-03-29).

(3) Westhoek, H. *The Protein Puzzle - The Consumption of Meat, Dairy and Fish in the European Union*; PBL Netherlands Environmental Assessment, 2011.

(4) *FAOSTAT*. FAOSTAT. http://faostat.fao.org/ (accessed 2010-09-23).

(5) Tammi, R.; Kaartinen, N. E.; Harald, K.; Maukonen, M.; Tapanainen, H.; Smith-Warner, S. A.; Albanes, D.; Eriksson, J. G.; Jousilahti, P.; Koskinen, S.; Laaksonen, M. A.; Heikkinen, S.; Pitkäniemi, J.; Pajari, A.-M.; Männistö, S. Partial Substitution of Red Meat or Processed Meat with Plant-Based Foods and the Risk of Colorectal Cancer. *Eur. J. Epidemiol.* **2024**, *39* (4), 419–428. https://doi.org/10.1007/s10654-024-01096-7.

(6) Sägesser, C.; Mair, T.; Braun, A.; Dumpler, J.; Fischer, P.; Mathys, A. Application of a Shear Cell for the Simulation of Extrusion to Test the Structurability of Raw Materials. *Food Hydrocoll.* **2025**, *160*, 110736. https://doi.org/10.1016/j.foodhyd.2024.110736.

(7) Kaunisto, E.; Wassén, S.; Stading, M. A Thermodynamical Finite Element Model of the Fibre Formation Process during Extrusion of High-Moisture Meat Analogues. *J. Food Eng.* **2024**, *362*, 111760. https://doi.org/10.1016/j.jfoodeng.2023.111760.

(8) Sandoval Murillo, J. L.; Osen, R.; Hiermaier, S.; Ganzenmüller, G. Towards Understanding the Mechanism of Fibrous Texture Formation during High-Moisture Extrusion of Meat Substitutes. *J. Food Eng.* **2019**, *242*, 8–20. https://doi.org/10.1016/j.jfoodeng.2018.08.009.

(9) Gerber, P. J.; Steinfeld, H.; Henderson, B.; Mottet, A.; Opio, C.; Dijkman, J.; Falcucci, A.; Tempio, G. *Tackling Climate Change through Livestock: A Global Assessment of Emissions and Mitigation Opportunities.*; Food and Agriculture Organization of the United Nations (FAO): Rome, 2013. https://www.cabidigitallibrary.org/doi/full/10.5555/20133417883 (accessed 2025-04-22).

(10) Glenn, A. J.; Wang, F.; Tessier, A.-J.; Manson, J. E.; Rimm, E. B.; Mukamal, K. J.; Sun, Q.; Willett, W. C.; Rexrode, K. M.; Jenkins, D. J.; Hu, F. B. Dietary Plant-to-Animal Protein Ratio and Risk of Cardiovascular Disease in 3 Prospective Cohorts. *Am. J. Clin. Nutr.* **2024**, *120* (6), 1373–1386. https://doi.org/10.1016/j.ajcnut.2024.09.006.

(11) Cheftel, J. C.; Kitagawa, M.; Quéguiner, C. New Protein Texturization Processes by Extrusion Cooking at High Moisture Levels. *Food Rev. Int.* **1992**, *8* (2), 235–275. https://doi.org/10.1080/87559129209540940.

(12) Jones, O. G. Recent Advances in the Functionality of Non-Animal-Sourced Proteins Contributing to Their Use in Meat Analogs. *Curr. Opin. Food Sci.* **2016**, *7*, 7–13. https://doi.org/10.1016/j.cofs.2015.08.002.

(13) Kyriakopoulou, K.; Keppler, J. K.; Van Der Goot, A. J.; Boom, R. M. Alternatives to Meat and Dairy. *Annu. Rev. Food Sci. Technol.* **2021**, *12* (1), 29–50. https://doi.org/10.1146/annurev-food-062520-101850.

(14) Krona, A.; Klose, F. P.; Gold, J.; Kadar, R.; Stading, M. Developing Cultured Meat Scaffolds of Extruded Vegetable-Based Proteins. *Annu Trans. Nord. Rheol Soc* **2017**, *25*, 311–313.

(15) Tsegaye, B.; Barman, S.; Bovagne, L.; Ellwanger, F.; Kaunisto, E.; Lorén, N.; Kádár, R.; Stading, M. Rheological Properties of Pea Protein Melts Used for Producing Meat Analogues. *Appl. Rheol.* **2025**, *35* (1), 20250036. https://doi.org/10.1515/arh-2025-0036.

(16) Stading, M.; Langer, R. Mechanical Shear Properties of Cell-Polymer Cartilage Constructs. *Tissue Eng.* **1999**, *5* (3), 241–250. https://doi.org/10.1089/ten.1999.5.241.

(17) Hastie, T.; Friedman, J.; Tibshirani, R. *The Elements of Statistical Learning*; Springer Series in Statistics; Springer New York: New York, NY, 2001. https://doi.org/10.1007/978-0-387-21606-5.

(18) James, G.; Witten, D.; Hastie, T.; Tibshirani, R.; Taylor, J. *An Introduction to Statistical Learning: With Applications in Python*; Springer Texts in Statistics; Springer International Publishing: Cham, 2023. https://doi.org/10.1007/978-3-031-38747-0.

(19) Hastie, T.; Tibshirani, R. Generalized Additive Models. *Stat. Sci.* **1986**, *1* (3), 297–310.

(20) Ruppert, D.; Wand, M. P.; Carroll, R. J. *Semiparametric Regression*; Cambridge university press, 2003.

(21) Mundo, A. I.; Tipton, J. R.; Muldoon, T. J. Generalized Additive Models to Analyze Nonlinear Trends in Biomedical Longitudinal Data Using R: Beyond Repeated Measures ANOVA and Linear Mixed Models. *Stat. Med.* **2022**, *41* (21), 4266–4283. https://doi.org/10.1002/sim.9505.
(22) Yu, Z.; Guindani, M.; Grieco, S. F.; Chen, L.; Holmes, T. C.; Xu, X. Beyond t Test and ANOVA: Applications of Mixed-Effects Models for More Rigorous Statistical Analysis in Neuroscience Research. *Neuron* **2022**, *110* (1), 21–35. https://doi.org/10.1016/j.neuron.2021.10.030.
(23) Caruana, R.; Lou, Y.; Gehrke, J.; Koch, P.; Sturm, M.; Elhadad, N. Intelligible Models for HealthCare: Predicting Pneumonia Risk and Hospital 30-Day Readmission. In *Proceedings of the 21th ACM SIGKDD International Conference on Knowledge Discovery and Data Mining*; ACM: Sydney NSW Australia, 2015; pp 1721–1730. https://doi.org/10.1145/2783258.2788613.
(24) Wood, S. N. *Generalized Additive Models: An Introduction with R*; chapman and hall/CRC, 2017.
(25) Wood, S. N. Fast Stable Restricted Maximum Likelihood and Marginal Likelihood Estimation of Semiparametric Generalized Linear Models. *J. R. Stat. Soc. Ser. B Stat. Methodol.* **2011**, *73* (1), 3–36. https://doi.org/10.1111/j.1467-9868.2010.00749.x.
(26) Wood, S. N. Stable and Efficient Multiple Smoothing Parameter Estimation for Generalized Additive Models. *J. Am. Stat. Assoc.* **2004**, *99* (467), 673–686. https://doi.org/10.1198/016214504000000980.
(27) Simpson, G. L. Gratia: Graceful Ggplot-Based Graphics and Other Functions for GAMs Fitted Using Mgcv. *R Package Version 0100* **2024**.

Polymer Rheology

A NOVEL STRAIN HARDENING INDEX SHI FOR LONG-CHAIN BRANCHED POLYMER MELTS

Manfred H. Wagner[1] and Valerian Hirschberg[1,2]

[1]Polymer Engineering/Polymer Physics, Berlin Institute of Technology (TU Berlin), Ernst-Reuter-Platz 1, 10587 Berlin, Germany
[2]Institute for Technical Chemistry, Technical University Clausthal, Arnold-Sommerfeld-Str. 4, 38678 Clausthal-Zellerfeld, Germany

ABSTRACT

Strain hardening of polymer melts in extensional flows is considered as a desirable rheological feature because it stabilizes homogeneity of free surface flows such as, e.g., film blowing, blow molding and fiber spinning. Relating strain hardening to molecular characteristics has been a long-standing challenge in rheology, but while long-chain branching (LCB) is known to be a decisive feature to enhance strain hardening, a quantitative relation between strain hardening and molecular topology is still missing. We propose a novel strain hardening index SHI that can be used to assess the strain hardening behaviour and to compare strain hardening of polymer melts with different topologies and different chemistries investigated at different temperatures.

INTRODUCTION

The standard method of measuring strain hardening is via the strain hardening factor (SHF), i.e., by taking the ratio of the elongational stress growth coefficient to the linear-viscoelastic start-up viscosity. The SHF indicates the change of *transient* strain hardening with strain rate in start-up elongational flow at a prescribed Hencky strain and at a particular experimental temperature for the specific polymer system considered. However, as the SHF does not contain a material time constant, it cannot be used to compare the strain hardening potential of polymer systems with different chemistries and different topologies.

Recent progress in living anionic polymerization technology has enabled the synthesis of well-defined model polystyrene (PS) polymer systems such as pom-pom polymers (**Fig. 1**) in quantities allowing extensive elongational characterization. We have shown that the elongational viscosity of these systems is well described by the Hierarchical Multi-mode Molecular Stress Function (HMMSF) model or the Enhanced HMMSF (EHMMSF) model[1] up to the steady-state elongational viscosity or in case of fracture, the maximal elongational viscosity. These models take into account hierarchical relaxation and dynamic dilution of the backbone by the side arms. We consider the maximal elongational viscosity of pom-poms as a function of the Weissenberg number Wi_d based on the disengagement time. We show that the maximal elongational viscosity normalized by the zero-shear viscosity is a useful measure of strain hardening, and we define a novel strain hardening index SHI. We discuss the effect of

molecular topology, i.e. the effect of molecular weight of backbone as well as number and molecular weight of side arms on the strain hardening behaviour. In addition, we compare the strain hardening behaviour of pom-poms to the strain hardening of several polydisperse (commercial) LDPE melts. We show that the normalized elongational viscosity reaches a maximal value at $Wi_d \approx 2-8$, and we show that the experimentally measured strain hardening index SHI_m can be used to assess the strain hardening behaviour and to compare strain hardening of polymer melts with different topologies and different chemistries. From a one-mode HMMSF model, we derive a relation for the strain hardening index SHI, which is in nearly quantitative agreement with SHI_m up to SHI≈100.

MATERIALS

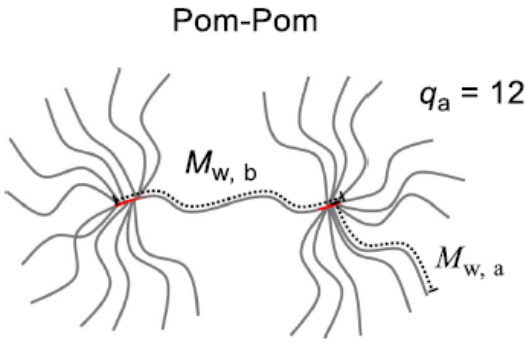

Fig. 1. Schematic representation of pom-poms.

A pom-pom polymer consists of a backbone chain of molecular weight $M_{w,b}$ with only one branch point at each end having q_a side arms of molecular weight $M_{w,a}$ (**Fig. 1**). We consider here the elongational viscosity of a series of 12 PS pom-poms as reported by Hirschberg et al.[2,3] comprising a wide range of $M_{w,a}$, $M_{w,b}$, and q_a (**Table 1**).

Table 1. Molecular characteristics of PS pom-poms.

Pom-Poms	**$M_{w,b}$ [kg/mol]**	**$M_{w,b}/M_n$ [-]**	**$M_{w,a}$ [kg/mol]**	**$M_{w,a}/M_n$ [-]**	**q_a [-]**	**M_w [kg/mol]**	**M_w/M_n [-]**
Pom-Pom $M_{w,b}$ – 2xq_a – $M_{w,a}$							
100k-2x12-24k	100	1.05	24	1.05	2x12	600	1.18
100k-2x12-40k	100	1.05	40	1.08	2x12	1060	1.16
100k-2x14-50k	100	1.05	50	1.20	2x14	1500	1.27
100k-2x22-25k	100	1.05	25	1.15	2x22	1200	1.15
220k-2x9-25k	220	1.06	25	1.08	2x9	670	1.08
220k-2x10-40k	220	1.06	40	1.10	2x10	1020	1.09
280k-2x22-22k	280	1.04	22	1.07	2x22	1248	1.15
400k-2x9-23k	400	1.10	23	1.14	2x9	814	1.15
400k-2x13-40k	400	1.10	40	1.15	2x13	1360	1.15
300k-2x24-40k	300	1.40	40	1.03	2x24	2220	1.40
100k-2x5-25k	100	1.05	25	1.05	2x5	350	1.12
220k-2x3-70k	220	1.06	70	1.04	2x3	640	1.11

The elongational rheology of the model PS pom-poms will be compared to the maximal viscosity of 6 commercial LDPE melts investigated by Wagner et al.[4] (2022) and Wagner and Hirschberg[1] (2023). The molecular characteristics of the LDPEs are summarized in **Table 2**.

Table 2. Characterization of LDPE melts.

Characteristics	**LDPE A**	**LDPE B**	**LDPE C**	**DOW150R**	**1840H-V**	**3020D**
Producer	Dow	Dow	Dow	Dow	BASF	BASF
M_w [kg/mol]	160	320	180	242	89	300
M_w/M_n	11	22	15	11	4	8
ρ_{RT} [g/cm^3]	0.920	0.919	0.918	0.921	0.920	0.94
MFR [dg/min]	2.0	8.5	3.9	0.18	-	-
E_a [kJ/mol]	65	65	65	-	-	64

THE STRAIN HARDENING INDEX SHI

As we will show in the following, the strain hardening index SHI depends on the product of two terms, one depending on the linear-viscoelastic (LVE) characterization of the melt in terms of the relaxation modulus *G(t)*, the other being a representative measure of stretch of chain segments. From the 1st and 2nd moment of the parsimonious relaxation time spectrum, the zero-shear viscosity η_0, the disengagement time τ_d and the steady-state compliance J_s^0 are obtained by

$$\eta_0 = \sum_i g_i \tau_i \tag{1a}$$

$$\tau_d = \frac{\sum_i g_i \tau_i^2}{\eta_0} \tag{1b}$$

$$J_s^0 = \frac{\sum_i g_i \tau_i^2}{\eta_0^2} \tag{1c}$$

To elucidate the essence of strain hardening, we simplify the HMMSF model to a one-mode model with relaxation time τ_d and modulus G_d representing the value of the relaxation modulus *G(t)* at time $t = \tau_d$,

$$G_d = G(t = \tau_d) \tag{2}$$

The stress tensor equation is then

$$\sigma(t) = \int_{-\infty}^{t} G_d / \tau_d \exp[-(t-t')/\tau_d] f^2(t,t') \mathbf{S}_{DE}^{IA}(t,t') dt' \tag{3}$$

and the evolution of stretch f is given by

$$\frac{\partial f}{\partial t} = f\,(\mathbf{K}:\mathbf{S}) - \frac{f\ -1}{\tau_d}(1-w_d^2) - \frac{\left(f^5-1\right)}{5\tau_d}w_d^2 \qquad (4)$$

w_d is the dynamically diluted polymer fraction

$$w_d = (G_d / G_D)^{1/2} \qquad (5)$$

with G_D being the dilution modulus of the HMMSF model[1,4]. In fast elongational flow and large values of $Wi_d = \dot{\varepsilon}\tau_d$, the elongational stress is obtained from Eq. (3) as

$$\sigma_E(Wi_d) \cong 5 f^2(Wi_d) G_d \qquad (6)$$

At large Hencky strain, the square of the steady-state stretch $f^2(Wi_d)$ is obtained from Eq. (4) as

$$f^2(Wi_d) \cong \sqrt{5Wi_d} / w_d \qquad (7)$$

From Eq. (6), the elongational viscosity is then given by

$$\eta_E(Wi_d) = \frac{\sigma_E(Wi_d)}{\dot{\varepsilon}} = \frac{\sigma_E(Wi_d)\tau_d}{Wi_d} \qquad (8)$$

Normalized by the zero-shear viscosity η_0, this results in

$$\frac{\eta_E(Wi_d)}{\eta_0} \cong 5 f^2(Wi_d) \frac{G_d\tau_d/\eta_0}{Wi_d} = \frac{5}{w_d}\sqrt{5Wi_d}\,\frac{G_d J_s^0}{Wi_d} \qquad (9)$$

From the right-hand side of this equation, we see that $\eta_E(Wi_d)$ decreases with increasing Wi_d according to $\eta_E(Wi_d) \propto Wi_d^{-1/2}$, and we note that this relation is often observed experimentally. The strain hardening index **SHI** is now defined as the normalized elongational viscosity $\eta_E(Wi_d)/\eta_0$ at $Wi_d = 1$,

$$\mathrm{SHI} = 5 f_d^2 G_d J_s^0 \qquad (10)$$

with

$$f_d^2 = f^2(Wi_d = 1) = \sqrt{5}/w_d = \sqrt{5G_D/G_d} \qquad (11)$$

While the term $5G_d J_s^0$ in Eq. (10) is determined by the LVE characterization of the melt, the representative stretch f_d depends on dynamic dilution according to Eq. (5). We also note that for pom-poms with q_a>5, the dilution modulus G_D is equal to the plateau modulus G_N^0 (**Table 3**), and therefore for these polymer systems, the SHI is fully determined by the LVE characterization[4].

COMPARISON TO EXPERIEMTAL DATA

For the 12 model PS pom-pom melts of **Table 1**, the normalized elongational viscosity $\eta_{E,\max}/\eta_0$ as a function of Weissenberg number $Wi_d = \dot{\varepsilon}\tau_d$ is shown in **Fig. 2**. Limited strain hardening is observed for pom-poms having only a few side arms at the two branched points such as 220k-2x3-70k (SHI_m=6) and 100k-2x5-25k (SHI_m=10), irrespective of the length of the side arms. We call SHI_m the experimentally observed or measured SHI. In contrast, pom-

pom 300k-2x24-40k with many side arms and the largest value of J_s^0 shows the highest strain hardening potential with SHI_m=90. Most of the other pom-poms fall in a narrow band with $SHF_m \approx 30$. Surprisingly, there is only a minor increase of SHF_m with increasing backbone molecular weight $M_{w,b}$ from 100 to 400 kg/mol, but with similar numbers of arms (q_a=10-13) and the same side arm molecular weight of $M_{w,a}$ = 40 kg/mol. Increasing the molecular weight of the side arms from 24 to 40 kg/mol at constant molecular weight of $M_{w,b}$ = 100 kg/mol and q_a=12 does not change strain hardening significantly, but a further increase of $M_{w,a}$ to 50 kg/mol increases SHF_m to 47 (**Table 3**). We note that for $M_{w,a}$ =50 kg/mol, the combined molecular weight $2M_{w,a}$ of two side arms is equal to the backbone molecular weight of $M_{w,b}$=100 kg/mol with the consequence that the entanglements of the arms act in a similar way as the entanglements of the backbone, thereby broadening the relaxation time spectrum and thus increasing the value of the steady-state compliance J_s^0 significantly. As seen from **Table 3**, $5G_d J_s^0$ is of the order 1 for all pom-poms considered and there is general agreement of the observed SHI_m and the strain hardening index SHI calculated from Eq.(10).

Table 3. Weight fraction φ_b of backbone, plateau modulus $\boldsymbol{G_N^0}$, dilution modulus $\boldsymbol{G_D}$, relaxation modulus $\boldsymbol{G_d}$, zero-shear viscosity η_0, disengagement time τ_d, steady-state compliance J_s^0, diluted polymer fraction $\boldsymbol{w_d}$, square of representative stretch f_d^2, strain hardening index SHI (Eq. (10)), and observed strain hardening index SHI_m (**Fig. 2**) for PS pom-poms at T = 160 °C.

Pom-Pom	φ_b [-]	G_N^0 [kPa]	G_D [kPa]	G_d [kPa]	η_0 [kPa s]	τ_d [s]	J_s^0 [kPa^{-1}]	$5G_d J_s^0$ [-]	w_d [-]	f_d^2 [-]	SHI [-]	SHI_m [-]
100k-2x12-24k	0.15	270	270	1.75	26	3.18	0.12	1.05	$8.0 \cdot 10^{-2}$	27.8	29.3	30
100k-2x12-40k	0.09	190	190	1.45	56	7.67	0.14	1.00	$8.7 \cdot 10^{-2}$	25.6	25.5	27
100k-2x14-50k	0.07	110	110	0.21	220	201	0.90	0.93	$4.4 \cdot 10^{-2}$	51.4	48.0	47
100k-2x22-25k	0.09	310	310	1.54	17	2.29	0.14	1.05	$7.0 \cdot 10^{-2}$	31.7	33.2	33
220k-2x9-25k	0.33	260	260	1.05	$1.5 \cdot 10^3$	313	0.21	1.11	$6.4 \cdot 10^{-2}$	35.1	39.1	35
220k-2x10-40k	0.22	190	190	1.46	$3.5 \cdot 10^3$	679	0.19	1.42	$8.8 \cdot 10^{-2}$	25.5	36.2	31
280k-2x22-22k	0.22	290	290	0.39	830	308	0.37	0.71	$3.6 \cdot 10^{-2}$	61.3	43.7	41
400k-2x9-23k	0.49	170	170	3.60	$1.9 \cdot 10^4$	1406	0.07	1.32	$1.5 \cdot 10^{-1}$	15.4	20.3	19
400k-2x13-40k	0.28	190	190	1.16	$3.5 \cdot 10^4$	7512	0.21	1.22	$7.8 \cdot 10^{-2}$	28.7	35.1	34
300k-2x24-40k	0.14	150	150	0.039	$1.0 \cdot 10^3$ *)	3441 *)	3.35	0.64	$1.6 \cdot 10^{-2}$	140	90.1	90
100k-2x5-25k	0.29	180	40	3.67	330 *)	20.8 *)	0.06	1.15	$3.0 \cdot 10^{-1}$	7.38	8.46	10
220k-2x3-70k	0.34	190	3	0.99	$3.0 \cdot 10^5$ *)	70945 *)	0.23	1.32	$5.7 \cdot 10^{-1}$	3.40	4.50	6

*) T=140°C

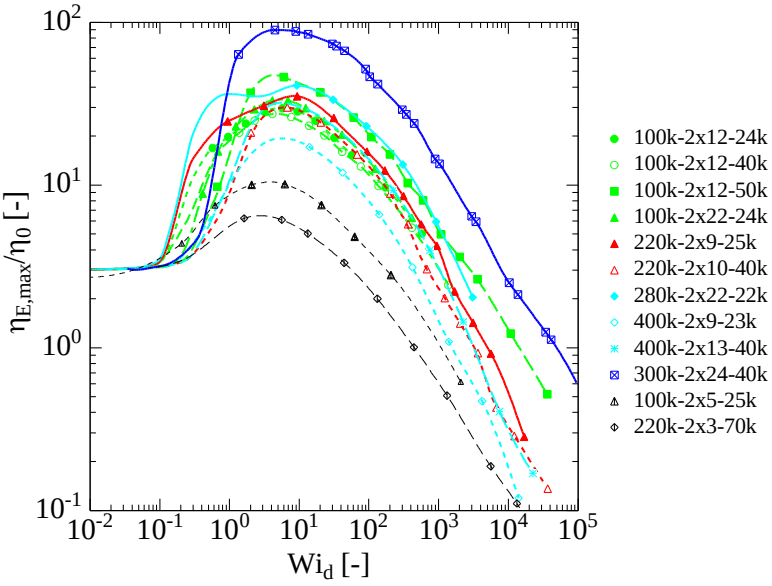

Fig. 2. Normalized maximal elongational viscosity $\eta_{E,\max}/\eta_0$ as a function of Weissenberg number $Wi_d = \dot{\varepsilon}\tau_d$ for PS model pom-poms $M_{w,b}$-2xq_a-$M_{w,a}$. Lines are calculated by the HMMSF model. Symbols indicate the calculated values at the experimental strain rates.

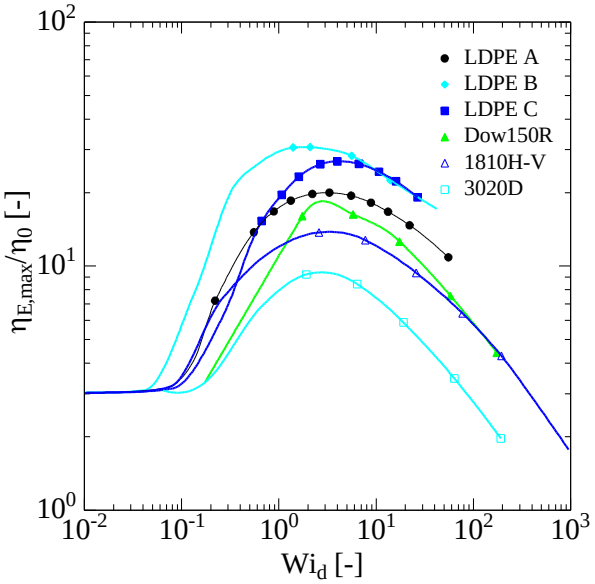

Fig. 3. Normalized maximal elongational viscosity $\eta_{E,\max}/\eta_0$ as a function of Weissenberg number $Wi_d = \dot{\varepsilon}\tau_d$ for six LDPE melts. Lines are calculated by the HMMSF model. Symbols indicate the calculated values at the experimental strain rates.

The normalized elongational viscosity $\eta_{E,\max}/\eta_0$ as a function of Weissenberg number $Wi_d = \dot{\varepsilon}\tau_d$ for the 6 LDPE melts of **Table 2** and measured at temperatures between 130 and 160 °C is presented in **Fig. 3**. Except for LDPE B, the LDPE melts show elongational stress

overshoot in start-up elongational flow. The maximal elongational viscosity $\eta_{E,\max}/\eta_0(Wi_d)$ is therefore taken as the maximum of $\eta_E^+(t,Wi_d)$. LDPE B with the highest polydispersity shows the highest strain hardening with a peak of SHI_m=30 at $Wi_d \approx 2$, while 3020D with the highest room temperature density of $\rho_{RT} = 0.94 g/cm^3$ and therefore the smallest amount of branching has the lowest strain hardening index of SHI_m=9 at $Wi_d \approx 3$ (**Table 4**). As shown in **Fig. 4**, the maximal elongational viscosity $\eta_{E,\max}/\eta_{0d}(Wi_d)$ of LDPE C is similar to that of two PS model pom-poms with $M_{w,b}$ =100 kg/mol, q_a=12, and $M_{w,a}$=24 and 40 kg/mol.

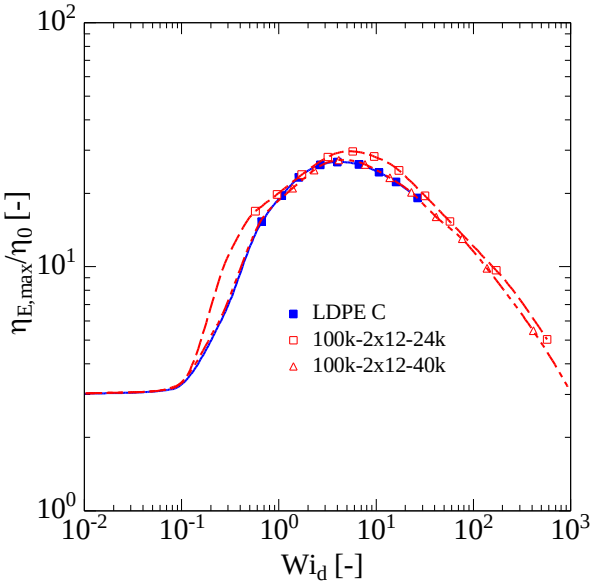

Fig. 4 Comparison of normalized maximal elongational viscosity $\eta_{E,\max}/\eta_{0d}(Wi_d)$ of LDPE C and PS model pom-poms with $M_{w,b}$ =100 kg/mol, q_a=12, and $M_{w,a}$=24 and 40 kg/mol.

Table 4. Dilution modulus G_D, relaxation modulus G_d, zero-shear viscosity η_0, disengagement time τ_d, steady-state compliance J_e^0, diluted fraction w_d, square of representative stretch f_d^2, strain hardening index SHI (Eq. (10)), and observed strain hardening index SHI_m for LDPE melts at measurement temperatures T.

LDPE	G_D [kPa]	G_d [kPa]	T [°C]	η_0 [kPas]	τ_d [s]	J_e^0 [kPa^{-1}]	$5G_dJ_e^0$ [-]	w_d [-]	f_d^2 [-]	SHI [-]	SHI_m [-]
LDPD A	30	0.170	150	31.4	22.1	0.70	0.61	$7.5\cdot10^{-2}$	29.7	17.8	20
LDPE B	30	0.049	150	7.07	14.0	1.98	0.49	$4.0\cdot10^{-2}$	55.3	26.9	30
LDPE C	30	0.012	150	22.0	26.7	1.22	0.71	$6.2\cdot10^{-2}$	35.9	25.4	27
Dow 150R	10	0.084	160	379	581	1.53	0.64	$9.1\cdot10^{-2}$	24.4	15.7	18
1810H-V	10	0.018	150	36.2	25.9	0.72	0.65	0.13	16.7	10.8	14
3020D	5	0.239	130	978	637	0.65	0.78	0.22	10.2	7.95	9

DISCUSSION AND CONCLUSIONS

We have quantified the strain hardening potential of PS pom-poms and LDPE melts by considering the maximal value of the normalized elongational viscosity $\eta_{E,\max}(Wi_d)/\eta_0$ corresponding to the normalized steady-state elongational viscosity or the normalized maximal elongational viscosity reached in the case of fracture or tensile stress overshoot, as a function of Weissenberg number $Wi_d = \dot{\varepsilon}\tau_d$. We found that $\eta_{E,\max}(Wi_d)/\eta_0$ reaches a maximal value at $Wi_d \approx 2-8$, and we showed that this experimentally observed maximal value of $\eta_{E,\max}/\eta_0$=SHI$_m$ can be used to assess the strain hardening behaviour investigated at different temperatures and across polymer systems with different topologies and different chemistries.

From a one-mode HMMSF model, we derived a relation for the strain hardening index $\mathrm{SHI} = 5 f_d^2 G_d J_s^0$ (Eq. (10)), which shows the same tendency as the measured SHI$_m$, and is in nearly quantitative agreement with SHI$_m$ up to SHI≈100. Interestingly, the temperature independent LVE factor $5G_d J_s^0$ with $G_d = G(t=\tau_d)$ is of the order of 1 for both polymer systems considered. The square of the characteristic stretch $f_d^2 = \sqrt{5}/w_d$ (Eq. (11)) depends on hierarchical relaxation and dynamic dilution with the diluted polymer fraction $w_d = (G_d/G_D)^{1/2}$ (Eq. (5)). Polymers with a large value of the steady-state compliance J_s^0, i.e., a rather broad relaxation time spectrum and therefore a low value of G_d and a small polymer fraction w_d, show large values of the strain hardening index SHI. From the comparison of pom-poms and LDPE melts considered here, we may conclude that the strain hardening potential of a typical LDPE such as LDPE C is equivalent to that of a pom-pom consisting of a backbone (largely independent of its length) and $2q_a$=24 side arms with a length corresponding to 2 to 3 times the entanglement length. Further research is in progress to extent these findings to polymer combs and to other chemistries.

REFERENCES

1. Wagner H.M.; Hirschberg V. Experimental validation of the hierarchical multi-mode molecular stress function model in elongational flow of long-chain branched polymer melts. *J. Non-Newtonian Fluid Mech.* ***2023,*** *321:105130.*
2. Hirschberg V.; Schusmann M.G.; Ropert M.C.; Wilhelm M.; Wagner M.H. Modeling elongational viscosity and brittle fracture of 10 polystyrene Pom-Poms by the hierarchical molecular stress function model. *Rheologica Acta* ***2023*** *62:269–283.*
3. Hirschberg V.; Schusmann M.G.; Ropert M.C.; Goeke A.; Wilhelm M.; Wagner M.H. Elongational rheology of 2, 3 and 4 polymer stars connected by linear backbone chains. *Rheologica Acta* ***2024*** *63:407-423.*
4. Wagner M.H.; Narimissa E.; Poh L.; Huang Q. Modelling elongational viscosity overshoot and brittle fracture of low-density polyethylene melts. *Rheologica Acta* ***2022*** *61: 281–298.*

Biopolymer Rheology

RHEOLOGICAL BEHAVIOR OF AQUEOUS SUSPENSIONS OF HIGHLY-REFINED PULP FIBRES

Antti Koponen[1], Juan Cecchini[2], Marjo Järvinen[1] and Olli-Ville Laukkanen[1]

[1]VTT Technical Research Centre of Finland Ltd, Koivurannantie 1, 40400 Jyväskylä
[2]Valmet Technologies, Inc., Rautpohjankatu 3, 40700 Jyväskylä, Finland

ABSTRACT

This study focuses on the rheological properties of highly-refined pulp fibres (HRF) as a potential alternative to energy-intensive microfibrillated and nanofibrillated celluloses (MFC/NFC). HRF, produced via conventional refining, has a broad size distribution but may offer similar functional benefits. We performed a detailed rheological analysis of HRF suspensions at four refining levels and five solids contents (1.2–3.0 wt%), using amplitude and frequency sweep measurements to assess viscoelastic properties, and steady-state viscosity measurements to examine flow behaviour.

INTRODUCTION

Microfibrillated and nanofibrillated celluloses (MFC and NFC) have been researched as additives in papermaking e.g. for improved barrier, strength, surface, and optical properties. The production of MFC and NFC through mechanical fibrillation of pulp fibres requires a significant amount of energy. Therefore, producing fibrous materials containing MFC through extensive refining with a conventional refiner can be a more efficient alternative. This approach has the advantage that it is well-established and readily available on an industrial scale. However, unlike MFC suspensions, this material has a very broad size distribution, as it consists of a mixture of fibrillated fibres and fine particles that form simultaneously during refining. These highly refined pulp fibres (HRF) could replace MFC in a variety of applications. Another promising strategy is to use them directly for novel cellulose-based applications. However, there is currently little information available on the rheological behaviour of the aqueous suspensions of these materials.

In this work, we performed a comprehensive rheological analysis for suspensions of highly-refined fibres at four refining levels and five solids contents ranging from 1.2 to 3.0 wt%. Our rheological characterization included amplitude and frequency sweep measurements to analyze the viscoelastic behaviour of these materials, as well as steady-state viscosity measurements to study the flow behaviour of these materials at various shear rates.

MATERIALS AND METHODS

Fibres

Eucalyptus Bleached Hardwood Kraft Pulp (BHKP) suspension was refined at Valmet Technologies to four specific refining energy (SEC) levels: 600 kWh/t, 760 kWh/t, 1400 kWh/t

and 2140 kWh/t. We call these fibre suspensions with an increasing refining level HRF, XFC(a), XFC(b) and MFC. **Fig. 1a** shows the average fibre length and width, and **Fig. 1b** shows the content of A- and B-type fines (flake- and fibril-type elements, respectively) as the function of the specific refining energy for these materials. The solids properties of the fibre suspension were measured using the FS5 Fiber Analyzer (Valmet Automation, Kajaani, Finland). The FS5 measures the fractions optically so that fines A is calculated as a percentage of the projection area of particles, and fines B is calculated as a percentage of particle length. Thus, the values are not directly comparable and do not add up to 100%. For HRF, XFC(a), and XFC(b), the mass concentrations (w/w) used in the measurements were 1.2%, 1.8%, 2.1%, 2.4%, and 3.0%. For MFC, measurements were performed at a single concentration of 2.1%. All suspensions were prepared using tap water with a salinity of 20–50 mg/L.

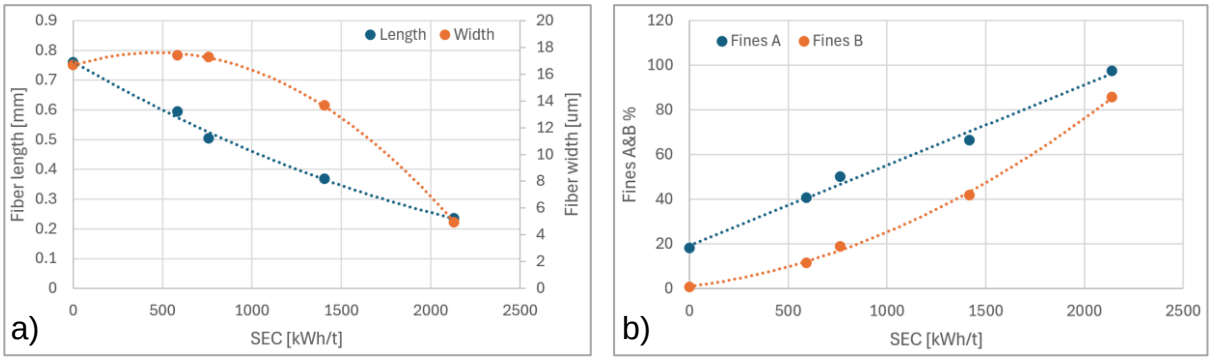

FIGURE 1: a) The fibre length and width as a function of specific refining energy. b) The mass content of A- and B-type fines (flake- and fibril-type elements, respectively) as a function of specific refining energy. Solid lines are included as a guide for the eye.

Rheological measurements

The rheological measurements were performed using a stress-controlled TA Instruments DHR-2 rheometer (**Fig. 2a**) using a wide-gap vane-in-cup geometry (**Fig. 2b**). The cup with a serrated surface was 3D-printed to eliminate wall slip. The diameter of the four-blade vane was 15 mm, and the inner diameter of the transparent cup was 30 mm, resulting in an effective measurement gap of 7.5 mm. The vane geometry was positioned vertically in the middle of the cup – the lower edge of the vane located 16 mm above the bottom of the cup, and the upper edge of the vane located 16 mm below the upper surface of the sample – to avoid end effects. The use of such a wide-gap vane geometry further minimizes possible wall slip effects[1] and avoids confinement effects that would be caused by the large size of the flocs compared to the measurement gap[2]. Notice that the small-gap approximation, typically applicable for standard rheometer geometries like concentric cylinders or cone-and-plate setups, does not hold for the vane-in-cup geometry. Therefore, the shear rate varies radially within the sample[3], and it is more accurate to refer to the shear rate as an apparent shear rate.

The rheological characterization included amplitude sweep measurements (γ_0 = 0.01 - 1000 %, ω = 1 rad/s) and frequency sweep measurements (ω = 0.1 - 100 rad/s, γ_0 = 0.1 %) to analyze the viscoelastic behaviour of these materials, as well as steady-state viscosity measurements to study the flow behaviour of these materials at various shear rates (first increasing the apparent shear rate from 0.001 to 100 s^{-1} and then decreasing it from 100 to 0.001 s^{-1}). All rheological measurements were performed at 22 °C.

FIGURE 2: a) Stress-controlled TA Instruments DHR-2 rheometer.
b) The vane geometry and the 3D-printed serrated cup used in this study.
c) The measurement setup.

RESULTS

Steady-state viscosity measurements

Table 1 presents the viscosity values (obtained from the downward sweep) of the different materials at a shear rate of 1.0 s^{-1}. We see that as expected, viscosity increases with increasing fiber concentration and refining energy. The only exception is 2.1% MFC which has a slightly lower viscosity than 2.1% XFC(b). Overall, at a given concentration, the viscosities do not vary significantly. The difference between the lowest and highest viscosity is less than a factor of two. It is somewhat surprising that the viscosities of refined cellulose fibre suspensions remain relatively unchanged, even as the refining energy increases significantly. **Fig. 3** compares the measured viscosities at different concentrations with the viscosities of various MFC grades[4] and highly refined softwood fibres[5] reported in the literature.

TABLE 1 Viscosity (Pa·s) at a shear rate of 1.0 s^{-1} for different materials and concentrations.

%	HRF	XFC(a)	XFC(b)	MFC
1.2	6.5	7.6	10.4	-
1.8	18.6	19.8	31.6	-
2.1	26.1	36.5	48.2	44.2
2.4	35.8	49	63.1	-
3	71.7	82.4	107.8	-

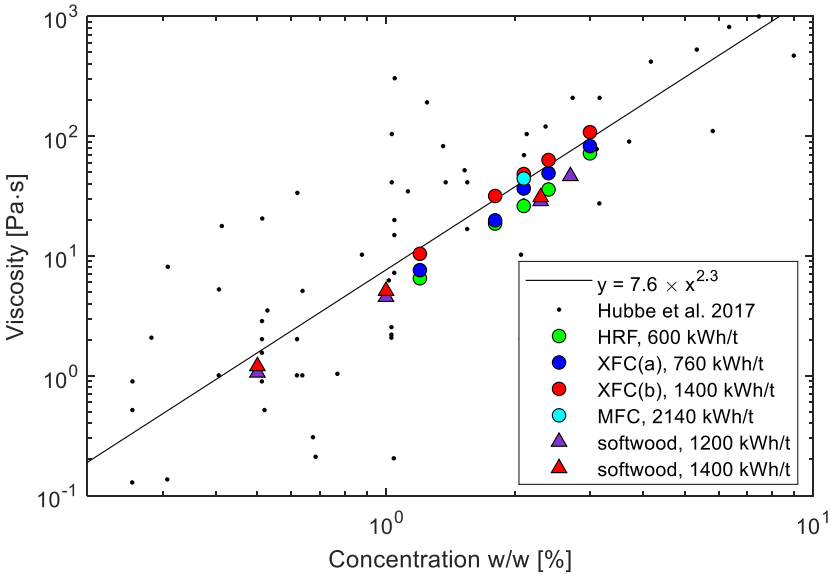

FIGURE 3: Viscosity at a shear rate of 1.0 s^{-1} as a function of concentration for the different materials. Values from a data set for various types of MFC and NFC [4] and highly refined softwood fibres[5] are shown for comparison. The solid line represents a power law fit to the data set from Hubbe et al 2017.

We see from **Fig. 3** that the viscosities of the materials studied here are comparable to the average behaviour of MFCs (see the solid line), with their concentration dependence approximately following a universal[6] power-law relationship. We studied the dependence of the viscosity on the concentration by fitting the power law

$$\eta = Ac^{\alpha} \tag{1}$$

to the data shown in **Table 1**. The values of the fitting parameters, A and α, are shown in **Table 2**. We see that the exponent α is ca. 2.6 for all three materials. This falls well within the range reported in the literature; it is only slightly higher than in the dataset compiled by Hubbe et al.[4]

TABLE 2 Fitting parameter values from Eq. (1) for the different materials. In all cases, R^2 was greater than 0.98.

	HRF	XFC(a)	XFC(b)
A [Pa·s]	4.00	4.62	6.79
α	2.57	2.66	2.56

Fig. 4 shows shear stress as a function of shear rate, while **Fig. 5** presents viscosity versus shear rate for fibre concentrations of 1.2%, 2.1%, and 3.0%, across the different materials measured both at increasing and decreasing shear rate. The curves are noisier with the two lower refining levels. This is due to the higher inhomogeneity of HRF and XFC(a) when compared to XFC(b) and MFC. With a given shear rate, shear stress and viscosity increase in most cases with increasing refining levels. An exception is 2.1% XFC(b), which exhibits slightly higher stress/viscosity than 2.1% MFC. This could be due to a minor deviation in suspension concentration. However, this difference could also arise from XFB(b) having an optimal combination of short and long fibres that enhances momentum transfer across the material. At the smallest shear rates of an upward sweep, stress initially increases rapidly and then decreases as the shear rate increases. This behaviour occurs because the measurement was started without pre-shearing, resulting in a non-homogeneous structure where the fibres are more flocculated.

Moreover, the data measured at increasing shear rates may be affected by shear banding, particularly at low to intermediate shear rates[7].

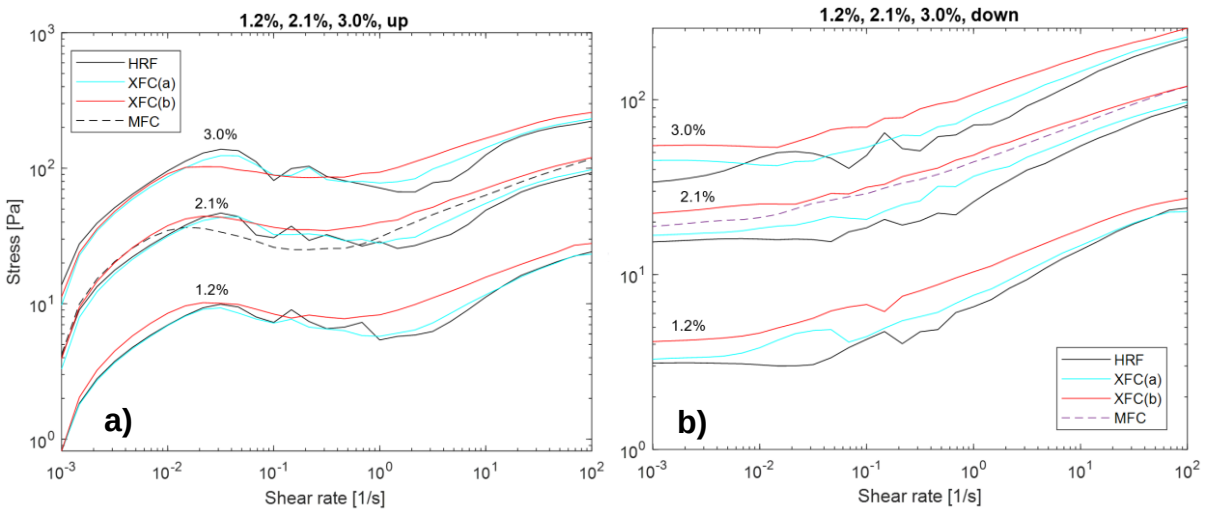

FIGURE 4: Shear stress as a function of shear rate for consistencies 1.2%, 2.1% and 3.0% for the different materials. a) Increasing shear rate. b) Decreasing shear rate.

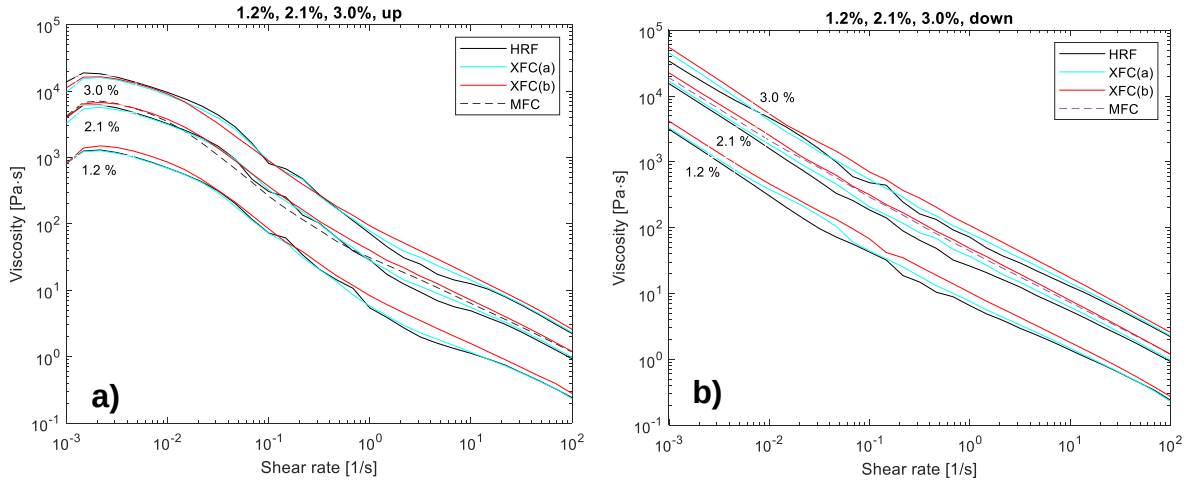

FIGURE 5: Viscosity as a function of shear rate for fibre concentrations 1.2%, 2.1% and 3.0% for the different materials. a) Increasing shear rate. b) Decreasing shear rate.

The stress vs. shear rate curves of the downward sweeps resemble that of a typical Herschel-Bulkley fluid behaviour, namely

$$\sigma = \sigma_0 + K\dot{\gamma}^n \,, \tag{2}$$

where σ is the shear stress, σ_0 the yield stress, K is the consistency index, and n is the flow index. The materials thus exhibit yield stress, and their viscous behaviour approximately follows a power law at high shear rates. We fitted Eq. (2) to the shear stress vs. shear rate curves; an example of a fit is shown in **Fig. 6**. The fitting parameters are provided in **Table 3**. The values of the flow indexes are typical for MFC-type materials at these mass concentrations[6]. Yield stress was similar for all materials with a given concentration. Notice that generally, the measured curves were flat at low shear rates, while the Herschel-Bulkley model fits slightly underestimated the yield stress, as also shown in **Fig. 6.**

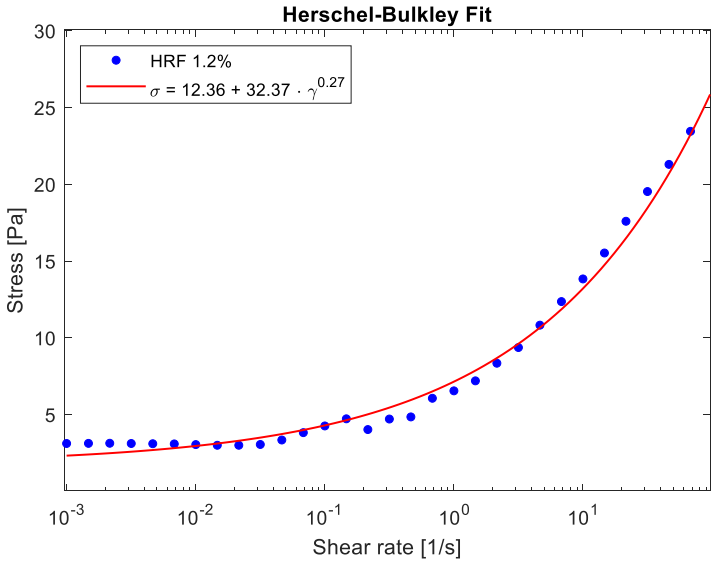

FIGURE 6: Herschel–Bulkley fit, Eq. (2), to the 1.2% HRF flow sweep data with decreasing shear rate.

We studied the dependence of the yield stress on the concentration by fitting the power law

$$\sigma_0 = Bc^{\beta} \tag{3}$$

to the yield stress data shown in **Table 3**. The obtained values for the fitting parameters are shown in **Table 4**. In all cases, the value of parameter β was close to three, which is somewhat higher than typically found in the literature. In the review of Koponen[6], e.g., the mean value of β for various MFC types of materials was 2.3.

TABLE 3: Fitting parameter values from Eq. (2) for the different materials and concentrations. The parameters are consistency index *K*, flow index *n*, and yield stress σ_0. R^2 was always greater than 0.97.

		HRF		XFC(a)			XFC(b)			MFC		
[%]	K [Pa s^n]	n [-]	σ_0 [Pa]	K [Pa s^n]	n [-]	σ_0 [Pa]	K [Pa s^n]	n [-]	σ_0 [Pa]	K [Pa s^n]	n [-]	σ_0 [Pa]
1.2	5.4	0.33	1.8	6.3	0.28	1.9	9.1	0.24	1.7	-	-	-
1.8	12.5	0.34	6.7	14.6	0.32	7.2	23.7	0.25	8.6	-	-	-
2.1	18.5	0.34	11.1	26.6	0.27	10.2	36.3	0.24	13.0	32.4	0.27	12.4
2.4	22.7	0.35	17.4	36.2	0.27	15.0	49.3	0.22	15.5	-	-	-
3.0	43.4	0.33	31.2	57.7	0.28	28.2	80.8	0.23	29.5	-	-	-

TABLE 4 Fitting parameter values from Eq. (3) for the different materials. In all cases, R^2 was greater than 0.98.

	HRF	XFC(a)	XFC(b)
B [Pa]	1.03	1.19	1.14
β	3.17	2.91	3.07

Amplitude sweep measurements

Figs. 7 and **8** show the storage modulus and the loss modulus as functions of strain amplitude, respectively. The shapes of the curves are typical for MFC-type materials[8]. In the linear

viscoelastic regime (strain amplitude < 1%), G' generally increases with increasing refining levels. An exception is 3.0% HRF which has higher G' and G'' than XFC(a) in this regime. With strain amplitude > 10% this anomaly vanishes. To check whether this was due to slight variations in concentration, we repeated the measurements and obtained the same result. Then, by gradually decreasing the concentration, we found that at concentrations below 2.7%, XFC(a) exhibited higher G′ and G″ values than HRF. At present, we do not have an explanation for this behaviour.

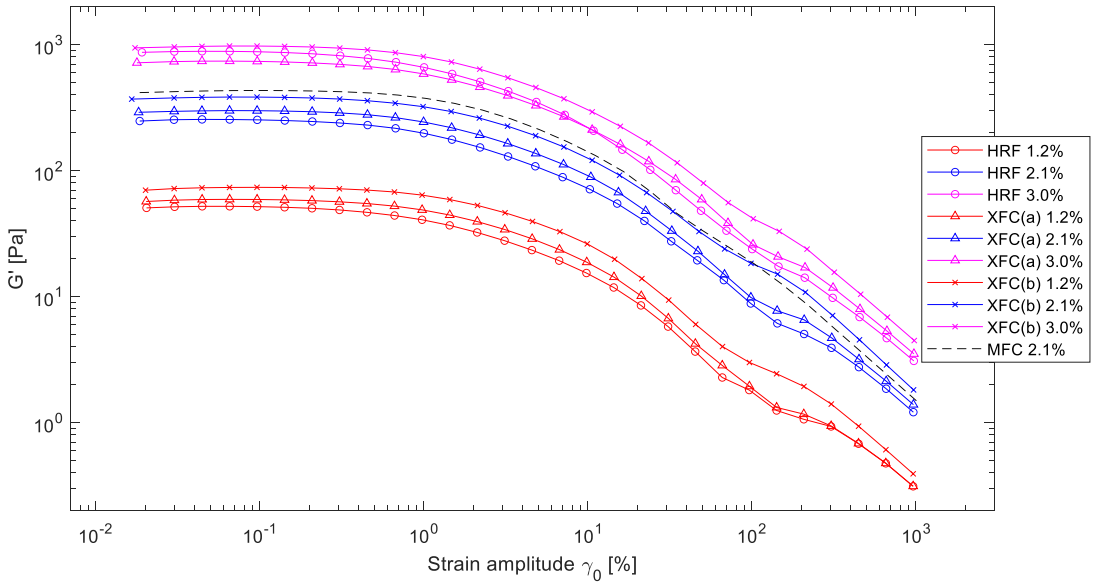

FIGURE 7: Storage modulus G' as a function of strain amplitude for the different materials and concentrations of 1.2%, 2.1% and 3.0%.

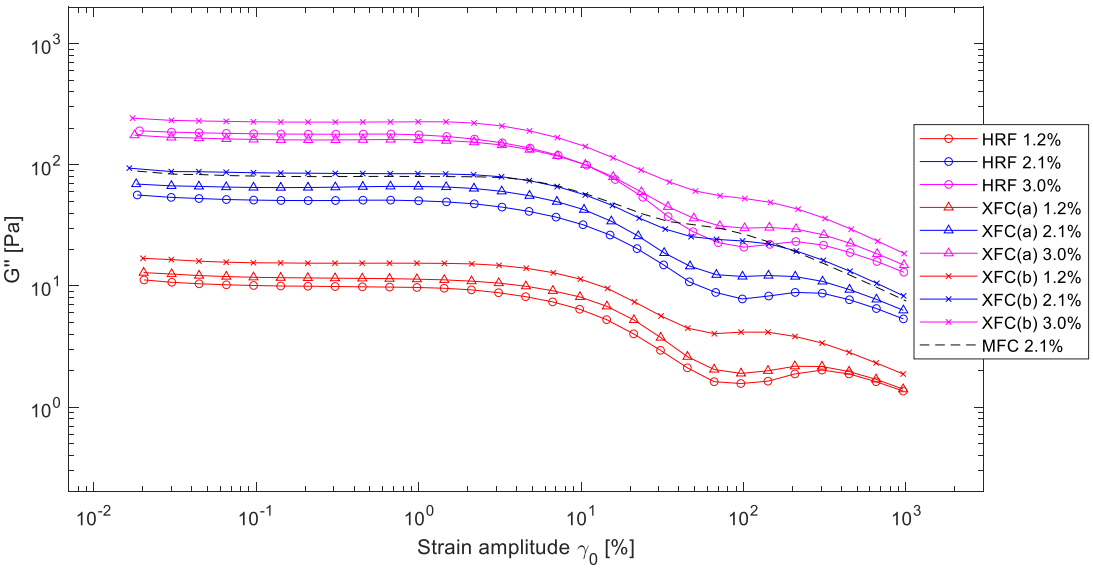

FIGURE 8: Loss modulus G'' as a function of strain amplitude for the different materials and concentrations 1.2%, 2.1% and 3.0%.

We determined the values of the storage and loss modulus in the linear viscoelastic (LVE) region. The LVE region was defined as the strain range over which G′ and G'' remained approximately constant, indicating undisturbed material structure. The onset of nonlinearity was identified as the point where G′ or G'' deviated by more than 5% from its initial plateau value. The storage and loss moduli, representative of the LVE region, were calculated as the averages of G′ and G″ within this linear range. **Table 5** shows these values for different materials and concentrations. In **Fig. 9**, G' and G'' are presented as a function of concentration. We see from **Fig. 9** that the relation between G' and G'' and concentration is a power law

$$G' \text{or } G'' = Dc^{\delta} \ . \tag{4}$$

The fits of Eq. (4) to the data are shown in **Fig. 9** with solid lines. The fitting parameters are shown in **Table 6**. The value δ is close to three in all cases. Similar values can be found in the literature for both MFC and NFC [9-12].

TABLE 5: The storage modulus G' and loss modulus G'' in the LVE region for the different materials and concentrations.

	HRF		XFC(a)		XFC(b)		MFC	
[%]	G' [Pa]	G'' [Pa]	G' [Pa]	G'' [Pa]	G' [Pa]	G'' [Pa]	G' [Pa]	G'' [Pa]
1.2	50.5	10.3	57.2	11.9	71.7	15.8	-	-
1.8	159.4	33.6	183.1	39.4	234.5	55.3	-	-
2.1	247.0	52.1	292.5	66.0	371.8	86.6	421.6	81.7
2.4	387.2	88.4	434.0	100.2	531.1	126.1	-	-
3.0	853.5	181.9	718.1	164.0	943.0	228.3	-	-

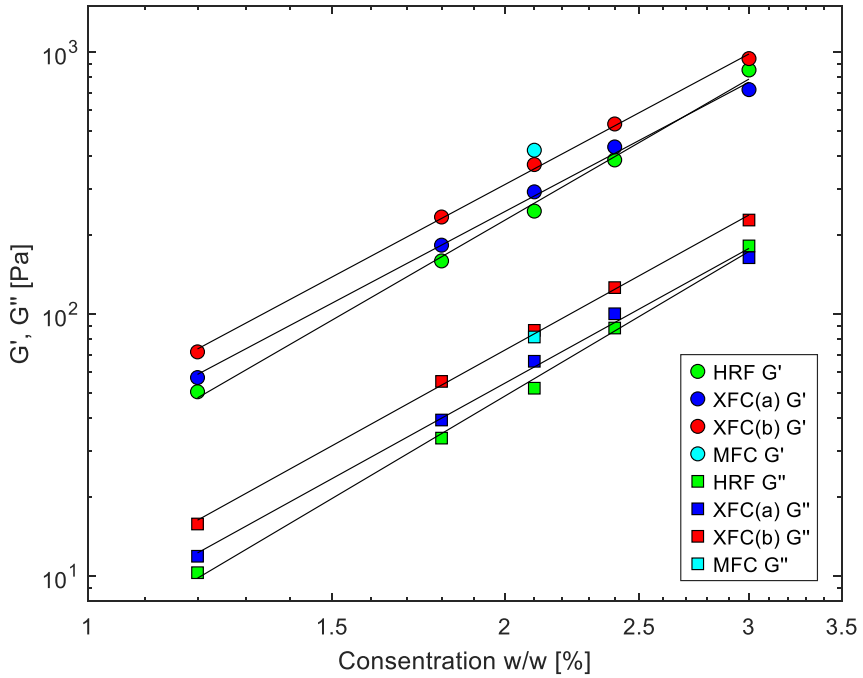

FIGURE 9: Storage modulus and loss modulus in the LVE region as a function of concentration. Solid lines represent power-law fits for each material (excluding MFC).

TABLE 6: Fitting parameter values from Eq. (4) for the different materials.

	HRF G'	HRF G''	XFC(a) G'	XFC(a) G''	XFC(b) G'	XFC(b) G''
D	27.4	5.52	35.3	7.21	43.9	9.58
δ	3.05	3.14	2.80	2.92	2.83	2.93

Frequency sweep measurements

Figs. 10 and **11** show the storage modulus and the loss modulus as functions of angular frequency. All samples can be observed to exhibit strongly elastic behaviour irrespective of the fiber type and concentration, with weak frequency dependence of G' and G''. This is typical behaviour for MFC-type materials[10-12].

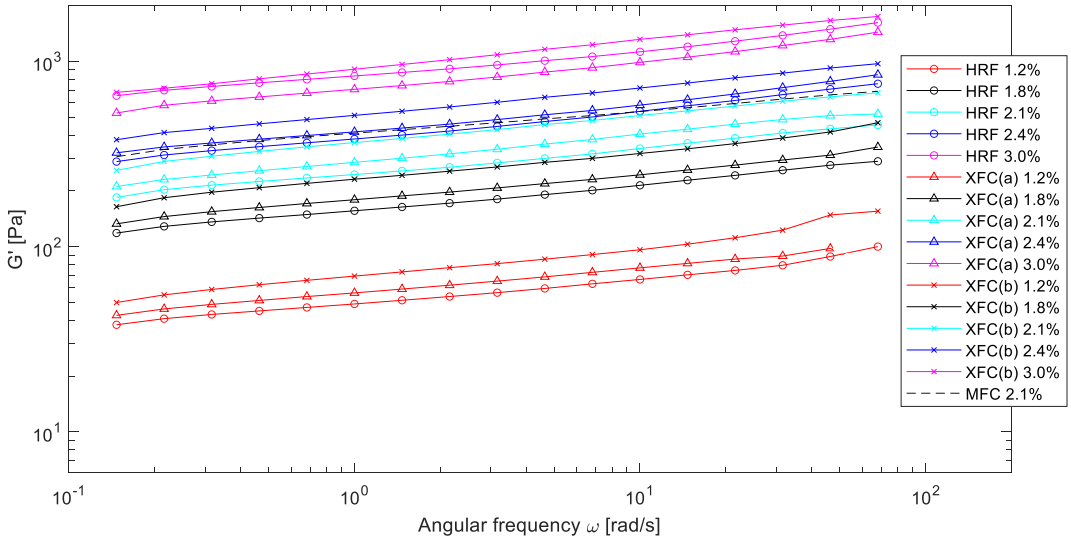

FIGURE 10: Storage modulus G'' as a function of angular frequency for the different materials and concentrations.

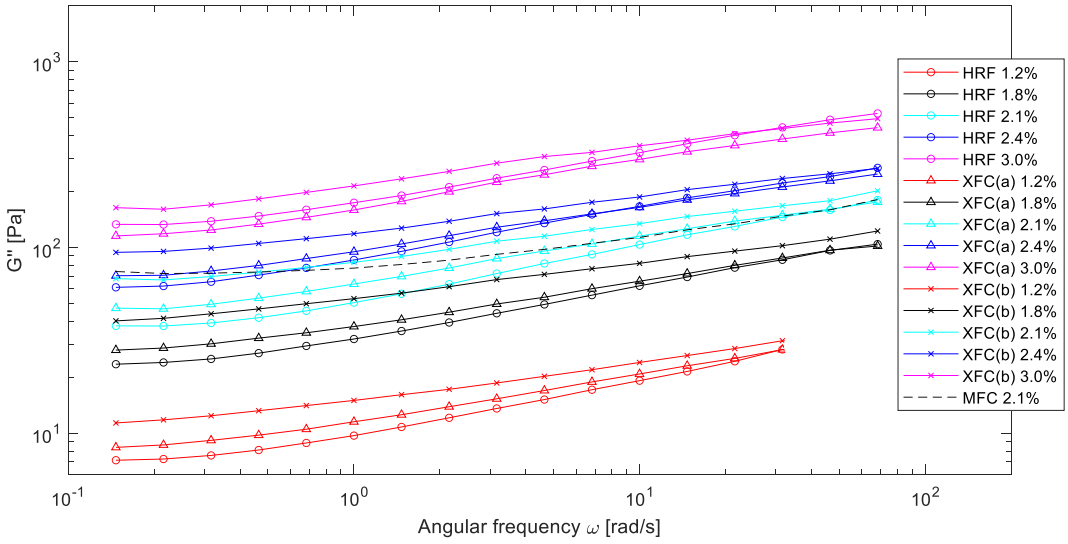

FIGURE 11: Loss modulus G'' as a function of angular frequency for the different materials and concentrations.

SUMMARY

This study provided a comprehensive rheological analysis of highly refined fibres (HRF) as a potential alternative to microfibrillated and nanofibrillated celluloses (MFC/NFC). Four HRF suspensions were studied across a mass concentration range of 1.2% to 3.0%. The results demonstrate that HRF exhibits rheological properties comparable to those of MFC/NFC, despite a broader fibre size distribution. The viscosity of HRF suspensions showed relatively small variation with increasing refining energy, while the yield stress remained nearly constant across all refining levels. The flow, amplitude, and frequency sweeps of the HRF suspensions closely resembled those observed for MFC/NFC. Overall, the findings highlight the potential of HRF as a cost-effective and energy-efficient alternative to MFC/NFC. The ability to produce HRF using conventional refining methods offers a significant advantage for industrial-scale applications, providing a more sustainable approach to enhancing cellulose-based products.

REFERENCES

1. Mohtaschemi, M., Dimic-Misic, K., Puisto, A., Korhonen, M., Maloney, T., Paltakari, J. Alava, M., Rheological characterization of fibrillated cellulose suspensions via bucket vane viscometer, *Cellulose* **2014**, 21, 1305–1312. https://doi.org/10.1007/s10570-014-0235-1.
2. Barnes, H., Nguyen, Q., Rotating vane rheometry—a review, *Journal of Non-Newtonian Fluid Mechanics* **2001**, 98(1), 1–14. https://doi.org/10.1016/S0377-0257(01)00095-7.
3. Chaparian, E., Owens, C., McKinley, G., Computational rheometry of yielding and viscoplastic flow in vane-and-cup rheometer fixtures, *Journal of Non-Newtonian Fluid Mechanics* **2022**, 307, 104857. https://doi.org/10.1016/j.jnnfm.2022.104857.
4. Hubbe, M., Tayeb, P., Joyce, M., Tyagi, P., Kehoe, M., Dimic-Misic, K., Pal, L., Rheology of nanocellulose-rich aqueous suspensions: a review, *Bioresources* **2017**, 12(4), 9556–9661. https://doi.org/10.15376/biores.12.4.Hubbe.
5. Jäsberg, A., Heiskanen, S., Cecchini, J., Kiiskinen, T., Koponen, A., Characterizing rheological behavior and fluidization of highly refined furnishes for process optimization, *TAPPI Journal* **2024**, 23(4), 200-208. https://doi.org/10.32964/TJ23.4.200.
6. Koponen, A., The effect of consistency on the shear rheology of aqueous suspensions of cellulose micro- and nanofibrils: a review, *Cellulose* **2020**, 27(4), 1879-1897. https://doi.org/10.1007/s10570-019-02908-w.
7. Nechyporchuk, O., Naceur Belgacem M., Pignon F., Rheological properties of micro-/nanofibrillated cellulose suspensions: Wall-slip and shear banding phenomena, *Carbohydrate Polymers* **2014**, 112, 432-439. https://doi.org/10.1016/j.carbpol.2014.05.092.
8. Rezayati Charani, P., Dehghani-Firouzabadi, M., E. Afra, E., Shaker, A., Rheological characterization of high concentrated MFC gel from kenaf unbleached pulp, *Cellulose* **2013**, 20, 727–740. https://doi.org/10.1007/s10570-013-9862-1.
9. Schenker, M., Schoelkopf, J., Gane, P., Mangin, P., Influence of shear rheometer measurement systems on the rheological properties of microfibrillated cellulose (MFC) suspensions, *Cellulose* **2018**, 25, 961–976. https://doi.org/10.1007/s10570-017-1642-x.
10. Rezayati Charani, P., Dehghani-Firouzabadi, M., Afra, E., Shakeri, A., Rheological characterization of high concentrated MFC gel from kenaf unbleached pulp. *Cellulose* **2013**, 20, 727–740. https://doi.org/10.1007/s10570-013-9862-1.
11. Agoda-Tandjawa, G., Durand, S., Berot, S., Blassel, C., Gaillard, C., Garnier, C., Doublier, J., Rheological characterization of microfibrillated cellulose suspensions after freezing, *Carbohydrate Polymers* **2010**, 80(3), 677-686. https://doi.org/10.1016/j.carbpol.2009.11.045.
12. Pääkkö, M., Ankerfors, M., Kosonen, H., Nykänen, A., Ahola, S., Österberg, M., Ruokolainen, J., Laine, J., Larsson, P., Ikkala, O., Lindström, T., *Biomacromolecules* **2007** 8(6), 1934-1941. https://doi.org/10.1021/bm061215p.

USE OF AI-BASED LANGUAGE MODELS

AI-based language models ChatGPT (OpenAI, San Francisco, CA, USA), and Microsoft Copilot (Microsoft Corporation, Redmond, WA, USA) were used to improve readability and refine language in the manuscript. The AI was not used for data analysis, interpretation, or scientific conclusions. The authors take full responsibility for the final content and any errors.

Engineering Rheology

EFFECT OF DISSOLUTION OF CO_2 AND CH_4 ON THE FLOW CURVE OF DRILLING FLUIDS

Blandine Feneuil[1], Elie N'Gouamba[1], Jan Ole Skogestad[1], Harald Linga[1]
[1]SINTEF, NO-7031 Trondheim, Norway

ABSTRACT

When drilling a well, careful choice of drilling fluid is essential to allow, among others, for well stabilization and lubrication of the drill bit. The apparent viscosity of a drilling fluid is one of its major properties affecting the ability to be pumped and to transport particles. However, when the drilling fluid is circulated in a well, it may meet components that affect its properties. Here we investigate the case of a gas kick, i.e., fluid from the rock formation entering the wellbore, and evaluate how the reservoir fluid dissolution affects the apparent viscosity of the fluids.

The drilling fluid-reservoir fluid mixtures are prepared at high pressure (400 bar) in a 1L piston bottle, and the apparent viscosity is measured with a high-pressure Couette cell provided by Anton Paar. Several drilling fluids are tested, and as reservoir fluids we perform experiments with CO_2, CH_4, or a mix of both. The results show that reservoir fluid dissolution decreases the apparent viscosity of the fluids at given temperature and pressure conditions.

The experimental results will be used to calibrate numerical models in order to improve a well-control evaluation software.

INTRODUCTION

When drilling a well, careful choice of drilling fluid is essential to allow, among others, for well stabilization and lubrication of the drill bit. The apparent viscosity of a drilling fluid is one of its major properties affecting the ability to be pumped and to transport particles. However, when the drilling fluid is circulated in a well, it may meet different impurities that affect its functional properties. In oil and gas wells, gas kick, i.e., penetration of natural gas (mainly CH_4) into the well during drilling, poses a major risk for well safety, and may lead in worst case to blow out. Gas kicks are usually detected and remediated with the help of well control software.

The project "Well control for CO_2 wells", started in 2022, aims to integrate the performance prediction of CO_2 kick in software for well control. Key activity in the project is the generation of experimental data to calibrate a thermodynamical model on CO_2 solubility in drilling fluids and the effects on the density and apparent viscosity. The thermodynamical model is integrated to the software. The first results of the projects have already been published [1–5], including among others the solubility of CO_2 in drilling fluids and the effect on the density and the viscosity of the fluids. The risk of CO_2-hydrate formation in drilling fluids was also assessed.

In this paper, we focus on CO_2-CH_4 gas mixtures, to see how the solubility of each fluid component in the drilling fluid is affected by the presence of the other. Then, we evaluate the effect of the dissolution of the reservoir fluids on the density and the apparent viscosity of the drilling fluids.

MATERIALS AND METHODS

Materials

We have selected three commercial drilling fluids for the tests; two water-based drilling fluids (WBDF index 1 and 2) and one oil-based drilling fluid (OBDF). The exact composition of the fluids is not known, but the main characteristics of each drilling fluid are listed in **TABLE 1**. Note that the fluids are the same as used in previous publications[1–5].

TABLE 1: Drilling fluids used in this paper

Drilling fluid	Base fluid	Density (g/L)
WBDF1_factory	NaCl Brine	1160
WBDF1_field	NaCl Brine	1150
WBDF2	KCl Brine	1280
OBDF	Base oil	1480

Three different batches of water-based drilling fluids have been used in this study, all come from the same vendor. Water-based drilling fluids are typically made from a salt solution (brine), where polymer, particles and other additives are added to control the fluid properties (viscosity, density, fluid loss…). WBDF1_Factory and WBDF1_field are the same drilling fluid, i.e. have the same composition, but the former comes directly form the factory while the latter has been circulated in a well before it was shipped to us. WBDF1_field therefore contains additional particles and impurities from the well. WBDF2 has a different composition and is based on KCl brine.

We also performed experiments with one oil-based drilling fluids (OBDF). It is composed of a base oil, approximately 80%, and contains further on brine, emulsifiers, and diverse particles.

In this study, we have dissolved CO_2 and/or CH_4 into the drilling fluids. Pressurized CO_2 and CH_4 bottles are provided by Linde with a CO_2 purity higher than 99.7%, and a CH_4 purity of 99.5%. In this paper, we use the following conventions to indicate the amount of reservoir fluids in the OBDF-gas mixtures:

- The amount of reservoir fluids (CO_2 + CH_4) is given as a weight fraction of the total mixture, i.e., drilling fluid and gas.
- When both CO_2 and CH_4 are dissolved, we indicate the molar fraction of CH_4.

Solubility measurements

The drilling fluids – gas mixtures are prepared and homogenized at high pressure (up to 400 bar) as follows:

1- The drilling fluid is placed in a 1L Leutert piston bottle (see **FIGURE 1** (a)), called “mixing cylinder”. On the hydraulic side, the piston bottle is connected to a Vindum

VP-6K pump (Pump A), allowing to monitor the pressure in the mixing cylinder and the volume variations of the hydraulic fluid.

2- The reservoir fluids CO_2 or CH_4 are transferred first as gases from the respective CO_2 or CH_4 pressurized bottles to another piston bottle, called "gas cylinder", then from the gas cylinder to the mixing cylinder. This procedure allows us to accurately control the pressure and volume of gas transferred to the mixing cylinder at ambient temperature (23°C), and therefore the mass of gas.

3- The mixing cylinder is agitated for at least one night using a rolling steel ball and an oscillating platform at high pressure to homogenise the mixture and let CO_2 and/or CH_4 dissolve into the drilling fluid.

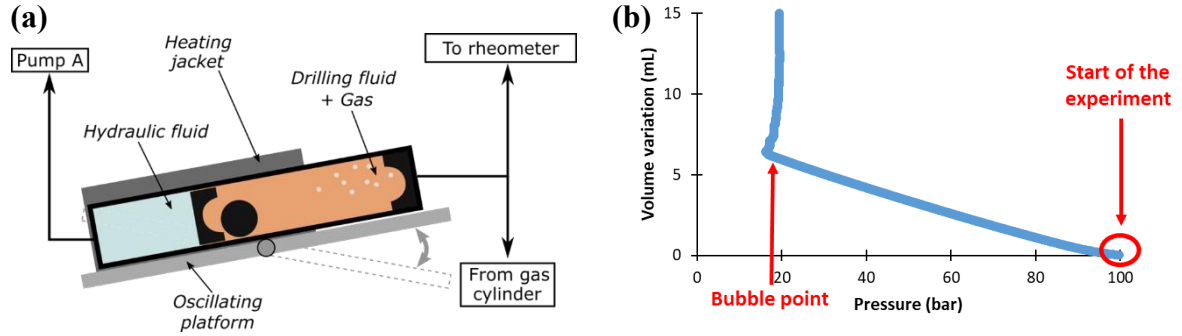

FIGURE 1: (a) Schematic of the mixing cylinder. (b) Illustration of the solubility measurement method. Drawings adapted from *Skogestad et al.*(2024)[1]

After the homogenization of the mixture, we perform solubility measurements. The hydraulic fluid is pumped out of the mixing cylinder at a constant rate (0.01 mL/min) to increase the volume of the of the drilling fluid – gas mixture, and the pressure is recorded. An example of obtained pressure-volume curve is shown in **FIGURE 1** (b): a clear change of slope appears, indicating a phase change in the mixture. The pressure when this happens is called the bubble point. The bubble point may reflect two physical phenomena:

- Release of dissolved CO_2 and/or CH_4 for the drilling fluid, i.e., apparition of gas bubbles
- Phase transition of undissolved CO_2 or CH_4, from liquid or supercritical to gas. This happens if the CO_2 or CH_4 is not fully dissolved in the drilling fluid. For CO_2 at ambient temperature, this transition occurs at 60 bar. It means for instance that if the CO_2 concentration in the fluids exceeds the maximal solubility of CO_2 (typically about 3% in water-based drilling fluids[2] and 15% in oil-based drilling[1]), we measure experimentally a bubble point at 60 bar.

The results of the solubility measurements are used to ensure that the density and rheology measurements, described in the next paragraphs, are performed only in the case where the gas is fully dissolved in the drilling fluids (gas content below the maximal solubility, pressure above the bubble point).

Density

The density of the drilling fluids - gas mixtures is assessed by analyzing the change of volume of the fluid in the mixing cylinder when gas is added, or temperature or pressure are modified. The volume of the fluid mixture is deduced from the volume variations of the hydraulic fluid, given by the pump, after correction for the compressibility of the hydraulic fluid. More details of the method can be found in Skogestad et al. (2024)[1].

We have observed that this method is accurate to determine volume variations, but not for measurement of absolute volume due to possible experimental artifacts such as bubbles in the hydraulic fluid. Therefore, in these experiments, we measure density variations from the reference density, i.e., the density of the drilling fluid at ambient temperature and without gas.

Rheology

Measurements are performed with a high-pressure cell (maximum pressure 1000 bar) from Anton Paar, placed in an Anton Paar MRC 102 rheometer. The high-pressure cell has been described in several publications[1,6,7], we will recall here the main points. The geometry is a Couette cell with a rotating cylinder of diameter 29 mm, giving a gap of 0.5 mm. To allow for high pressure inside the cell, it is closed on top, and the rotating cylinder is entrained by a magnet rotating outside the cell. Due to the high inertia of the magnet-cylinder system, the high-pressure cell has low relative accuracy at low torque values. The accuracy limit as defined by the shear stress value where system effects and repeatability are in the same range as the physical value, corresponds to about 5 Pa shear stress.

The cell has only one inlet, which is used for filling. Initially, a vacuum is made in the cell to remove air. Then, the cell is connected to the mixing cylinder; this leads to a pressure drop in the mixing cylinder. We always check that this drop does not lower the pressure below the bubble point, so that no gas bubbles are formed in the rheometer cell.

RESULTS AND DISCUSSION

Oil-based drilling fluid

Result of CO_2 solubility in the same OBDF have been published in Skogestad et al. (2024)[1], some measurements of CH_4 dissolution in two oil-based drilling fluids are presented in Torsvik et al. (2016)[6]. Here, we will focus on impact from mixtures of CO_2 and CH_4 exposed to the drilling fluids.

Solubility of CO_2 and CH_4 mixtures

Oil-based drilling fluids are mainly composed of base oil, where different components are added. This includes brine (here $CaCl_2$ brine), mass fraction typically between 15% and 40%, an emulsifier, and different types of particles such as clay, lime and barite. It has been shown before for both CO_2 and CH_4 at these fluids are more soluble in oil than in the brine, to such an extent that the dissolution of CO_2 and CH_4 into oil-based drilling fluids can be assumed to be only in the base oil.

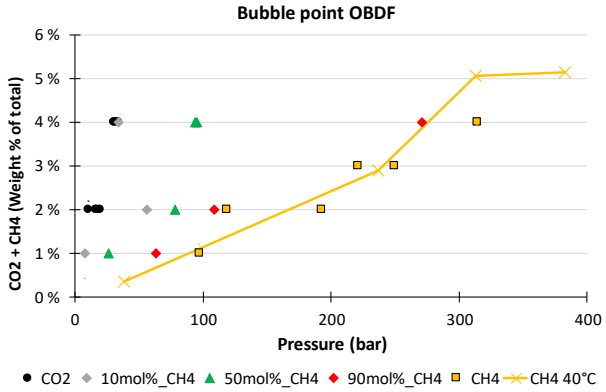

FIGURE 2: Bubble point curves of CO_2, CH_4, and CO_2-CH_4 mixtures in OBDF, at ambient temperature. The points "*CH4 40°C*" are taken for comparison from Torsvik at al. (2016)[6]. The points for CO_2 are from Skogestad et al (2024)[1]. The dotted lines indicate linear regression (passing by the origin) for each data series.

The solubility of CO_2 and CH_4 in OBDF is shown in **FIGURE 2**. We first note that bubble point with CH_4 dissolved is much larger than that for CO_2 for a given mass content, reflecting that the CO_2 solubility is much larger than the CH_4 solubility in the OBDF. The CO_2-CH_4 mixture bubble point curves are in between pure CO_2 and pure CH_4 curves. To better explain these results, we have plotted in **FIGURE 3**, the same bubble point results as a function of the concentration of (a) CH_4 content only and (b) CO_2 only. Here, we see that when plotting the data as a function of CH_4 content, most points collapse on one single curve. This shows that in experiments with CO_2-CH_4 mixtures, the resulting bubble point reflects the formation of CH_4 bubbles, thus the CH_4 bubble nucleation is not affected by the presence of dissolved CO_2. Only in the curve with 10 mol% CH_4, the measured bubble point seems larger than would be expected with CH_4 only. In this case, we see in **FIGURE 3** (b) that the measured bubble point is close to the bubble point of CO_2 only, showing that in this case, the bubble point probably reveals the apparition of CO_2 bubbles.

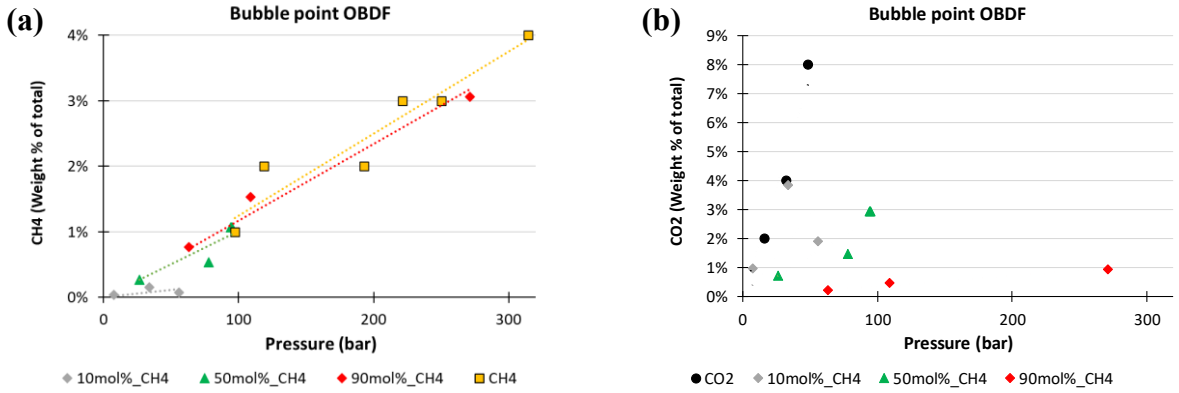

FIGURE 3: (a) Bubble point curves of CH_4 and CO_2-CH_4 mixtures, plotted as a function of the CH_4 content. (b) Bubble point curves of CO_2 and CO_2-CH_4 mixtures, plotted as a function of the CO_2 content. For both graphs, the doted lines indicate linear regression (passing by the origin) for each data series.

To summarize this part, the bubble point of CO_2-CH_4 mixtures seems to follow two distinct trends:

- With 50mol% CH_4 or more, the bubble point is equal to the bubble point of pure CH_4 and is unaffected by the presence of CO_2.
- With 10mol % CH_4, the bubble point aligns with the bubble point of CO_2.

Effect on drilling fluid density

The density of OBDF after gas dissolution has been measured at room temperature. The reference density at 400 bar and no dissolved gas is 1515 kg/m^3. The results are given in **FIGURE 4**. As reported before, CO_2 dissolution tends to decrease the OBDF density[1], by about 3% for 4% of CO_2 content. Our results show that CH_4 reduces even more the density, up to 15% for 4% of CH_4 content. CO_2-CH_4 mixes lead to intermediate values of density, with increasing density reduction with increasing CH_4 content.

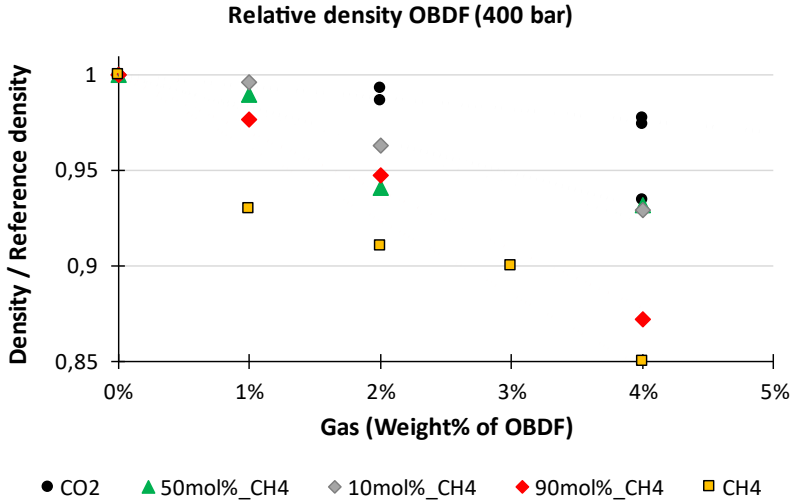

FIGURE 4: Effect of the dissolution of CO_2, CH_4 and CO_2-CH_4 mixtures on the density of OBDF, at room temperature. The points for CO_2 are from Skogestad et al (2014)[1].

Effect on rheological properties

A previous study[1] has investigated how the apparent viscosity of OBDF is affected by the pressure and temperature conditions, as well as the amount of dissolved CO_2. Results are illustrated in **FIGURE 5**. CO_2 dissolution in the oil-based drilling fluids strongly reduces the apparent viscosity; the flow curves are one order of magnitude lower when 8% CO_2 (by weight of the total mix) is dissolved. The results also showed that increasing the temperature decreased the apparent viscosity of the drilling fluids, this observation is valid with and without CO_2 dissolution. The same study showed that pressure conditions also slightly affect the flow curve: higher pressure leads to increased apparent viscosity (results not shown here). However, the effect of pressure is minor compared to the effect of temperature and CO_2 dissolution.

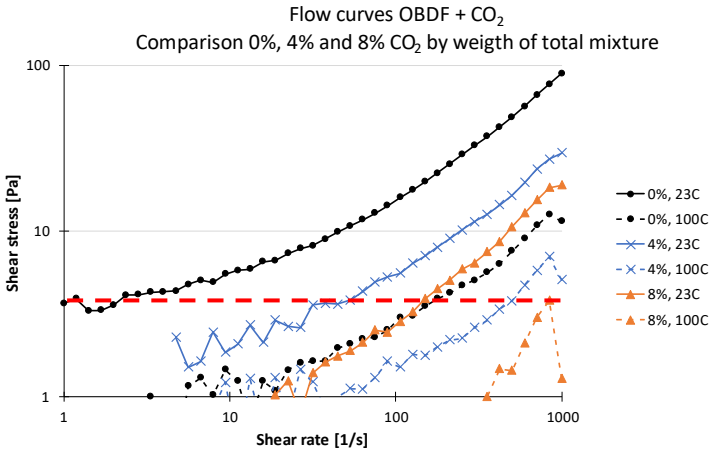

FIGURE 5: Effect of CO_2 loading and temperature on the rheological properties of OBDF. Gathering of all experimental results at 200 bar. Graph adapted from Skogestad et al. (2024)[1]. The red dotted line indicates the stress accuracy limit of the high pressure measuring cell.

Torsvik et al. (2016)[6] also showed that CH_4 dissolution reduces the apparent viscosity of oil-based drilling fluids. In **FIGURE 6**, we show the flow curves measured for different mixing proportions of CH_4 and CO_2. For both gas content (2% and 4% by weight), the apparent viscosity seems to decrease with the CH_4 content. This effect is minor compared to the points previously discussed, i.e., the impact of total gas content and temperature.

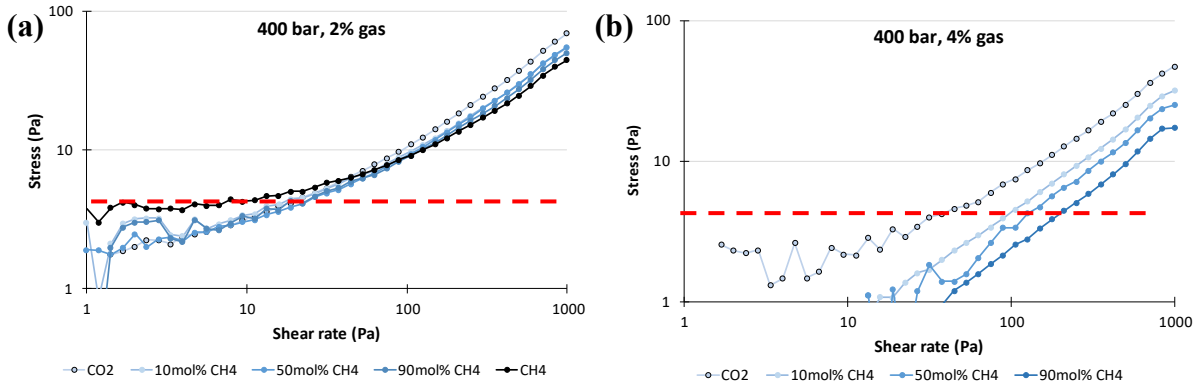

FIGURE 6: Effect of the dissolution of CO_2-CH_4 mixtures on the flow curves of OBDF, at 400 bar and room temperature, for different proportions of CH_4. The total mass fraction of gas is (a) 2% and (b) 4%. The red dotted lines indicate the shear stress accuracy limit of the high-pressure measuring cell.

Water-based drilling fluids

Results of solubility experiments of CO_2 in WBDF1_field and WBDF2 and density have been published before[2], at different temperatures. They showed that the solubility of CO_2 in the water-based drilling fluids is much lower than in oil-based fluids. The maximal solubility at ambient temperature (23°C) is about 3% CO_2 by weight of the total mixture for both drilling fluids under investigation; the bubble point is in this case close to 60 bar. Increasing the pressure further does not increase the solubility of CO_2.

Solubility curves of CO2 and CO2-CH4 mixtures

First, we compare in **FIGURE 7** the solubility curve of WBDF1_factory with the curve from WBDF1_field[2]. The solubility curves are similar for both batches of drilling fluid.

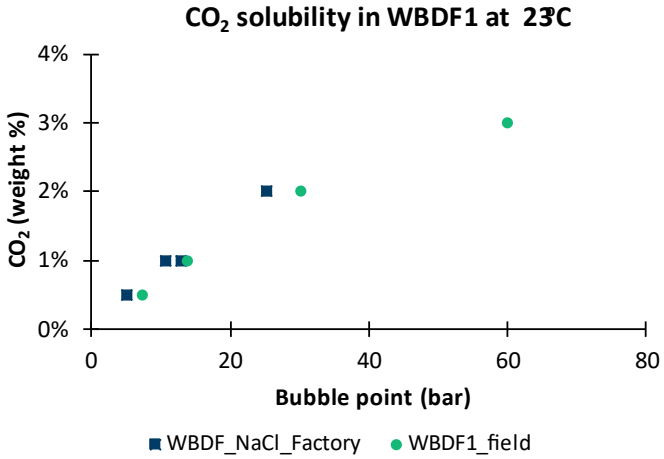

FIGURE 7: Bubble point curves of pure CO_2 in both batches of WBDF1. The data from WBDF1_field has already been published[2]

Next, we focus on solubility experiments for CO_2-CH_4 mixes in WBDF1_factory. In **FIGURE 8** (a), we show pressure -volume relations obtained from the solubility experiments at different total gas fractions, with 10mol% CH_4 in the gas. No distinct change of slope can be observed on these curves. On the contrary, the curves reveal a smooth change of slope as we reduce the pressure. This reflects that we cannot identify a bubble point. In some experiments, we observed small steps on the curves, However, when we repeated the tests (see for example the curves at 1% gas), we noted that these steps were not reproducible; we believe therefore that the steps are experimental artifacts, maybe particles hindering the smooth displacement of the piston in the mixing cylinder.

The absence of a distinct bubble point may indicate that CH_4 is never fully dissolved in WBDF1_factory. To confirm this hypothesis, we have plotted in **FIGURE 8** (b), the theoretical pressure-volume relation calculated with the assumption that no CH_4 is dissolved at all in the drilling fluids. The calculation method is as follows.

- We assume that the bubble point of CO_2 (about 20 bar for 1.9% CO_2) is not affected by the presence of the CH_4 phase.
- For pressure above the bubble point of CO_2,
    - We assume that there are two phases in the mixing cylinder: (1) the CH_4 phase and (2) the drilling fluid phase with dissolved CO_2. The mass of each of the phase is constant.
    - The density of the CH_4 phase at 23°C is taken from the NIST database. The density of the drilling fluid-CO_2 is experimental data[2].
    - The total volume is the sum of the volumes of the CH_4 and the drilling fluid (+ dissolved CO_2) phases
- For pressures below the bubble point of CO_2,
    - We assume that the relation between the mass of dissolved CO_2 and the pressure is linear (i.e., follows Henry's law)
    - The density of the CO_2 phase at 23°C is taken from the NIST database
    - The total volume is the sum of the volumes of the CH_4, CO2 and drilling fluid (+ dissolved CO_2) phases.

The resulting theoretical curve is compared with the experimental curve in **FIGURE 8** (b). We observe that the curves are quite similar to each other, with the increase of volume related mainly to the CH_4 phase. We can also note that the bubble point of CO_2 on the theoretical curve

is characterized by a very small change of slope. Therefore, even if gas CO_2 is released during the experiments, we might not be able to see it on the experimental curve.

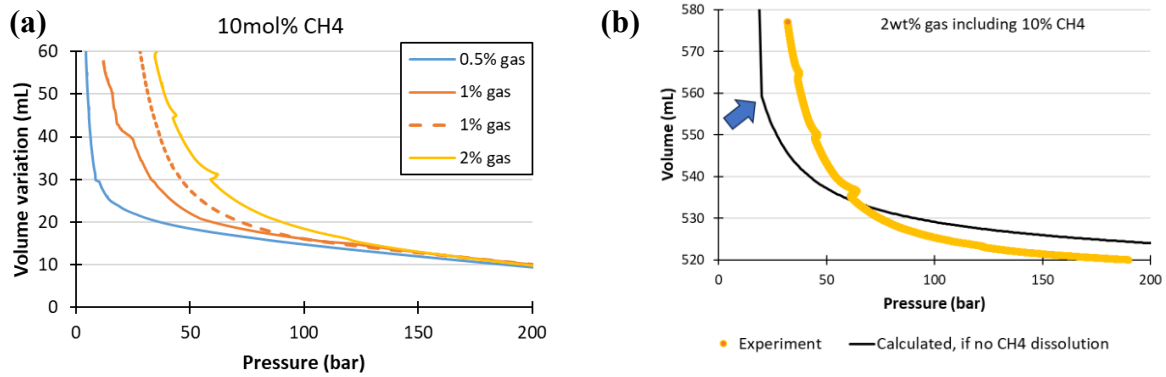

FIGURE 8: (a) Curves obtained during solubility measurements of CO_2-CH_4 mixtures in WBDF1_factory, the total gas constant varies between 0.5% and 2%, while the CH_4 molar fraction in the gas is kept constant (10%) (b) For the test with 2% gas, comparison of the experimental pressure-volume curve with a theoretical curve (see explanation in text). The blue arrow indicates the bubble point of CO_2 (25 bar).

Density and rheological properties

No density or rheological measurements have been performed with CO_2-CH_4 mixtures in water-based drilling fluids as no single phase system exists for this fluid mixture. The density results of drilling fluids with dissolved CO_2 have been already published, they show very little effect from CO_2 dissolution on the density of WBDF1_field and WBDF2.

In **FIGURE 9**, we observe the effect of CO_2 dissolution on the rheological properties of drilling fluids. For both WBDF1_field and WBDF2, the apparent viscosity is reduced when drilling fluid is subject to CO_2 dissolution. The impact from CO_2 is, however, much smaller for water-based drilling fluids than OBDF (see **FIGURE 6**).

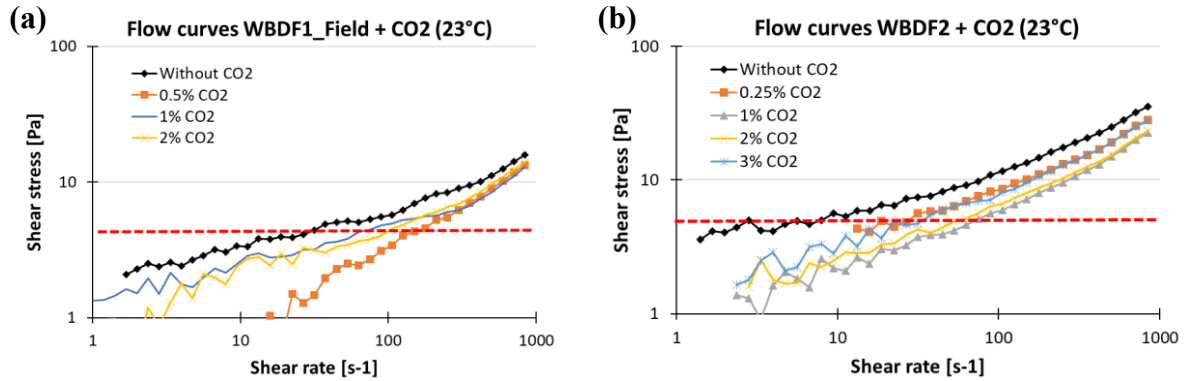

FIGURE 9: Effect of CO_2 dissolution on the flow curves of (a) WBDF1_field and (b) WBDF2. The red dotted lines indicate the stress accuracy limit of the high-pressure measuring cell.

CONCLUSIONS

In this paper we investigate the solubility of CH_4 and carbon dioxide in drilling fluids, and the effect of the dissolution on the density and apparent viscosity. The following observations have been made:

- The solubility of CO_2 is higher than CH_4 in oil-based drilling fluids. When CO_2-CH_4 mixtures are dissolved, the resulting bubble corresponds to the bubble point for CH_4 - drilling fluid for CH_4 ratio above 50mol% for the CO_2-CH_4 mixtures.
- In water-based fluids, CO_2 reveals lower solubility than in OBDF; while it was not possible to fully dissolve CH_4 in water-based drilling fluids at the concentration tested.
- Gas dissolution reduces the density of OBDF, and CH_4 has a larger density-reduction effect than CO_2.
- Gas dissolution reduces the apparent viscosity of all the drilling fluids. In OBDF, CH_4 reveal a larger viscosity-reduction effect than CO_2.

ACKNOWLEDGEMENTS

The work was funded by Gassnova, Equinor, Shell, EBN, ENI and eDrilling through the Climit-Demo project 622128 “Well control for CO_2 wells”. The authors also thank BakerHughes for providing fluids for the experiments.

REFERENCES

(1) Skogestad, J. O.; Feneuil, B.; N’Gouamba, E.; Linga, H.; Aasen, A.; Skår, G.; Roggeband, S. M.; Nedrum, J.; Helgeland, S. CCS Well Control Impact of CO2 on Drilling Fluid Performance. In *IADC/SPE International Drilling Conference and Exhibition*; SPE: Galveston, Texas, USA, 2024; p D021S018R004. https://doi.org/10.2118/217711-MS.

(2) Skogestad, J. O.; Lund, B.; Feneuil, B.; N’Gouamba, E.; Aasen, A.; Linga, H.; Vold, L.; Bruton, Z.; Helgeland, S.; Ødegård, S. I. CO2 Well Control Scenario Prediction Using Experimentally Verified Models. In *SPE/IADC International Drilling Conference and Exhibition*; SPE: Stavanger, Norway, 2025; Vol. SPE-223812-MS, p D021S022R001. https://doi.org/10.2118/223812-MS.

(3) Skogestad, J. O.; Feneuil, B.; N’Gouamba, E.; Linga, H.; Aasen, A.; Skår, G.; Roggeband, S. M.; Nedrum, J.; Helgeland, S. Assessing Hydrate Formation Risk in Infill CCS Wells. In *Paper OMAE2024-122640 presented at the ASME 2024 43rd International Conference on Ocean, Offshore and Arctic Engineering*; American Society of Mechanical Engineers: Singapore, Singapore, 2024; p V008T11A057. https://doi.org/10.1115/OMAE2024-122640.

(4) N’Gouamba, E.; Feneuil, B.; Skogestad, J. O.; Linga, H.; Skår, G.; Roggeband, S. M.; Nedrum, J.; Ødegård, S. I. Integrity of Drilling Fluid As Primary Barrier for CCS Wells. In *Paper OMAE2024-128597 presented at the ASME 2024 43rd International Conference on Ocean, Offshore and Arctic Engineering*; American Society of Mechanical Engineers: Singapore, Singapore, 2024; p V008T11A041. https://doi.org/10.1115/OMAE2024-128597.

(5) N’Gouamba, E.; Feneuil, B.; Skogestad, J. O.; Linga, H.; Ødegård, S. I. CO2 Hydrate Inhibition in Drilling Fluids Using Mono-Ethylene Glycol. *Paper OMAE2025-156972 accepted for presentation at the 44th International Conference on Ocean, Offshore and Arctic Engineering* **2025**.

(6) Torsvik, A.; Skogestad, J. O.; Linga, H. Impact on Oil-Based Drilling Fluid Properties from Gas Influx at HPHT Conditions. In *IADC/SPE Drilling Conference and Exhibition*; SPE: Fort Worth, Texas, USA, 2016; p D031S019R004. https://doi.org/10.2118/178860-MS.

(7) Torsvik, A.; Myrseth, V.; Linga, H. Drilling Fluid Rheology at Challenging Drilling Conditions – an Experimental Study Using a 1000 Bar Pressure Cell. *Annual Transactions of the Nordic Rheology Society* **2015**.

RHEOLOGICAL CHARACTERIZATION OF BITUMINOUS COMPOUNDS FOR THE OPTIMIZATION OF ROOFING MEMBRANES

Fabio Curto[1], Laura Pellicano[1], Stefano Carrà[1], Anke Wendtland[2], Daniela Bush[2]

[1]Mapei Spa, R&D Corporate Lab, Via Cafiero, 22, Milan, Italy
[2]Rasco Bitumentechnik GmbH, R&D Lab, Imkerweg 32 b
32832 Augustdorf, Germany

ABSTRACT

Bitumen and polymer blends represent important compounds for the production of waterproofing membranes for the roofing industry. The addition of a polymer is fundamental to improve performance and mechanical characteristics. On the other hand, compatibility between asphalt and polymers is a crucial factor which deeply affect the thermo-mechanical and rheological properties of bituminous compounds. As a matter of fact, the low compatibility between polymer and bitumen is the root of many problems in the formulation of bituminous blends. A careful selection of the raw materials needed for the optimization of the final characteristics for the formulation of the bitumen-polymer compounds, used in the production of waterproofing membranes. Polyolefins and elastomers are commonly used in this kind of products, thanks to their compatibility with bitumen. The following study investigates the role of quantity and type of polymer to produce bituminous waterproofing membranes, by comparing the performance of different bitumen and polymer combinations (radial and linear SBS) through rheological tests. The bituminous compounds were tested with a strain-controlled rheometer by using a "temperature sweep" protocol, an oscillatory test in which both components of the moduli (G', elastic and G'', viscous) were evaluated by cooling the sample at a fixed frequency within the viscoelastic region. This kind of analysis gives an interesting insight into the behaviour of the bituminous compounds in a wide range of temperatures.

INTRODUCTION

Bituminous membranes consist primarily of bitumen, polymers, and an inert filler. The use of polymer-modified bitumen (PMB) is currently the standard choice for the production of bituminous water-proofing membranes, since the modification with a polymer significantly increases the viscoelastic properties of raw bitumen, especially at low temperatures.

However, the compatibility between bitumen and polymer is a critical factor in this kind of formulation; a careful selection of both components is necessary to achieve the desired final properties. Bitumen itself is a complex mixture of many components and each type of bitumen possesses a unique chemical composition, which determines different chemical interaction with the modifying polymer.

Additionally, the chemical nature of the polymer plays a key role. Commercially available SBS (styrene-butadiene-styrene) polymers with various structures—radial, linear, and diblock—and different PB/PS ratios are commonly employed to modify bitumen[1,2,3]. The structural differences among these polymers are highly significant, as they directly influence the performance level of the resulting PMB[4].

The degree of compatibility between bitumen and polymers is a critical factor in the production of bituminous membranes, as it directly affects the thermodynamic stability of the

final product over time. Compatibility refers to the ability of bitumen to integrate intimately with a polymer, forming a biphasic morphological structure in which the polymer establishes a continuous and dominant phase, while the bitumen remains dispersed in a discontinuous phase[5].

Thermal susceptibility is another key aspect to understand the thermal stability of the compounds and their ability to maintain the desired properties under varying temperature conditions. This parameter significantly influences the performance of the modified material, making it a fundamental point to consider in PMB formulation. Classical laboratory tests performed at fixed temperatures provide only a limited perspective on the material's behaviour as a function of temperature. This limitation highlights the need to complement standard tests with advanced rheological and mechanical characterization techniques[6]. These advanced methodologies enable a deeper understanding of the modified bitumen's behaviour, facilitating the identification, optimization, and exploitation of the interactions between various bitumen types and polymers.

The following study investigates the role of quantity and structure of polymer to produce bituminous waterproofing membranes, by comparing the performance of different bitumen and polymer combinations (radial and linear SBS) through rheological tests.

MATERIALS AND METHODS

Materials

Bituminous membranes were prepared by using bitumen 160/220 mixed with 9% tall oil. To this mixture two different types of SBS (linear and radial SBS) were added in two different percentages (5% and 8%).

PMB compounds were prepared as follows: bitumen, previously heated in an oven, is placed on a heating plate. At 180 °C, the filler is gradually added stirring between 200 and 500 rpm. When the latter is completely dispersed, the modifying polymer is added. Then, the stirring is progressively increased up to a maximum of 2000 rpm at 180-190 °C.

Test methods

DMA: Thermo-mechanical properties of the polymers (linear and radial SBS) were evaluated using a dynamic mechanical analyser, which measures the elastic modulus (E') through oscillatory measurements. The polymeric samples were tested with a ramp from -150°C to 50°C at 2°C/min, with 30 μm displacement at 1 Hz, using the "single cantilever" geometry.

DSR: A strain-controlled dynamic shear rheometer (702e by Anton Paar) was used to measure the rheological properties of the samples. The linear viscoelastic region (LVR) was preliminarily evaluated at three different temperatures (120°C, 60°C and 20°C) with an amplitude sweep, to select a suitable shear strain for the subsequent temperature sweep test. The temperature sweep was performed from 150°C to 20°C with a cooling rate of 2°C/min, applying 0.1% shear strain at 1 Hz to measure the storage modulus (G') and loss modulus (G").

RESULTS AND DISCUSSION

The DMA characterization of the polymers was performed to highlight the influence of the different morphology on their thermo-mechanical properties. From **Fig. 1** it can be noticed that linear SBS possesses a higher rigidity at low temperatures, which becomes comparable to the radial one for temperatures higher than -100°C. Both polymers show the same glass transition temperature around -86°C; linear SBS presents also an additional peak at -110°C.

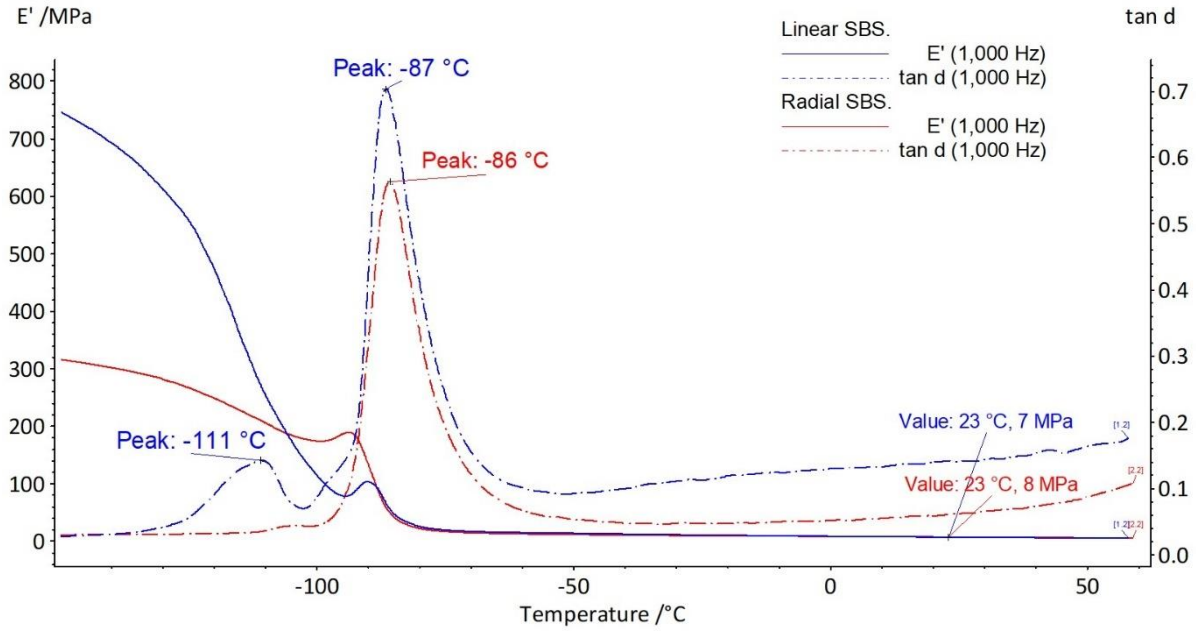

FIGURE 1: DMA characterization of linear and radial SBS

First, an amplitude sweep test was performed to evaluate LVR at different temperatures; one sample is shown in **Fig. 2** as an example. As expected, an increase in both G' and G'' moduli is observed by reducing the temperature; at the same time, the width of the linear viscoelastic region progressively decreases with temperature. The peculiar behaviour at 60°C, where the moduli values are almost overlapping, is confirmed by the temperature sweep test and discussed below.

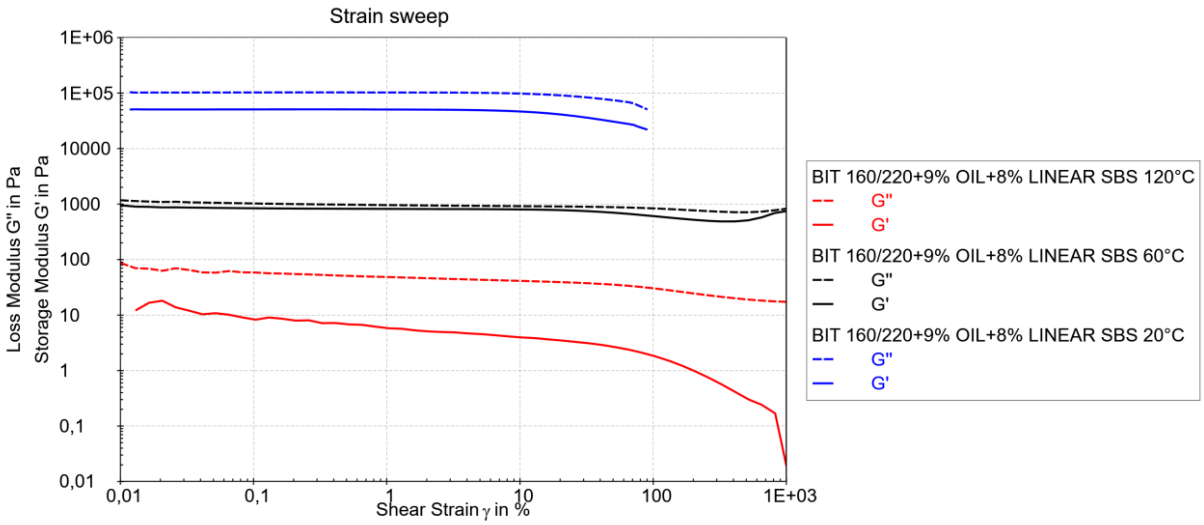

FIGURE 2: Determination of LVR at different temperatures

Then, the temperature sweep test was performed on all samples. The rheological profile obtained for the unmodified bitumen sample (**Fig. 3**) is characteristic of a system with no distinct texture, exhibiting a predominantly viscous response, with the loss modulus (G") much exceeding the storage modulus (G') in the entire temperature range. In the same graph a sample of raw bitumen, without the addition of oil, is also shown for a comparison. Tall oil is commonly

used as a modifier for bitumen, since it is widely available as a by-product and it can significantly increase the viscous response of asphalt binders, resulting in better low-temperature properties but reduced high-temperature properties[7].

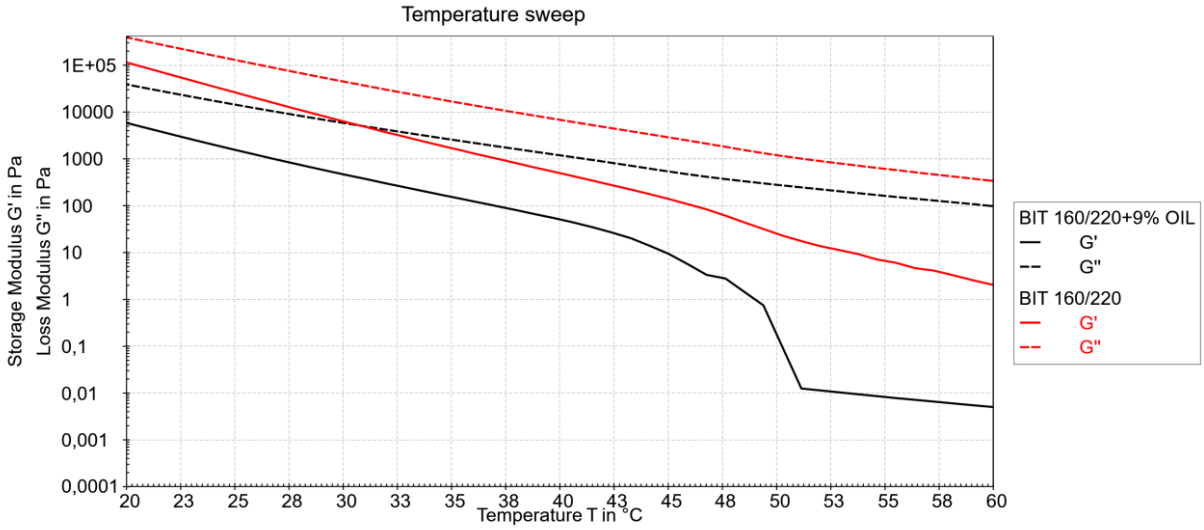

FIGURE 3: Effect of tall oil on the temperature sweep test

Modification with SBS significantly enhances the viscoelastic response of the bitumen, as testified by an increase in both components of the modulus, G' and G'', as can be easily observed from the values reported in **Tab. 1**. The viscoelastic properties of the PMBs are determined by the polymer morphology, the chemical composition of the bitumen, and the nature of their interactions. When SBS copolymers are incorporated into the bitumen, intermolecular interactions occur between the bitumen and the PS (polystyrene) and PB (polybutadiene) blocks of the SBS[8]. This leads to the formation of a rubbery supporting network within the modified bitumen, which contributes to increased moduli, particularly by enhancing the elastic response.

TABLE 1: G' and G'' values at different temperatures

	40°C		70°C		90°C		120°C		T cross/ °C
	G'/Pa	G''/Pa	G'/Pa	G''/Pa	G'/Pa	G''/Pa	G'/Pa	G''/Pa	
Bitumen + 9% oil	54	1242	$2 \cdot 10^{-3}$	41	$5 \cdot 10^{-4}$	9	$9 \cdot 10^{-5}$	2	-
5% radial polymer	2775	4725	482	509	130	252	12	55	-
8% radial polymer	12778	6908	2176	3303	349	947	30	170	30; 63
5% linear polymer	606	2996	3	116	$1 \cdot 10^{-3}$	28	$3 \cdot 10^{-4}$	5	-
8% linear polymer	2879	4663	727	466	272	294	2	19	55; 90

From the comparison of **Fig. 4** and **Fig. 5** it emerges that both the quantity and the morphology of the modifying polymer deeply affect the viscoelastic properties of the system.

An increasing percentage of the polymer leads not only to an increase of the moduli value, but also to a different relation between G' and G''; this is especially apparent in the case of linear SBS. In fact, a different degree of modification of the PMB is associated to a change in the microstructure of the material.

The morphology of SBS also plays a pivotal role: thanks to is architecture, radial SBS is more likely to form a rigid and robust three-dimensional network within the bituminous matrix. On the other side, linear SBS has weaker interactions with the bitumen. In fact, 5% of linear SBS has much less impact on the rheological behaviour compared to 5% of radial SBS.

It can be observed that 8% of modifying polymer induces a structural change that radically influences the rheological properties at intermediate temperatures (approximately 40°C-70°C for radial SBS and 50°C-90°C for linear SBS). In this temperature range, the response become more elastic and the storage modulus G' prevails over G''. This surprising behaviour is probably ascribable to the complexity of the PMB structure, especially with SBS as a modifying polymer; the different glass transition temperatures of polystyrene and polybutadiene blocks must be taken into consideration.

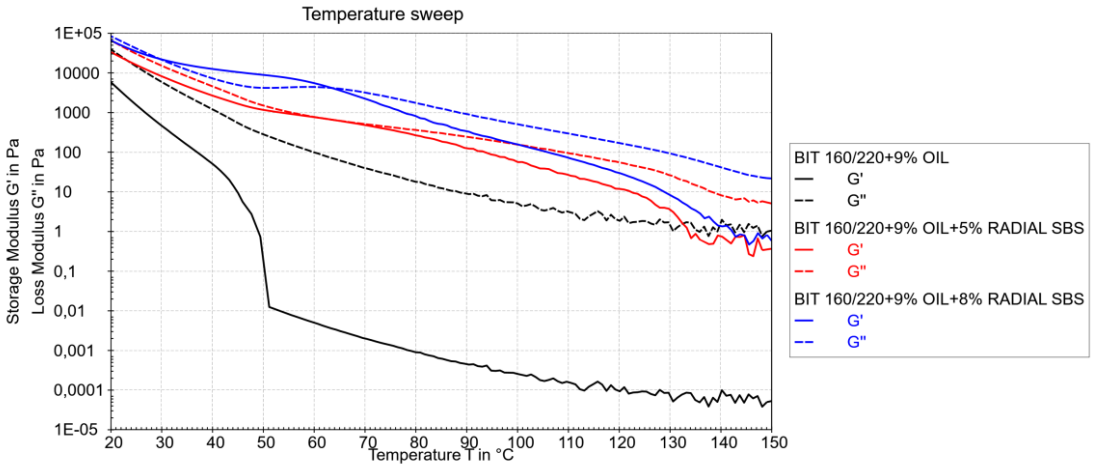

FIGURE 4: Effect of radial SBS on temperature sweep test

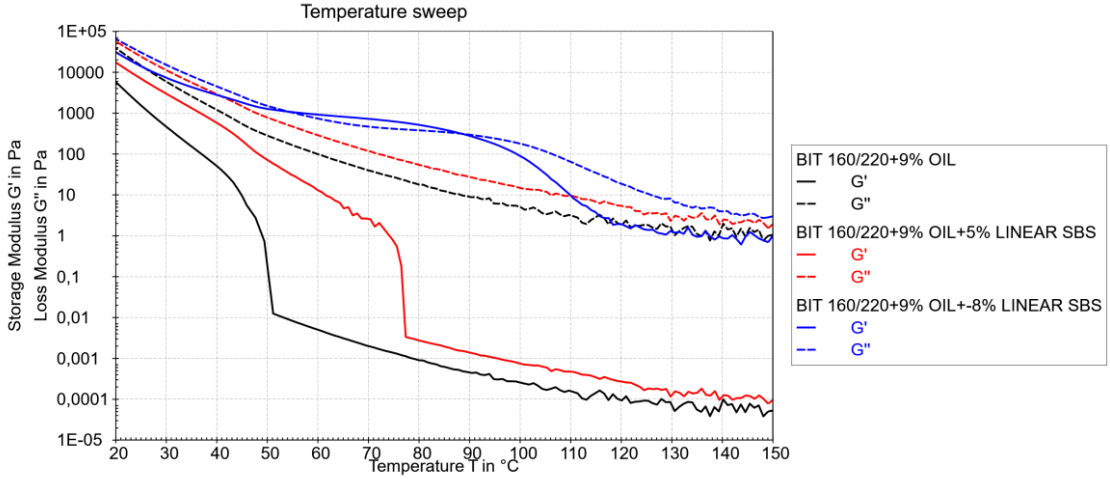

FIGURE 5: Effect of linear SBS on temperature sweep test

CONCLUSION

The rheological analysis conducted on SBS-modified bitumen compounds provided a deep and complex description of the material behaviour over a wide temperature range. The results demonstrate that the incorporation of SBS polymers significantly enhances the viscoelastic properties of bitumen. However, the degree of compatibility between the bitumen matrix and the SBS polymer plays a pivotal role in determining the overall performance of the composite material.

The different architectures of SBS polymers—linear and radial—have a substantial influence on the rheological response of the compound, leading to different performance characteristics that must be carefully considered during the formulation of bituminous membranes. These findings are particularly pertinent to the design and optimization of waterproofing membranes, where both thermal and mechanical properties are critical for ensuring the long-term durability and reliability of the final product.

The appropriate selection of SBS polymer types is crucial from an applicative point of view, since bituminous membranes require a precise balance between thermal stress resistance and adhesion to the substrate[6]. Rheological evaluations further affirm that achieving optimal performance necessitates the careful selection of bitumen and SBS polymer combinations, tailored to the specific demands of the application and local climatic conditions.

REFERENCES

Bibliography

1. Lu, X., Isacsson, U.: Rheological characterization of styrene-butadiene-styrene copolymer modified bitumens. *Constr. Build. Mater. 11, 23–32* **1997**
2. Fawcett, A., McNally, T.: Polystyrene and asphaltene micelles within blends with a bitumen of an SBS block copolymer and styrene and butadiene ho-mopolymers. *Colloid Polym. Sci. 281, 203–213* **2003**
3. Ocelic Bulatovic, V., Rek, V., Jurkaš Marković, K.: Effect of polymer modifiers on the properties of bitumen. *Journal of Elastomers & Plastics 45 (1), 33-47* **2013**
4. Lesueur, D.: The colloidal structure of bitumen: Consequences on the rheology and on the mechanisms of bitumen modification. *Advances in Colloid and Interface Science 145(1), 42-82* **2009**
5. Yang, C., Xie, X., Wu, S., Amirkhanian, S., Zhou, X., Ye, Q., Yang, D., Hu, R.: Investigation of physicochemical and rheological properties of SARA components separated from bitumen. *Construction and Building Materials 235 117437* **2020**
6. Antunes, I.; Bartucca, C.; Caputo, P.; Carrà, S.; Curto, F.; De Rosa, A.; Pellicano, L.; Oliviero Rossi, C. Rheological analysis: a powerful tool for the characterization of bituminous compounds in the production of waterproofing membranes, *RILEM Transactions*, **2025**.
7. Zhang, F., Zhu, J., Sun, Y., Mariam Benny, C., Wang, D., & Cannone Falchetto, A. (2025). Effect analysis of using tall oil pitch (TOP) to partially extend bitumen in asphalt pavements: comparison of different TOPs. Road Materials and Pavement Design, 1–20 2025. https://doi.org/10.1080/14680629.2025.2483478
8. Masson, J.F., Collins, P., Robertson, G., Woods, J.R., Margeson, J.: Thermo-dynamics, phase diagrams, and stability of bitumen–polymer blends. *Energy Fuels 17(3), 714–724* **2003**

Rheological Behavior of Bentonite-Water Mud Under Elevated Temperatures: Insights for Predicting Fluid Performance

Masoumeh Amiri, Arild Saasen, Mahmoud Khalifeh, Alf Kristian Gjerstad

Department of Energy and Petroleum Eng., Faculty of Science and Technology, University of Stavanger, 4036, Stavanger, Norway

ABSTRACT

During well construction, control of drilling mud rheology is required at elevated temperature and pressure. Therefore, understanding the influencing factors on water-base mud (WBM) rheology characteristics, as one of the most commonly used drilling fluids, is essential to maintain a firm control over rheological properties of elevated temperature WBM. Due to changing the rheological properties of some additives at elevated temperatures, selecting appropriate additives for WBM is challenging.

This study focuses on the behavior of a typical bentonite mud utilizing a state-of-the-art viscometer to measuring drilling fluids properties at different concentrations of bentonite and temperatures. Sensitivity of the mud to shear stress at different temperatures and concentrations was examined. The experimental approach involved mixing distilled water with bentonite and conducting experiments including preparation, and hot rolling to simulate aging of mud during circulation. Rheological properties of the mud were measured at various concentrations (8 and12 g) across temperatures (10 to 90°C) and shear rates (5 to 1021 s^{-1}) to identify patterns for predicting the mud behavior.

The results show that the rate of shear stress increase is a strong function of temperature in the applied shear rate range. Plastic viscosity decreased with temperature, being highest at 10°C and lowest at 90°C. Additionally, temperature increase leads to increased yield stress. It is believed that at higher temperature face to face repulsive electrostatic energy between particles is higher. Additionally, higher temperatures led to an increased yield stress due to stronger particle interactions. It is proposed that, as a result of these enhanced interactions at higher temperatures, a more robust gel structure would be formed. The experimental data closely fit the Herschel-Bulkley model, confirming its suitability for predicting bentonite mud behavior under varying temperatures and shear rates.

This study provides deeper understanding of how temperature and bentonite concentration influence the rheology of bentonite muds. Also, these findings highlight the complexity of maintaining mud rheology at elevated temperatures, as viscosity changes can affect mud stability and drilling efficiency. Moreover, it offers practical insights for optimizing bentonite concentrations to ensure efficiency in field applications for elevated temperature conditions.

Key words: Rheology characteristics; temperature effect; Bentonite muds

Introduction

Understanding the rheological properties of drilling fluids under elevated pressures and temperatures is crucial for any drilling operation. In deeper formations where such conditions are encountered, predicting the rheological characteristics of drilling fluids is essential to ensure their performance and stability[1]. One of the key components in top hole water-based fluid systems is bentonite clay, due to its cost-effectiveness, environmental advantages, swelling capacity, and gel-structure formation [2]. Acquiring knowledge about the rheological properties of bentonite is critical for improving drilling fluid performance in terms of wellbore cleaning efficiency, managing pressure losses, and controlling equivalent circulation density[2].

Several studies have shown that the effect of pressure on the rheology of water-based drilling fluids is negligible[3]. However, temperature can significantly influence the rheological properties of water-bentonite dispersions in various ways[4].

For instance, Mohammed et al.,[5] investigated the rheological characteristics of three different bentonite concentrations (2, 4, and 6 wt%) at three temperatures (25°C, 55°C, and 85°C), both with and without nano-Fe_2O_3. Their results showed that yield stress decreased with increasing temperature at all concentrations. Generally, higher bentonite concentrations resulted in greater plastic viscosity and apparent viscosity. However, both plastic viscosity and apparent viscosity decreased as temperature increased.

In a separate study, Vryzas et al.,[4] examined the rheology of Wyoming sodium bentonite at a 7.0% mass concentration (45.16 g bentonite in 600 ml deionized water) across a wide temperature range (25°C to 80°C) under ambient pressure. Contrary to prior studies, they observed that at low shear rates, shear stress increased with temperature, whereas at high shear rates, the shear stresses converged to similar values. Their samples, analyzed using the Herschel-Bulkley model, revealed that yield stress increased with temperature, while the flow consistency index decreased, and the flow behavior index increased with temperature. Similarly, Lin et al.,[6] studied the temperature dependence of the yield stress in clay suspensions (kaolinite and bentonite mixed with distilled water) at various concentrations (15, 20, and 30 wt%) and temperatures (2°C and 25°C). They reported a significant increase in yield stress with increasing temperature, particularly at higher clay concentrations.

This behavior was attributed to the increase in electrostatic repulsive potential between charged clay particles with temperature.

This study focuses on investigating the rheological behavior of bentonite based mud with varying properties at elevated temperatures and different concentrations using a state-of-the-art rheometer. Understanding the combined effects of high temperature and bentonite concentration sensitivity is crucial to maintaining consistent drilling fluid properties, ensuring optimal performance in challenging environments.

Drilling fluid design and preparation

The composition of bentonite muds is presented in **Table1** including the order and duration of mixing:

Table 1: Mix design of WBDF

Ingredients	Function	Content by Weight (g)	Mixing time (min)
Distilled Water	Base fluid	350	-
Bentonite	Elevate viscosity and reduce filtration loss	8 and 12	10

Experimental Procedure

The methodology is divided into two steps: before hot rolling (BHR) and after hot rolling (AHR).

In the first step (BHR) the mentioned compositions were mixed using Silverson L4RT- a high-speed mechanical homogenization and emulsification shown in **Fig. 1.**

FIGURE 1: Blade used to shear the fluid during drilling fluid preparation

To avoid agglomeration the process of adding bentonite should be done very slow. Also, mixing time plays an important role in water base mud mixing.

The pH of drilling fluid was measured by a pH meter). To improving chemical solubility and performance of drilling mud, as well as for protecting drilling and completion tools from corrosion, pH of water-base drilling muds is generally maintained in the 8 to 12 [6].

To investigate the flow behaviour of this drilling mud, rheology parameters like yield stress and apparent viscosity were recorded using a versatile rheometer-model MCR302.

In the second step to simulate a wellbore mud circulation in the laboratory a roller oven and mud aging cell were used. Hot rolling is conducted to assess changes of mud properties after a mud circulation at a specific temperature. The mud samples were hot rolled at 90 ºC for 16 hours at atmospheric pressure.

After hot rolling the mud sample placed in the rheometer cell at the mentioned temperature. To reduce the effect of evaporation pressure cell was used. Shear stress readings were taken in 5, 10, 51, 102, 170, 340, 510 and 1021 s^{-1} in ascending order with 10 seconds between each measuring point in order to wait for equilibrium and to measure in a permanent state. The viscosity of the drilling fluids was measured with the same viscometer configuration.

Results

Temperature Effect on Shear Stress at Ambient Pressure

8 grams of bentonite

Rheograms for all six samples containing 8 g of bentonite at the tested temperatures are presented in Fig. 2. As shown, shear stress increases with increasing shear rates across all temperatures. Notably, higher temperatures result in a greater yield stress. At 10°C, the shear stress was 0.079 Pa at the lowest shear rate and 8.6 Pa at the highest. While, at 90°C, the shear stress ranged from 2.01 Pa at the lowest shear rate to 6.01 Pa at the highest. It shows at elevated temperatures and higher shear rates, the observed shear stress values are lower compared to those at lower temperatures.

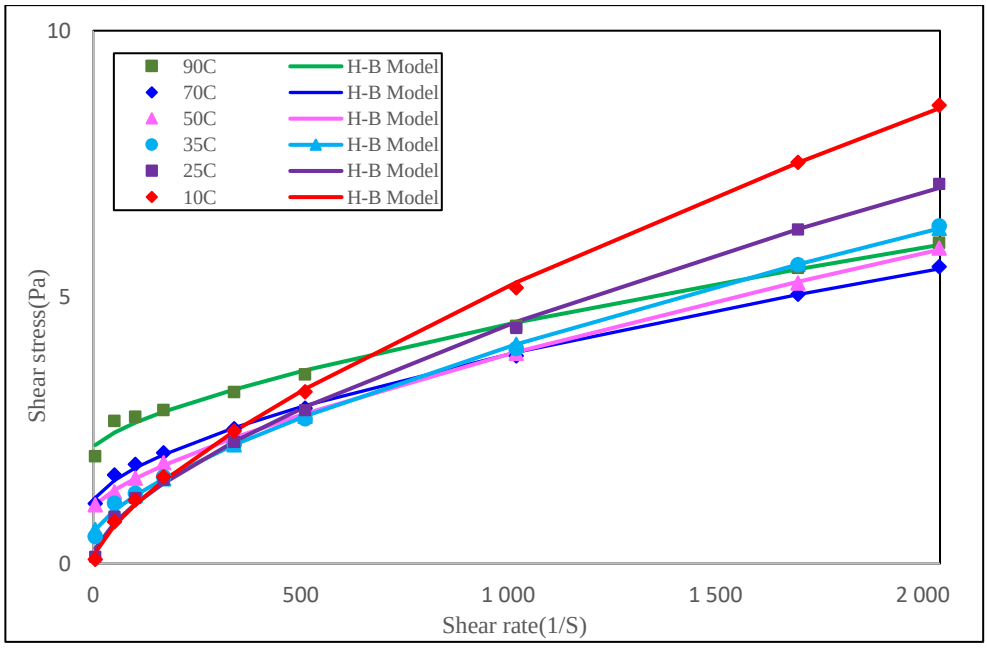

Figure 2. Rheograms of 8 grams of sodium bentonite in water at different temperatures

Table 2. presents the data obtained from fitting the data to the Herschel-Bulkley rheological model. This model demonstrated a strong fit for all sample rheograms, and the corresponding rheological parameters. It is obvious with increasing the temperature yield stress increased. No discernible pattern was observed for the flow consistency index and flow behavior index.

TABLE.2. Herschel-Bulkley rheological parameters of 8 g water- sodium bentonite suspensions at different temperatures.

Herschel- Bulkley Model				
T (°C)	τ_o	k	n	R^2
10	0.08414	0.03972	0.7035	0.9993
25	0.1486	0.04765	0.6529	0.9984
35	0.5441	0.03108	0.6849	0.9986
50	1.05	0.01884	0.7281	0.9997
70	1.141	0.03469	0.6352	0.9981
90	2.165	0.01955	0.692	0.992

12 grams of bentonite

The relationships between shear stress with shear rate for 12 g bentonite drilling mud have been graphed (Fig. 3). The same trend was observed for 12 grams of bentonite. In other words, at lower temperatures (e.g., 10°C), the shear stress is lower (1.48 Pa) compared to higher temperatures like 90ºC which shows shear stress of 7.77Pa at the same shear rate (5 1/s). However, at all shear rates, shear stresses were higher than 8 rams of bentonite.
Also, at lower shear rates, the yield stress exhibits higher values as the temperature increases.

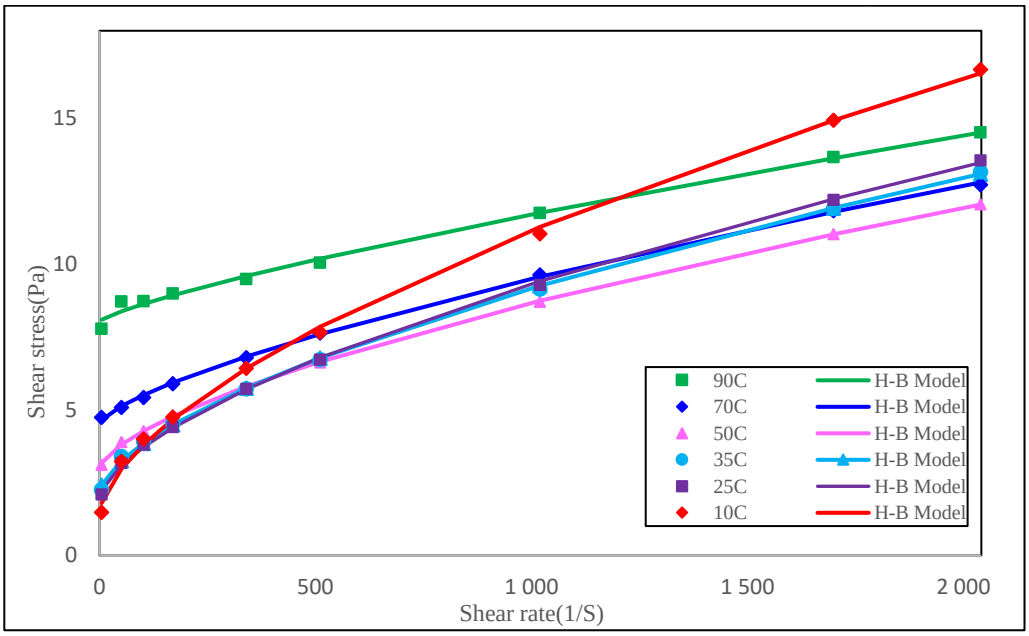

Figure 3. Rheograms of 12 grams of sodium bentonite in water at different temperatures

The Herschel-Bulkley model was found to fit all sample rheograms very well, especially at higher shear rates and the rheological parameters, are shown in Table 3. An increase of yield stress with temperature was observed Also, flow consistency index decreased with temperature while the flow behavior index increased with temperature and tends towards the value of 1.0, indicating that the dispersions become Bingham plastic at higher temperatures.

TABLE 3. Herschel-Bulkley rheological parameters of 12g water- sodium bentonite suspensions at different temperatures.

Herschel- Bulkley Model				
T (ºC)	τ_o	k	n	R^2
10	1.428	0.1348	0.6193	0.9986
25	1.963	0.09558	0.6287	0.9996
35	2.154	0.0954	0.6222	0.9994
50	2.995	0.06182	0.6542	0.9998
70	4.534	0.03503	0.7169	0.9996
90	8.033	0.01483	0.7977	0.9942

Discussion

The rheological parameters reflect the strength and nature of interparticle interactions among clay particles. The observed increase in yield stress with temperature may be attributed to enhanced face-to-face electrostatic repulsive interactions, which intensify as the temperature rises. In such a face-to-face interaction structure, the electrostatic repulsive potential primarily governs the separation distance between adjacent particles. As a result, the particles are drawn into a deep van der Waals potential well. Consequently, as the separation distance decreases, the repulsive potential increases, leading to a corresponding rise in yield stress [6]. Similarly, at higher concentrations, the reduced interparticle distance results in an increased yield stress.
At low shear rates, elevated temperatures increase yield stress due to stronger interparticle repulsive forces. However, at higher shear rates, the clay particle network becomes disrupted. It is hypothesized that at higher temperature, between bentonite particles adhesion occurs and with increasing the temperature the network structure breaks down. After reorganization, bentonite particles show less resistance to flow even at high shear rates. As a result, shear stress decreases with increasing temperature under high shear conditions.

Conclusion

1. The rheological behavior of sodium bentonite dispersions at concentrations of 8 and 12 grams is accurately described by the Herschel-Bulkley model across the entire range of shear rates and temperatures studied.
2. At low shear rates, shear stress increases significantly with temperature, whereas at high shear rates, the lowest temperature yields the highest shear stress.
3. Yield stress exhibits an increasing trend with rising temperature.
4. Higher bentonite concentrations result in increased shear stress and yield stress across all temperatures.

REFERENCES

(1) Amani, M.; Al-Jubouri, M. The Effect of High Pressures and High Temperatures on the Properties of Water Based Drilling Fluids. *Energy Science and Technology* **2012**, *4* (1), 27–33. https://doi.org/10.3968/j.est.1923847920120401.256.

(2) Du, M.; Liu, P.; Clode, P. L.; Liu, J.; Haq, B.; Leong, Y. K. Impact of Additives with Opposing Effects on the Rheological Properties of Bentonite Drilling Mud: Flow, Ageing, Microstructure and Preparation Method. *J Pet Sci Eng* **2020**, *192*. https://doi.org/10.1016/j.petrol.2020.107282.

(3) Alderman, N. J.; Research, C.; Gavignet, ; A; Forex, S.; Guillot, ; D; Schlumberger, D.; Maitland, G. C.; Research, S. C. *SPE High-Temperature, High-Pressure Rheology of Water-Based Muds*. http://onepetro.org/SPEATCE/proceedings-pdf/88SPE/88SPE/SPE-18035-MS/3466275/spe-18035-ms.pdf/1.

(4) Vryzas, Z.; Kelessidis, V. C.; Nalbantian, L.; Zaspalis, V.; Gerogiorgis, D. I.; Wubulikasimu, Y. Effect of Temperature on the Rheological Properties of Neat Aqueous

Wyoming Sodium Bentonite Dispersions. *Appl Clay Sci* **2017**, *136*, 26–36. https://doi.org/10.1016/j.clay.2016.11.007.

(5) Mohammed, A. S. Effect of Temperature on the Rheological Properties with Shear Stress Limit of Iron Oxide Nanoparticle Modified Bentonite Drilling Muds. *Egyptian Journal of Petroleum* **2017**, *26* (3), 791–802. https://doi.org/10.1016/j.ejpe.2016.10.018.

(6) Lin, Y.; Cheah, L. K. J.; Phan-Thien, N.; Khoo, B. C. Effect of Temperature on Rheological Behavior of Kaolinite and Bentonite Suspensions. *Colloids Surf A Physicochem Eng Asp* **2016**, *506*, 1–5. https://doi.org/10.1016/j.colsurfa.2016.06.012.

FLOW CURVES AND FLUID LOSS OF WATER-BASED DRILLING FLUIDS

Blandine Feneuil[1], Bjørnar Lund[1], Inga Synnøve Nordhus[1], Stefan Chisca[1], Marius Sandru[1], Arild Saasen[2], Jan David Ytrehus[1],

[1]SINTEF, NO-7031 Trondheim, Norway
[2]University of Stavanger, NO-4036 Stavanger, Norway

ABSTRACT

A drilling fluid must fulfill numerous functions during well drilling, ranging from particle transport, lubrication, to wall stabilization. In that aim, the composition is carefully chosen by the drilling engineer for each well section according to the required properties such as density, rheological properties, chemical stability and fluid loss. In particular, fluid loss refers to the penetration of the liquid from the drilling fluid into the rock formation. It must be controlled and preferably avoided as it may reduce the permeability of the formation and change the fluid properties due to the depletion of the liquid. Fluids with low fluid loss have the ability to form an impermeable filter cake at the rock surface, i.e., a layer of accumulated particles on the wall of the well.

As interest in CO_2 storage has increased in the last decade, the need to design drilling fluids for CO_2 well drilling has arisen. Lots of knowledge is inherited from oil & gas wells, and still CO_2 wells pose new challenges. These wells should not be optimized for production (receiving fluids from the formation into the well), but for injection (injecting CO_2 from the well to the rock formation). Here, we present an experimental study aiming to optimize drilling fluids rheological properties and fluid loss for CO_2 wells. Flow curves are measured using a Couette cell in an Anton Paar rheometer. Fluid loss and filter cake formation are evaluated with a filterpress. We investigate the effect of the fluid components on the flow curve, the fluid loss and the filter cake mass.

INTRODUCTION

A drilling fluid must fulfill numerous functions during well drilling, ranging from particle transport, lubrication, to wall stabilization. In that aim, the composition is carefully chosen by the drilling engineer for each well section according to the required properties such as density, rheological properties, chemical stability and fluid loss. As interest in CO_2 storage has increased in the last decade, the need to design drilling fluids for CO_2 well drilling has arisen[1]. Lots of knowledge is inherited from oil & gas wells and still CO_2 wells pose new challenges. These wells should not be optimized for production (receiving fluids from the formation into the well), but for injection (injecting CO_2 from the well to the rock formation).

One of the important properties of the drilling fluids is their ability to reduce fluid loss, i.e., penetration of the liquid from the drilling fluid into the rock formation. Fluid loss is undesired as it may reduce the permeability of the formation and change the fluid properties due to the

depletion of the liquid. Fluid with low fluid loss have the ability to form an impermeable filter cake at the rock surface, i.e., a layer of accumulated particles on the wall of the well or in the outer layer of the rock. For CO_2 wells, it is essential that the filter cake does not hinder the injection of CO_2 in the reservoir. Since there is no flow from the formation into the well, there are no mechanisms from the formation to wash back the filter cake or clean out formation damage due to fluid loss.

In this paper, we investigate fluid loss and filter cake formation with different water-based drilling fluids. The paper is divided into two main parts: first, in the experimental part, we investigate the effect of testing conditions and fluid composition on their properties. Secondly, we present a model for the formation of the filter cake and compared it with the experimental data. This study is part of a larger project where we aim to provide methods and tools supporting the choice of drilling fluids for CO2 wells.

MATERIALS AND METHODS

Materials

The drilling fluids have been mixed with a OFITE high speed blender, at rotation velocity 11 500 rpm, first for 15 min for all the ingredients except barite particles, then another 15 min after the addition of barite. The composition for each of the studied drilling fluids are listed in **TABLE 1**. The density of the fluids is about 1200 kg/m^3.

TABLE 1: Drilling fluids used in this paper

	DF_base	DF_cellulose	DF_MEG	DF_PEEK
Tap water (g)	465	465	450	465
Xanthan gum (g)	2.00	2.00	2.00	-
Sulfonated PEEK (sPEEK) (g)	-	-	-	2.00
Soda ash (g)	1.00	1.00	1.00	1.00
KCl (g)	33.0	33.0	33.0	33.0
Cellulose (g)	-	10.0	10.0	10.0
Mono-ethylene glycol (MEG) (g)	-	-	20.0	-
Barite (g)	140	140	140	140

The composition of DF_base is similar to commercial KCl-based drilling fluids. DF_cellulose has the same composition except for the addition of cellulose fibers. In DF_MEG, water is partially replaced by monoethylene glycol (MEG), a common component in drilling fluids to avoid hydrate formation. The MEG content is chosen so that the total volume of liquids is the same in all the drilling fluids (MEG density is 1350 kg/m^3). Finally, in DF_PEEK, we replace Xanthan gum polymer by sulfonated PEEK (sPEEK). Functionalization of PEEK (Polyether ether ketone) is performed in our lab prior to the experiments. This step is necessary to make the polymer hydrophilic and soluble in water. In a typical procedure, 5.5 g of commercial PEEK (Fumion® E 600-PEEK from Fumatech) was dissolved in 75 ml of 97% H_2SO_4 and heated at 80°C for 7 days. After the reaction, the solution was poured in ice cold water, neutralized with sodium hydroxide and used further for preparing water-based fluid.

Hot rolling (HR)

In the field, fluids are reused after being circulated in the well as long as their properties do not change too much. In the well, the fluids are exposed to higher temperature, pressure and mechanical stirring. To check whether these conditions may affect the properties of the drilling fluids, we perform hot rolling where the fluids are placed in a 500 mL cylindrical cell and kept in an oven at 90°C with rotation at 20 rpm for one night. In addition, in some cases, we placed a steel rod in the cell to induce additional shear on the fluids. This procedure is inspired by, and further described in, the work of Klungtvedt and Saasen[2].

Filter press measurements

The filter press experiments are performed with an OFITE HTHP static filtration cell. A schematic drawing of the tests can be seen in **FIGURE 1**. 50 mL of drilling fluid is placed in the chamber on a 11-µm sized filter paper supported by a porous disk with pore size much larger than 11 µm. The top of the chamber is connected to a nitrogen bottle to impose a pressure of 35 bar. The test starts when the bottom or the cell is opened, and the fluid coming out of the drilling fluid (filtrate) is collected. The filtrate volume (fluid loss) is monitored during 30 min, after which the test is stopped. The test leads to the forming of a filter cake, i.e., an agglomeration of particles on the top of the filter paper. After the test, the cell is opened and the remaining fluid at the top of the filter cake is poured out. The filter cake is weighted before (wet mass) and after (dry mass) drying for one night in an oven at 66°C.

The cell is placed in a heating jacket: For the results presented in this paper, tests are performed at room temperature and 50°C.

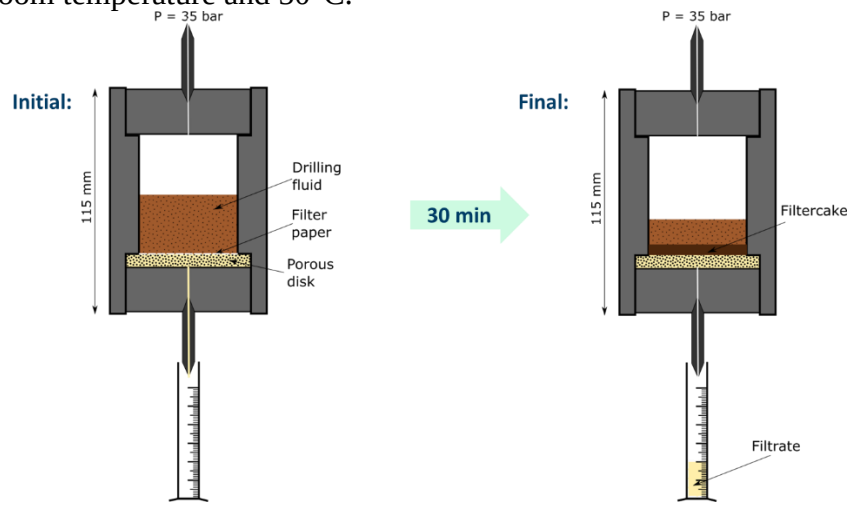

FIGURE 1: Schematic drawing of filter press experiments

Rheology

The rheological properties are derived from tests performed in Anton Paar 102 MRC equipped with a smooth Couette cell. The measuring gap is 1.13 mm, and the rotating cylinder has a diameter of 26.66 mm and a height of 40 mm. The cell is equipped with a Peltier system to control the temperature.

The applied test sequence is as follows. The fluid is presheared for 1 min at 1000 s^{-1}, then left to rest for 10 s. Then, we apply a ramp of increasing shear rates from 0.01 s^{-1} to 1000 s^{-1}, before a decreasing ramp from 100 s^{-1} to 0.01 s^{-1}. The curves shown in this paper are obtained during the decreasing shear rate ramp.

EXPERIMENTAL RESULTS

Effect of hot rolling and test temperature

We have first studied for DF_base the effect of hot rolling and test temperature on the properties for the drilling fluid (see **FIGURE 2**).

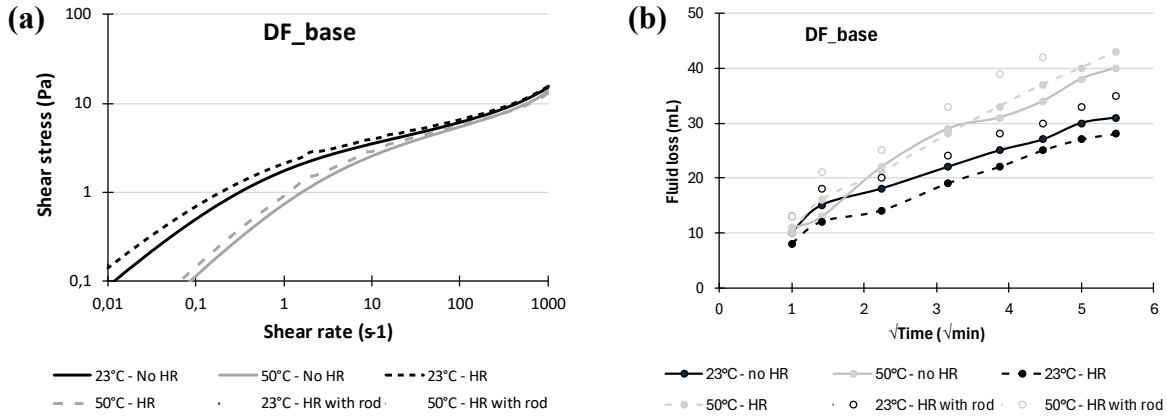

FIGURE 2: Effect of hot rolling (with and without rod) and test temperature on the properties of DF_base. (a) Flow curves (b) Fluid loss curves.

The hot rolling, with or without rod, did not have a major impact on the rheological properties of the drilling fluids, showing that the DF_base composition is adapted to be used in wells at high temperature (see **FIGURE 2** (a)). The temperature in the tests affects the viscosity of the fluids. The viscosity decreases with the test temperature. This is a common observation for water-based drilling fluids. Regarding the fluid loss properties (**FIGURE 2** (b)), hot rolling has a limited effect, while increasing the test temperature increases the fluid loss.

Besides, the test temperature and hot rolling does not seem to have a major effect on the filter cake dry mass, as the values obtained for all the tests are between 9.0 and 13.1 g, with an average of 11.3 g.

Effect of cellulose

Next, we study the effect of cellulose by comparing the flow curves and fluid loss curves of DF_base and DF_cellulose. These results can be seen in FIGURE 3. The cellulose fibers have a major effect on the flow curves of the drilling fluid; it increases the effective viscosity at high shear rate ($> 10\ s^{-1}$) and decreases the effective viscosity at low shear rates ($< 10\ s^{-1}$). Hot rolling has limited effect on the flow curves of the fluids.

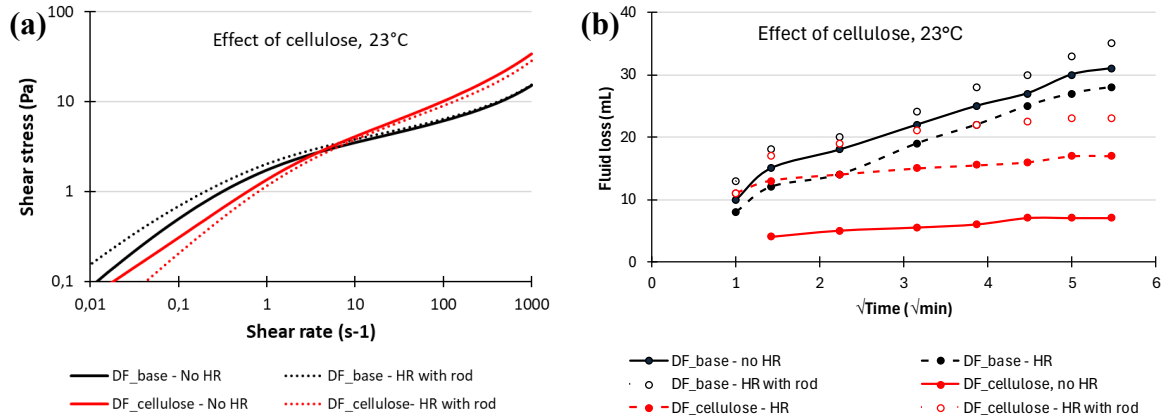

FIGURE 3: Effect of cellulose on (a) the flow curve and (b) the fluid loss curve of the drilling fluids, at 23°C.

The cellulose fibers also have a major impact on the fluid loss curves. It is known that the addition of fibers in a drilling fluids reduces the fluid loss and makes it easier to close the large pores in the rock formation[3,4]. This effect can clearly be seen in **FIGURE 3** (b), where the fluid loss is about 30 mL without cellulose after 30 min, while it is no more than 8 mL with cellulose. We can note that the hot rolling and mechanical shear with rod both reduce the efficiency of cellulose fibers. The fluid loss reaches 23 mL for DF_cellulose after hot rolling with rod. This shows that high temperature and mechanical shear damage the cellulose fibers. This observation is in accordance with previous tests which investigated the crack sealing ability of drilling fluids[2], where the sealing ability decreased when hot rolling was performed with a rod compared to hot rolling without rod. Experiments with DF_cellulose performed at 50°C showed no difference in fluid loss without hot rolling, but fluid loss much higher than DF_base in the case of hot rolling (results not shown here). This confirms that the cellulose fibers tend to be damaged by high temperature.

The mass of the filter cakes obtained from DF-cellulose were consistently lower than the filter cakes obtained from DF_base, on average 7,9 g. A large variation could however be observed in the dry mass of filter cakes obtained with cellulose. For instance, the experiment at 23°C without hot rolling, gave a filter cake dry mass of 4.3 g.

Effect of glycol

In **FIGURE 4** we investigate how MEG affects the fluid properties. Both DF_cellulose and DF_MEG contain cellulose. The difference in composition is that in DF_MEG, water is partially replaced by monoethylene glycol. Just one set of experiments has been performed, without hot rolling and with test temperature 50°C. Both flow curves and fluid loss curves show no difference between the fluids. This shows that MEG has no effect on these properties.

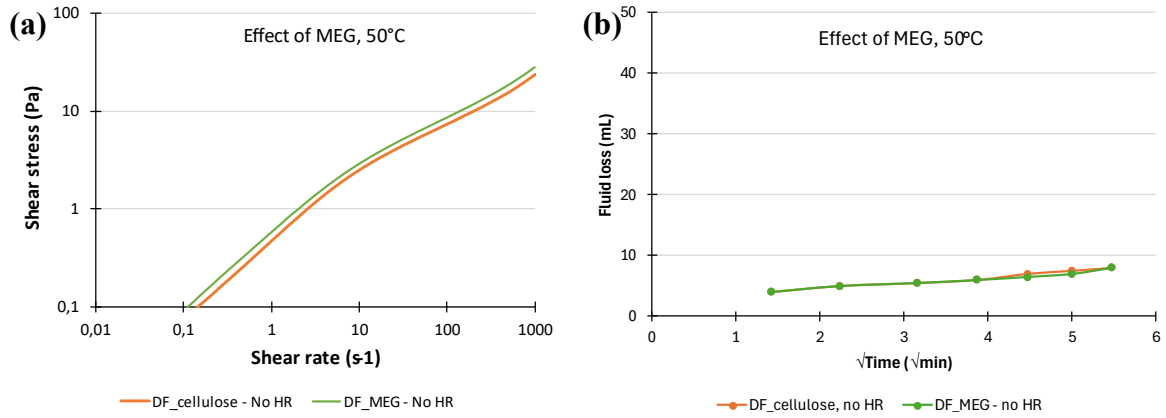

FIGURE 4: Effect of MEG on (a) the flow curve and (b) the fluid loss curve of the drilling fluids, at 50°C.

Replacement of Xanthan gum by PEEK

Finally, we investigate the effect of the polymer on the measured fluid properties (with cellulose). Xanthan gum is a common polymer used in water-based drilling fluids. PEEK, on the other hand, is not commonly used in drilling fluids. We have performed experiments to investigate whether it could be used to replace Xanthan gum for CO2 well applications.

The flow curves in **FIGURE 5** (a) show that the sulfonated PEEK results in drilling fluids with much lower viscosity than the xanthan gum. Note that this may reduce the fluid's ability to suspend and transport particles (weight particles and cuttings). This effect is not the object of this study.

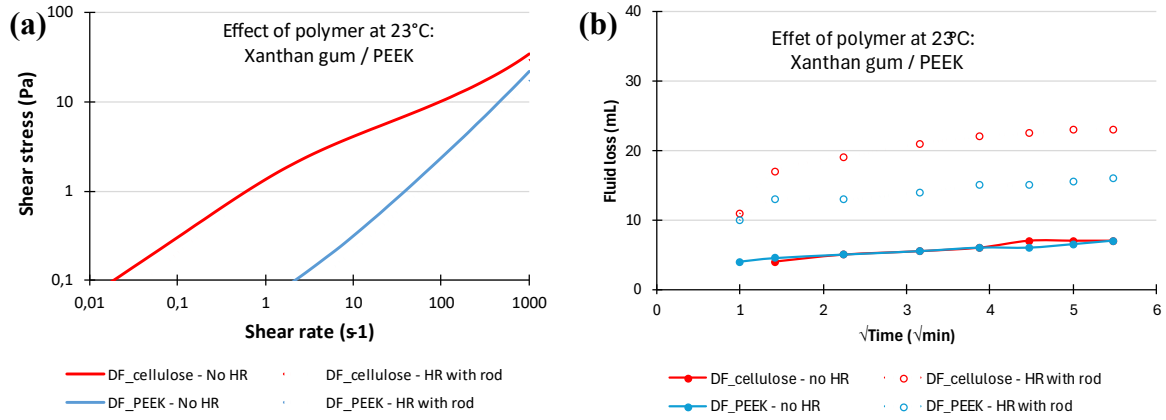

FIGURE 5: Comparison of (a) flow curves and (b) fluid loss curves for drilling fluids prepared from two different polymers.

On the other hand, fluid loss curves are very similar between the fluid with Xanthan gum (DF_cellulose) and the fluid with PEEK (DF_PEEK) without hot rolling. After rot rolling with rod, DF_PEEK had a lower fluid loss, which may indicate a good temperature stability of the PEEK. This should be confirmed by further experiments.

MODELLING OF FILTER CAKE FORMATION

During drilling a filter cake builds up on the inner cylindrical surface of the borehole wall as particles deposit on the surface while fluid (termed filtrate) flows into the porous formation. At the same time, the axial flow of drilling fluid circulating in the well causes erosion of the filter cake. This process is therefore a dynamic, radial filter cake buildup. If there is no axial flow the process is termed static, and if the geometry is planar, as in a laboratory filterpress, the process is termed linear. The latter is also a suitable approximation if the thickness of the filter cake is small relative to the wellbore radius. Civan[5] presents models for this process with both constant pressure difference and constant rate conditions. Here we use the model for static, linear filter cake buildup at constant Δp to analyze some of the results presented above from filterpress experiments with water-based drilling fluid. Civan presented this model as

$$Q(t) = \frac{q_0}{\hat{A}u_0^2}\left[\sqrt{1+2\hat{A}u_0^2 t}-1\right] = \frac{a}{\hat{A}u_0}\left[\sqrt{1+2\hat{A}u_0^2 t}-1\right] \tag{1}$$

where $Q(t)$ is the cumulative filtrate volume versus time t, a is the effective area of the porous disk, q_0 = a*u_0 is the initial volumetric filtrate flow rate and $\hat{A}$ is given by

$$\hat{A} = \frac{K_f k_d c_p}{\rho_p\left(1-\phi_c\right)K_c u_0 L_f} \tag{2}$$

Here, K_f and K_c are the permeabilities of the porous disk and the filter cake, respectively, k_d is a dimensionless constant of order unity representing the particle deposition rate of particles onto the filter cake, c_p is the mass concentration of particles in the drilling fluid, ρ_p is the mass density of these particles, ϕ_c is the filter cake porosity and L_f is the thickness of the porous disk. See **TABLE 2** for list of symbols.

While we do not know the permeability of the porous disk, it can be estimated using the Kozeny-Carman relation, given by [6]

$$K_f = \frac{\phi_f^3 d_f^2}{180\left(1-\phi_f\right)^2} \tag{3}$$

This gives a permeability of 3.65 darcy. The effective area a of the porous disk is

$$a = \frac{\pi D_{f,eff}^2}{4} \tag{4}$$

The model presented above neglects the spurt loss volume. We account for this ad hoc by neglecting the flow time for this volume. The resulting model is thus

$$Q(t) = \frac{a}{\hat{A}u_0}\left[\sqrt{1+2\hat{A}u_0^2 t}-1\right] + Q_{sl} \tag{5}$$

At short times, i.e. for

$$t << \tau \equiv \frac{1}{2\hat{A}u_0^2} \tag{6}$$

we have

$$\lim_{t\to 0}\frac{Q(t)-Q_{sl}}{t} = au_0 = q_0 = \frac{\Delta p a K_f}{\mu L_f} \tag{7}$$

where we have assumed flow according to Darcy's law. Assuming (or defining) $Q(t=0) = Q_{sl}$ we can estimate q_0 as

$$q_0 = \frac{Q(t_1) - Q_{sl}}{t_1} \tag{8}$$

Asymptotically at large times $t >> \tau$ we have

$$Q(t) - Q_{sl} = \frac{a}{\hat{A}u_0}\left[\sqrt{1 + 2\hat{A}u_0^2 t} - 1\right] \approx \frac{a}{\hat{A}u_0}\sqrt{2\hat{A}u_0^2 t} = a\sqrt{\frac{2}{\hat{A}}}\sqrt{t} \tag{9}$$

Thus, the model predicts that Q plotted versus the square root of time should produce straight lines asymptotically at large times, and from this slope we can calculate the filter cake permeability.

The following approximations are made:

1. Instantaneous spurt loss volume
2. Incompressible mudcake
3. No deposition of particles inside permeable disk
4. No deposition of particles inside filter cake
5. Darcy flow

The validity of the first of these assumptions can be discussed by analyzing the initial part of the curve $Q(t)$. Assumption #2 can be questioned due to the large pressure difference over the filter cake. Qualitatively, we expect that compression of the filter cake will reduce the porosity and thus the permeability of the filter cake and thus that the filtrate flow volume will increase more slowly than indicated by eq. (1). Since the permeable disk is covered by a filter paper with small pore size (11 µm), assumption #3 appears reasonable. Assumption #4 can be argued valid provided that the particles are of uniform size. In the base fluid (DF base) this is the case. For the other fluids the validity of this assumption can be questioned due to the presence of cellulose fibers. The validity of Darcy flow can be checked by calculating the Reynolds number based on the initial flow velocity u_0, viscosity μ, porosity ϕ_f, and pore size d_f of the porous disk. The viscosity is here the effective viscosity of the filtrate at representative shear rate for flow inside the porous disk. Thus, the viscosity cannot generally be inferred from the flow curves presented above, since the filtrate by assumption does not contain particles. In addition, we expect that some of the polymers are retained by the filter cake. However, we can still estimate the viscosity from eq. (7) once the initial flow rate q_0 is determined.

We apply the model presented above to the fluid DF base. It contains only one species of particles (barite) and is most likely to adhere to the assumptions presented above.
By regression using the model presented above we can in principle estimate values for initial filtrate flow velocity u_0, effective viscosity μ, and filter cake permeability K_c. Since the time resolution of the experimental data for $Q(t)$ is relatively coarse, the application to experimental data here is mainly to illustrate the principles.
We determine the parameters u_0, μ, and K_c using three different methods:

1. Asymptotic analysis, first using eqs. (7)-(9) neglecting the spurt loss and then calculating the spurt loss Q_{sl} as the difference between the experimental and modelled filtrate volume at the first non-zero time step.
2. By least square non-linear regression of eq. (5) using u_0, $\hat{A}u_0$, and Q_{sl} as fitting parameters
3. Subtract the spurt loss Q_{sl} calculated from method 1, and then apply least square non-linear regression of eq. (5) using u_0 and $\hat{A}u_0$ as fitting parameters.

Results from the regression analysis are shown in **TABLE 3**. We notice that there is a significant difference between the results from Method 1 (using asymptotic analysis) on the one side and Methods 2&3 (using least square fit) on the other side, for all results except the spurt loss. For all the models the viscosity μ is given by the velocity u_0 by eq. (7). We can argue which combination of μ and u_0 is most correct by considering the flow curve for this fluid, see **FIGURE 2**. The shear rate in the porous disk can be estimated as

$$\gamma = \frac{u_0 / \phi_f}{d_f} \tag{10}$$

From method 1 we obtain $\gamma = 2.5$ s^{-1} for method 1 and 1600-1700 for methods 2 and 3.
The actual viscosity of the filtrate is expected to be lower than indicated by **FIGURE 2** due to loss of particles and possibly also polymers. However, from **FIGURE 2** we obtain a viscosity of about 1.0 Pa*s at $\gamma = 2.5$ s^{-1} and 0.015 Pa*s at $\gamma = 1000$ s^{-1} (highest shear rate measured). Since the viscosity values of the filtrate should be lower than this, we conclude that all three methods overestimate the viscosity. This in turn means that the permeability K_f of the porous disk most likely is overestimated. From eq. (2) we see that then also the filter cake permeability is overestimated in this static linear model. To be able to conclude on which of the methods used here produce the most correct results, one would need more accurate experimental data on spurt loss volume and the corresponding time when this volume has been produced (spurt loss time t_{sl}). The three methods give t_{sl} = 40 s, 0.07 s, and 0.06 s, respectively.
Overall, we note that the cumulative filtrate volume is roughly linear in square root of time at large times, indicating the validity of the model. However, the time resolution is too low, in particular at short times, to produce more reliable data. Also, the accuracy of the filtrate volume is relatively low, on the order of 1 ml.
For all three methods we find that the filter cake permeability is much lower than the permeability of the porous disk and is of order 0.025 to 5.0E^{-5} darcy.

TABLE 2. List of symbols for filter cake formation modelling

Symbol	Description	Typical or default value
c_p	Mass concentration of particles in slurry	263 kg/m^3
d_f	Pore size in porous disk	90 µm
D_f	Diameter of porous disk	63.5 mm
$D_{f,eff}$	Effective diameter of porous disk (in contact with fluid)	53 mm
K_c	Permeability of filter cake	
k_d	Particle deposition rate coefficient	1
K_f	Permeability of porous disk	3.65 darcy
L_f	Length (thickness) of porous disk	6.5 mm
Q	Cumulative filtrate volume	
Q_{sl}	Spurt loss	
q_0	Initial filtrate flow rate	
Δp	Applied pressure difference	35 bar
ϕ_c	Porosity of filter cake	
ϕ_f	Porosity of porous disk	0.33
ρ_p	Mass density of particles in slurry	4200 kg/m3

TABLE 3. Results from regression analysis of filter cake model for fluid DF_base, no hot rolling, 23 °C.

Method	u_0	μ	Q_{sl}	K_c
	m/s	Pa*s	ml	darcy
1	7.6E-5	25.7	6.7	0.025
2	0.048	0.041	7.5	5.0E-5
3	0.053	0.037	6.7	4.5E-5

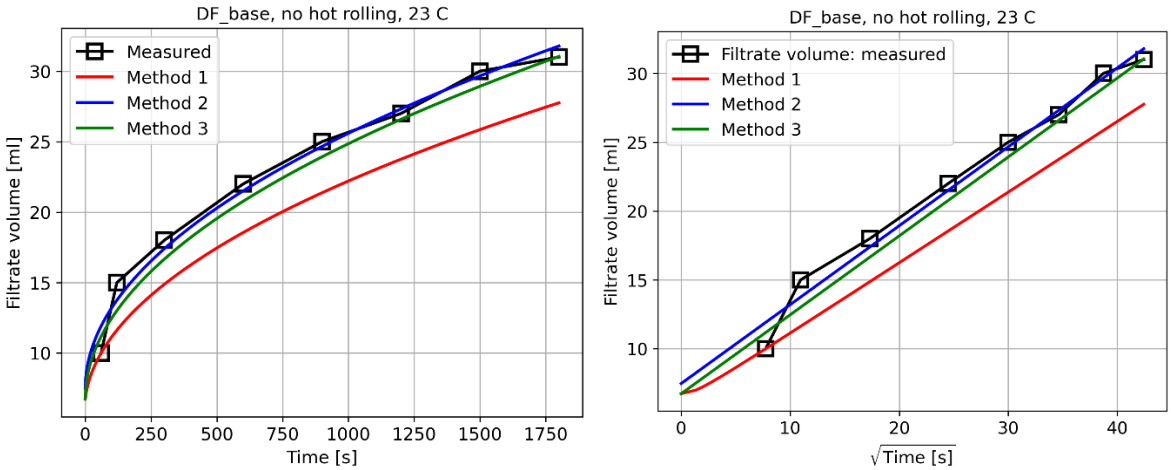

FIGURE 6. Measured and modelled filtrate volume as function of time (left) and square root of time (right) for fluid DF_base (no hot rolling, 23 °C).

CONCLUSIONS

We have measured experimentally the rheological and fluid loss properties of different water-based drilling fluids. We have also compared the fluid loss data with a static linear model and estimated physical parameters including filter cake permeability. The following observations have been made:

- The cellulose fibers increased the high shear rate viscosity and decreased the low shear rate viscosity of the drilling fluid. They reduced efficiently the fluid loss at room temperature but were easily damaged by mechanical shear and high temperatures.
- Replacement of a small quantity (3%) of water by monoethylene glycol (MEG) did neither affect the flow curve nor the fluid loss properties.
- Replacement of Xanthan gum by sulfonated PEEK strongly reduced the effective viscosity but seems slightly beneficial to fluid loss properties.
- The cumulative filtrate volume increases as the square root of time, indicating the validity of the static, linear filter cake buildup model for the setup used here.
- The permeability of the filter cake is significantly lower than the permeability of the porous disk.

ACKNOWLEDGEMENTS

The work was funded by SINTEF through the projects "*SEP Filter cake optimization for CCS wells*" and "*SEP Injectivity in CO_2 wells*". The authors also thank SLB for kindly providing components to prepare the fluids.

REFERENCES

(1) Skogestad, J. O.; Feneuil, B.; N'Gouamba, E.; Linga, H.; Aasen, A.; Skår, G.; Roggeband, S. M.; Nedrum, J.; Helgeland, S. CCS Well Control Impact of CO2 on Drilling Fluid Performance. In *IADC/SPE International Drilling Conference and Exhibition*; SPE: Galveston, Texas, USA, 2024; p D021S018R004. https://doi.org/10.2118/217711-MS.

(2) Klungtvedt, K. R.; Saasen, A. Comparison of Lost Circulation Material Sealing Effectiveness in Water-Based and Oil-Based Drilling Fluids and Under Conditions of Mechanical Shear and High Differential Pressures. *Journal of Energy Resources Technology* **2022**, *144* (12), 123011. https://doi.org/10.1115/1.4054653.

(3) Saasen, A.; Hodne, H.; Ronæs, E.; Aarskog, S. A.; Hetland, B.; Løvereide, M. B.; Mohammadi, R. Wood Fibre Based Lost Circulation Materials. In *ASME 2018 37th International Conference on Ocean, Offshore and Arctic EngineeringArctic Sciences and Technology; Petroleum Technology*; American Society of Mechanical Engineers: Madrid, Spain, 2018; p V008T11A062. https://doi.org/10.1115/OMAE2018-77662.

(4) Klungtvedt, K. R.; Saasen, A. A Method for Assessing Drilling Fluid Induced Formation Damage in Permeable Formations Using Ceramic Discs. *Journal of Petroleum Science and Engineering* **2022**, *213*, 110324. https://doi.org/10.1016/j.petrol.2022.110324.

(5) Civan, F. *Reservoir Formation Damage: Fundamentals, Modeling, Assessment, and Mitigation*, Fourth edition.; Gulf Professional Publishing, 2023. https://doi.org/10.1016/B978-0-323-90228-1.00034-0.

(6) Rehman, M.; Hafeez, M. B.; Krawczuk, M. A Comprehensive Review: Applications of the Kozeny–Carman Model in Engineering with Permeability Dynamics. *Archives of Computational Methods in Engineering* **2024**, *31* (7), 3843–3855. https://doi.org/10.1007/s11831-024-10094-7.

Non-Newtonian Fluid Mechanics

MODELING AND SIMULATION OF NON-NEWTONIAN FLUID FLOW USING COMSOL MULTIPHYSICS®

Galina Shugai

COMSOL AB, 111 40 Stockholm, Sweden

ABSTRACT

This paper presents an overview of the capabilities of COMSOL Multiphysics® for simulating non-Newtonian fluids, with an emphasis on multiphysics. It outlines the COMSOL implementation of inelastic and viscoelastic non-Newtonian fluid models and reviews the software's ability to couple fluid flow with heat transfer, structural deformation, and multiphase flow modeling.

FLUID FLOW MODELING

COMSOL Multiphysics is a finite element-based simulation software designed for modeling and solving physical problems involving processes such as fluid flow, heat transfer, and structural deformation. Starting from individual physics, it is possible to combine multiple physical phenomena in the COMSOL environment to simulate real-world behavior. COMSOL includes several interfaces specifically tailored for simulating flows with complex rheological behavior.

Fluid motion can be described using simplified mathematical models or engineering correlations for specific cases. However, the most comprehensive description is based on fundamental conservation laws: the continuity equation for mass conservation and the Navier–Stokes equations for momentum conservation:

$$\frac{\partial \rho}{\partial t} + \nabla \cdot (\rho \mathbf{u}) = 0 \tag{1}$$

$$\rho \left(\frac{\partial \mathbf{u}}{\partial t} + \mathbf{u} \cdot \nabla \mathbf{u} \right) = -\nabla p + \nabla \cdot \tau + \mathbf{f}, \tag{2}$$

where $\mathbf{u}$ is the velocity field, p is the pressure, ρ is the fluid density, τ is the stress tensor, and $\mathbf{f}$ is the body force (e.g., gravity).

Inelastic non-Newtonian models

Solving momentum conservation equations requires specifying the rheological behavior of the fluid through the stress tensor τ, which must be defined by a suitable constitutive

equation. For an incompressible Newtonian fluid, the stress tensor can be written as

$$\tau = 2\mu\mathbf{D},\ \mathbf{D} = \frac{1}{2}\left(\nabla\mathbf{u} + (\nabla\mathbf{u})^{\top}\right), \tag{3}$$

where μ is the viscosity.

However, many fluids deviate from this simple relationship. COMSOL provides a comprehensive suite of built-in constitutive models for both inelastic and viscoelastic behaviors. Inelastic non-Newtonian models typically follow the form of Eq. 3, but with viscosity replaced by an apparent viscosity, often calculated from the shear rate $\dot{\gamma} = \sqrt{2\mathbf{D} : \mathbf{D}}$. These models fall into two broad categories: those with yield stress behavior (viscoplastic) and those without. For fluids without yield stress behavior, COMSOL includes models such as the Power Law:

$$\mu = m(\max(\dot{\gamma}, \dot{\gamma}_{\min}))^{n-1} \tag{4}$$

where m and n are scalars. For $n > 1$, the fluid is shear thickening (dilatant); for $n < 1$, shear thinning (pseudoplastic); and $n = 1$ corresponds to a Newtonian fluid. The lower bound for the share rate $\dot{\gamma}_{\min}$ is introduced to avoid infinite viscosity at zero shear rate when $n < 1$.

The Ellis and Sisko models offer enhanced accuracy in different regimes. The Ellis model is a three-parameter model that is usually better than the power-law in matching experimental measurements in low and medium shear-rate regimes. The Sisko model includes both the power law region and an infinite shear plateau.

The Carreau–Yasuda model can be described by the equation

$$\mu = \mu_{\infty} + (\mu_0 - \mu_{\infty})\left[1 + (\lambda\dot{\gamma})^a\right]^{\frac{n-1}{a}} \tag{5}$$

where λ is the time constant, μ_0 is the zero-shear viscosity, μ_{∞} is the infinite-shear viscosity, and a is the transition parameter. Eq. 5 allows the recovery of the Carreau, Cross, and Cross-Williamson models through specific parameter choices.

Viscoplastic fluid behavior is characterized by the existence of a yield stress, denoted as τ_y, a threshold that must be exceeded before significant deformation occurs. Constitutive models for such fluids include this yield stress, which introduces numerical challenges due to the inherent discontinuity. To address these challenges, the Papanastasiou regularization method[2] is employed in COMSOL, thus enabling the modeling of both yielded and unyielded regions in a continuous manner. Five models for fluids exhibiting yield stress behavior are available: Bingham, Herschel–Bulkley, Casson, DeKee–Turcotte, and Robertson–Stiff. For example, the Bingham plastic model with Papanastasiou regularization is expressed as:

$$\tau = \tau_y\left(1 - e^{-m\dot{\gamma}}\right) + \mu_p\dot{\gamma} \tag{6}$$

where μ_p is the plastic viscosity, and m is a regularization parameter that controls the sharpness of the transition between unyielded and yielded behavior.

COMSOL also offers the Houska model, a viscoplastic constitutive model. It extends the Bingham plastic model by incorporating a shear-rate-dependent viscosity, allowing it to better represent complex flow characteristics of structured fluids such as suspensions and pastes. The model is particularly useful in capturing thixotropic behavior and structural recovery in time-dependent non-Newtonian fluids.

The predefined models can be extended or customized using the equation-based modeling tools to implement user-defined constitutive relations, time-dependent viscosity functions, or microstructural evolution equations relevant to thixotropic and viscoplastic materials.

In COMSOL, it is possible to model the flow of non-Newtonian fluids through porous media using the concept of an apparent shear rate. This quantity represents the equivalent shear rate that would produce the same pressure drop in a porous medium as in a free-flow scenario for a given non-Newtonian fluid. The apparent shear rate is expressed as:

$$\dot{\gamma}_{\text{app}} = \alpha \frac{|\mathbf{u}|}{\sqrt{\kappa \varepsilon_{\text{p}}}} \tag{7}$$

where α is a correction factor that depends on the porous structure, κ is the permeability, and ε_{p} is the porosity of the medium. The value of α is not universal; it must be determined experimentally or estimated using pore-scale simulations.

Viscoelastic models

To model viscoelastic effects, the stress tensor is expressed as the sum of a viscous and an elastic contribution:

$$\tau = 2\mu_{\text{S}}\mathbf{D} + \mathbf{T}_e, \tag{8}$$

where $\mathbf{T}_e$ is the elastic (or viscoelastic) stress tensor which is often represented as a sum of the individual modes: $\mathbf{T}_e = \sum_m \mathbf{T}_{e_m}$. The multimode formulation provides a more accurate description of the rheological behavior of fluids with a spectrum of relaxation times typically resulting from the polydispersity of macromolecules.

To complete the system of equations, a constitutive relation must be specified for each mode. Only differential constitutive models are available in COMSOL. These models can be formulated in different ways, depending on the choice of dependent variables. In a stress formulation, the extra stress tensor is the primary dependent variable. Alternatively, in a conformation formulation, an intermediate structural variable—the conformation tensor $\mathbf{C}$—is used, with the stress determined as an explicit function of $\mathbf{C}$.

Several commonly used constitutive models can be expressed as hyperbolic partial differential transport equations in the stress formulation[1]:

$$\mathcal{U}(\mathbf{T}_e) + \mathbf{f}_{\text{r}}(\mathbf{T}_e) = \frac{\mu_e}{\lambda_e}\mathbf{f}_{\text{p}}(\mathbf{T}_e) \tag{9}$$

Here, $\mathbf{f}_{\text{r}}$ and $\mathbf{f}_{\text{p}}$ are model-specific functions representing relaxation and viscous effects, respectively, λ_e is the relaxation time, and μ_e denotes the elastic viscosity. The function $\mathcal{U}(\mathbf{T})$ is the upper-convected derivative:

$$\mathcal{U}(\mathbf{T}_e) = \frac{\partial \mathbf{T}_e}{\partial t} + \mathbf{u} \cdot \nabla \mathbf{T}_e - \left(\nabla \mathbf{u} \cdot \mathbf{T}_e + \mathbf{T}_e \cdot \nabla \mathbf{u}^T\right) \tag{10}$$

This derivative is essential in viscoelastic fluid modeling because it ensures objectivity (frame-independence) of the constitutive equations. In other words, the stress response predicted by the model remains consistent under arbitrary rigid body motions of the coordinate system.

The Oldroyd-B model is one of the simplest constitutive models for viscoelastic fluids, representing a suspension of Hookean springs in a Newtonian solvent with $\mathbf{f}_{\text{r}} = \mathbf{T_e}$ and $\mathbf{f}_{\text{p}} = 1$. Building on this foundation, more advanced models have been developed to capture the complex structural behavior of polymeric fluids. These next-generation models incorporate the concept of networks formed by interacting polymer macromolecules, enabling the continuum-based modeling of polymer melts and concentrated solutions. Additionally to the Oldroyd-B model, COMSOL offers the Giesekus model that includes

quadratic nonlinearity due to hydrodynamic drag between polymers, the FENE-P and FENE-CR models with finitely extensible nonlinear elastic (FENE) springs to limit chain extensibility. The LPTT and EPTT models account for network elasticity to resist deformation, improving stability in extensional flows, and the finally Rolie-Poly model that is derived based on tube theory, capturing reptation, chain stretching, and convective constraint release.

The Weissenberg number, Wi, is a dimensionless number that characterizes the relative importance of elastic effects in a flowing viscoelastic fluid $Wi = \lambda_e \dot{\gamma}$ where $\dot{\gamma}$ is the characteristic shear rate. A high Weissenberg number indicates that elastic effects dominate over viscous effects in the flow. In this regime, the elastic stresses can grow rapidly, which can lead to convergence issues or unphysical results. This problem is particularly severe in geometries with sharp corners and in flows with strong extensional components. Overcoming high Weissenberg number problems requires careful numerical stabilization and sometimes simplified modeling approaches.

MULTIPHYSICS COUPLINGS INVOLVING NON-NEWTONIAN FLUIDS

One of the major advantages of using COMSOL is its seamless integration of multiphysics: non-Newtonian fluid flow can easily be coupled with other physical processes in the same model. This is particularly important for complex fluids, whose behavior often depend on temperature, chemical composition, or interactions with solid structures.

Non-isothermal flow modeling

Modeling non-isothermal flow is essential in many industrial applications involving non-Newtonian fluids, because of the strong coupling between the flow, stress, and thermal fields, which significantly affect the material response. COMSOL addresses these problem through the Non-Isothermal Flow multiphysics interface, which couples the fluid flow equations with the heat transfer equations. The heat transfer equation is expressed as:

$$\rho C_p \left(\frac{\partial T}{\partial t} + \mathbf{u} \cdot \nabla T \right) = k \nabla^2 T + Q \tag{11}$$

where ρ is the fluid density, C_p is the specific heat capacity, k is the thermal conductivity, and Q is the internal heat source term. The Nonisothermal Flow interface is pre-configured to include the heat source Q that includes several contributions:

$$Q = 2\mu_{\mathrm{S}} \mathbf{D} : \mathbf{D} + \alpha\, \mathbf{T}_e : \mathbf{D} + (1 - \alpha) \frac{\mathrm{tr}(\mathbf{T}_e)}{2\lambda_e(T)} \tag{12}$$

The first term represents viscous heating, that is present in both Newtonian and non-Newtonian fluids. For viscoelastic flows, the internal heat generation includes an irreversible dissipation term and a reversible component. In COMSOL, the reversible part is neglected ($\alpha = 1$).

Heating generally reduces viscosity due to increased molecular mobility. As temperature rises, polymer chains or molecular segments move more freely, leading to a decrease

in flow resistance. This temperature-dependent behavior is modeled in COMSOL Multiphysics using thermal functions:

$$\frac{\mu_s(T)}{\mu_s(T_0)} = \alpha_T(T) \tag{13}$$

For viscoelastic flows, it is assumed that both the relaxation time and elastic viscosity vary with temperature:

$$\frac{\mu_e(T)}{\mu_e(T_0)} = \frac{\lambda_e(T)}{\lambda_e(T_0)} = \alpha_T(T) \tag{14}$$

where $\alpha_T(T)$ is a temperature-dependent scaling function. Several thermal function models are available, including Arrhenius, WLF (Williams–Landel–Ferry), exponential forms, and user-defined functions.

Chemorheology

In many industrial applications involving non-Newtonian fluids—such as thermoset polymers, adhesives, and resins—viscosity is highly dependent on both temperature and the degree of cure. As curing progresses, chemical cross-linking between polymer chains restricts molecular motion, leading to a significant rise in viscosity. In the later stages, the system may undergo gelation, where viscosity increases dramatically.
This rise in viscosity can enhance viscous heating, which in turn raises the local temperature and further accelerates the curing process. The resulting interplay between thermal effects, curing kinetics, and viscous dissipation produces a highly nonlinear and tightly coupled behavior in the viscosity field.
Accurate simulation of such systems requires the simultaneous solution of the flow, heat transfer, and curing. The curing process is typically modeled using temperature-dependent reaction kinetics, where the degree of cure, c, evolves over time. A common form of the cure-kinetics equation is:

$$\frac{\partial c}{\partial t} + \mathbf{u} \cdot \nabla c = R(T, c) \tag{15}$$

Available reaction models include the Sestak–Berggren, Kamal–Sourour, and n-th order. To capture the sharp increase in viscosity during the curing of thermosetting polymers—particularly when the polymer network is close to gelation—the Castro–Macosko and percolation-based viscosity models are included.

Curing reactions are typically exothermic, releasing heat as crosslinking progresses:

$$Q_{\mathrm{r}} = H_r \frac{d\alpha}{dt} \tag{16}$$

where H_r is the total heat of reaction. COMSOL provides a dedicated coupling that automatically incorporates this source term into the heat transfer equation (Eq. 11).

Fluid–Structure Interaction

Fluid–Structure Interaction (FSI) refers to coupling fluid flow with solid mechanics so that a deformable structure and the fluid mutually influence each other. COMSOL supports fully coupled FSI simulations even for non-Newtonian fluids. For example, one could simulate the flow of an inelastic or a viscoelastic fluid flowing through an elastic tube, capturing how the fluid pressure deforms the structure and how that deformation in turn alters the flow.

Multiphase Flow and Free Surfaces

Many non-Newtonian fluid applications—such as coating, mold filling, and extrusion—involve free surfaces or multiphase flows. COMSOL provides several methods for simulating two-phase or multiphase flows with interface tracking, including the Level Set, Phase Field, and Moving Mesh (ALE) approaches. These methods can be directly coupled with non-Newtonian fluid models using predefined two-phase flow multiphysics couplings.

The beads-on-string structure is a phenomenon observed in thinning viscoelastic filaments, surface tension and elastic stresses cause the filament to form droplet-like beads connected by thin threads. It is a classic example that is used to verify numerical simulations. The problem is solved in COMSOL using the Oldroy B model and Moving Mesh (ALE) functionality. **Fig. 1** shows the evolution of the filament at different times. The results are in good agreement with the experimental and simulation results presented in other publications[3].

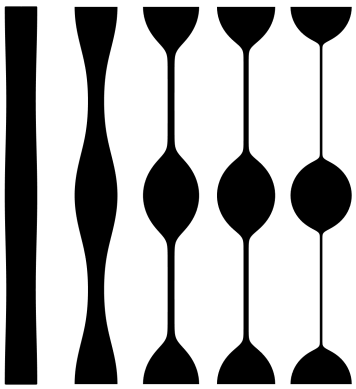

FIGURE 1: Filament profiles at 5 different dimensionless times: 0, 20, 30, 100, and 300

The next example illustrates the filling stage of an injection molding process. Molten polymer is injected into the top of a heated mold initially filled with air. The curing reaction is modeled using the Kamal–Sourour model, while the viscosity's dependence on the degree of cure is described by the Castro–Macosko model. Shear rate dependence is captured using a power-law formulation. **Figure 2** shows the distribution of viscosity and the degree of cure, along with the position of the interface between the air and the polymer melt. The problem is solved using two-phase flow with phase field coupling, non-isothermal flow, and curing reaction heat coupling.

In conclusion, the COMSOL Multiphysics simulation software is a practical tool for modeling coupled problems involving non-Newtonian fluid flow. It supports a range of non-Newtonian constitutive models and allows for the integration of flow with thermal, chemical, and structural effects. Built-in methods for handling free-surface and multiphase flows further extend its applicability. These features make it suitable for simulating processes such as polymer curing, coating, and biomedical flows, where complex rheological behavior and multiphysics interactions are significant.

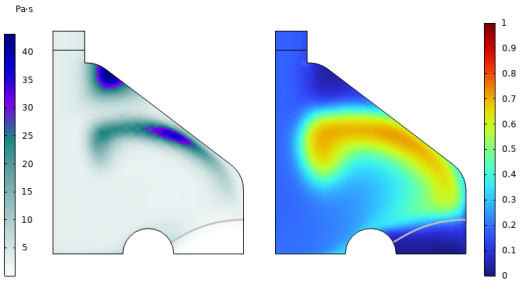

FIGURE 2: Viscosity (left) and degree of cure (right)

REFERENCES

1. Bird R.B., Stewart W.E. and Lighfoot E.N. *Transport Phenomena*, John Wiley, New York, Book Publication, 1960.

2. Papanastasiou T.C Flow of materials with yield *J.Rheol*,**31**, 385–404, 1987.

3. Clasen C., Eggers J., Fontelos M.A, Li J., McKinley G. The beads-on-string structure of viscoelastic threads *J. Fluid Mech.*, **556**, 283–308, 2006.

4. COMSOL Multiphysics, Version 6.3, including the Polymer Flow Module, 2025.

Poster Presentations

Stability Analysis of Rheology and Matting Paste in Coil Coatings Over Time and the Effects of Production Parameters

Ömer Gürçay

Kansai Altan Boya Sanayi ve Ticaret A.Ş. Kemalpaşa OSB Mah. İzmir Ankara Yolu (Ansızca) Küme Evleri No:286 - 35730 Kemalpaşa, İzmir

Author: Ömer Gürçay omer.gurcay@kansaialtan.com.tr

Abstract

This work examines the stability and viscosity issues encountered in the production and application of C0600972-coded Aerosil fumed silica paste. As a polyester- and melamine formaldehyde resin based this semi-product plays a crucial role in the coil coatings industry. The research focuses on variations in rheological behavior across different production batches, evaluating particle size effects, production processes, and stabilization stages..

Introduction

C0600972 aerosil paste significantly impacts pigment orientation in metallic topcoats. However, discrepancies in viscosity and rheological stability across different batches have posed challenges in maintaining consistent coating properties. This study aims to analyze the factors influencing these variations and propose process improvements.

Applications of C0600972:

- High Durable Polyester Topcoat
- Flexible High Durable Polyester Topcoat
- Polyurethane Base Coat

Problem Definition

Batch Variations

- Observed inconsistencies in viscosity and rheological behavior between different production batches.
- Time-dependent changes in flow behavior.

Particle Size and Rheological Behavior

- Target particle fineness limit: 12.5 µm.
- Some batches recorded particle sizes between 60-70 µm, indicating instability.
- Particle agglomeration during storage reduces rheological performance.

Test Results

- Viscosity increased significantly between days 11 and 18, stabilizing afterward.
- Optimal stabilization observed from day 18 onward.
- Comparative viscosity values are detailed in the following table.

Table 1: Viscosity Changes Over Time @ 0,1 shear rate

	1. Pass 0,1 s^{-1} SR Viskozite Ölçümleri		2. Pass 0,1 s^{-1} SR Viskozite Ölçümleri		3. Pass 0,1 s^{-1} SR Viskozite Ölçümleri		4. Pass 0,1 s^{-1} SR Viskozite Ölçümleri	
C0600972 2208342700	(cp)	% Change	(cp)	% Change	(cp)	% Change	(cp)	% Change
6.Gün	3510	-	2540	-	4130	-	5670	-
11. Gün	26200	646	20000	687	23800	476	30000	429
18. Gün	56300	115	39700	99	47000	97	56300	88
22. Gün	62600	11	47400	19	52700	12	61600	9
41. Gün	72400	16	64500	36	55100	5	71500	16

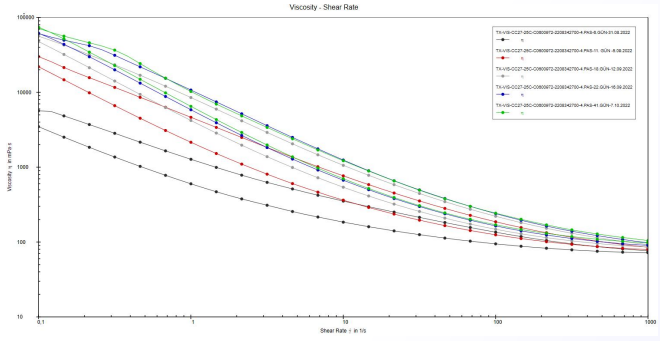

Figure 1: Viscosity Stability Over Time (Graph depicting viscosity fluctuations and stabilization period)

Influence of Milling Process and Bead Type
Effect of Bead Material

- Different milling beads were tested for efficiency.
  - Bead types: Zirconium (0.7-0.9 mm and 1.4-1.6 mm) and Glass (0.8-1,0 mm).

Table 2: Milling Bead Type and Impact on Particle Size

Samples	Batch	Bead Type	Bead Size (mm)	Mill Type	Additional Pass
C0600972 Premixing	**2408156300**	**Zirconium**	**0,7-0,9**	**Labstar LME**	**3**
C0600972 Premixing	**2408156300**	**Zirconium**	**1,4-1,6**	**Labstar LME**	**6**
C0600972 Production 1 Pass Dynomill	**2408196000**	**Zirconium**	**0,7-0,9**	**Labstar LME**	**2**
C0600972 Production 1 Pass Dynomill	**2408196000**	**Zirconium**	**1,4-1,6**	**Labstar LME**	**6**
C0600972 Production 1 Pass Dynomill	**2408196000**	**Glass**	**0,8-1,0**	**Labstar LME**	**1**

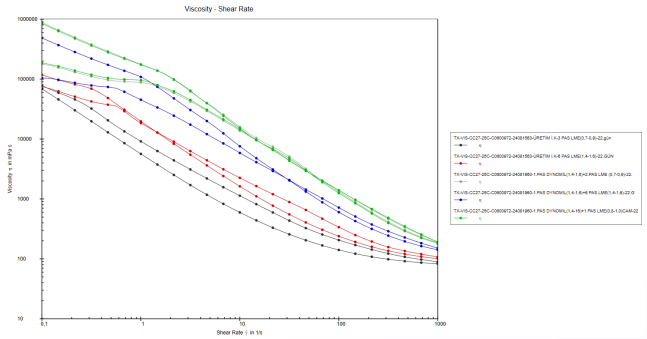

Figure 2: Bead Type vs. Milling Efficiency (Viscosity Graph displaying particle size reduction based on bead type)

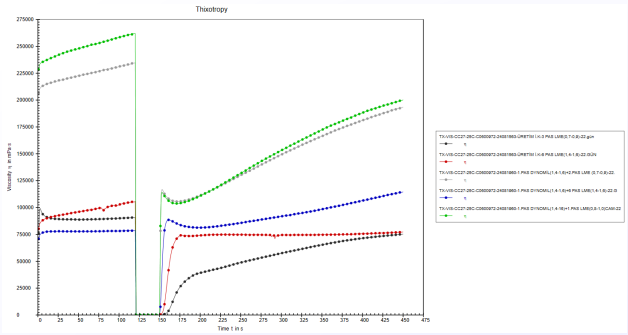

Figure 3: Bead Type vs. Milling Efficiency (Thixotropy Graph displaying particle size reduction based on bead type).

- Smaller beads improved grinding efficiency.
- Transitioning from larger to smaller beads led to more consistent particle sizes.

Future Research Recommendations

- Standardizing Process Parameters: Maintaining fixed mixing times and equipment settings.
- Initial Mixing (Premixing) Control: Ensuring initial milling produces consistent particle sizes before further processing.
- Enhanced Quality Control Measures: Regular viscosity and particle size checks to detect deviations earlier.

Conclusion

The research indicates that variations in production parameters significantly impact the rheological stability of C0600972 aerosil paste. By optimizing milling processes, adjusting bead materials, and standardizing production parameters, consistency in viscosity and overall product quality can be improved. These findings provide actionable insights for enhancing process reliability in coil coatings applications.

REFERENCES

Anton Paar, 2021, **"**The influence of particle on suspension rheology", https://wiki.anton-paar.com/tr-tr/partikuellerin-suespansiyon-reolojisiuezerindeki-etkisi/, (Access:15.09.2024)

Mezger, T. G., 2014, The Rheology Handbook, 4th Ed., Vincentz Network, Hanover, 31-42 pp

Thank you

We extend our gratitude to Kansai Altan Boya Sanayi ve Ticaret A.Ş. for their support throughout the study.

The influence of various forms of one-time physical activity in -5°C on the rheological properties of blood in young men

Aneta Teległów [1]*, Konrad Rembiasz [2], Janusz Pobędza [3], Jakub Marchewka [4], Zygmunt Dziechciowski [5], Andrzej Czerwiński [6], Jakub Leśniowski [7], Monika Świderska [8], Aleksandra Urban [9] and Piotr Mika [10]

[1] Department of Health Promotion, Faculty of Motor Rehabilitation, Bronislaw Czech University of Physical Culture in Krakow, 31-571 Krakow, Poland;aneta.teleglow@awf.krakow.pl
[2] Indoor Swimming Pool Complex, University of Physical Culture in Krakow, 31-571 Krakow, Poland;konrad.rembiasz@awf.krakow.pl
[3] Laboratory of Techno-Climatic Research and Heavy Duty Machines, Faculty of Mechanical Engineering, Cracow University of Technology, Jana Pawła, II 37, Krakow 31-864, Poland, janusz.pobedza@pk.edu.pl
[4] Department of Rehabilitation in Traumatology, Faculty of Motor Rehabilitation, Bronislaw Czech University of Physical Culture in Krakow,31-571 Krakow, Poland; jakub.marchewka@awf.krakow.pl
[5] Laboratory of Techno-Climatic Research and Heavy Duty Machines, Faculty of Mechanical Engineering, Cracow University of Technology, Jana Pawła, II 37, Krakow 31-864, Poland, z.dziechciowski@pk.edu.pl
[6] Laboratory of Techno-Climatic Research and Heavy Duty Machines, Faculty of Mechanical Engineering, Cracow University of Technology, Jana Pawła, II 37, Krakow 31-864, Poland, andrzej.czerwinski@pk.edu.pl
[7] Laboratory of Techno-Climatic Research and Heavy Duty Machines, Faculty of Mechanical Engineering, Cracow University of Technology, Jana Pawła, II 37, Krakow 31-864, Poland, jakub.lesniowski@pk.edu.pl
[8] Research & Development Department, Wimba Poland sp. Z. o. o., 31-553 Kraków; monikasw@poczta.onet.eu
[9] Medical Equipment Department, University Children's Hospital in Cracow, 30-663 Kraków, Poland; aurban1@usdk.pl
[10] Institute of Clinical Rehabilitation, Faculty of Motor Rehabilitation, Bronislaw Czech University of Physical Culture in Krakow, 31-571 Krakow, Poland; piotr.mika@awf.krakow.pl

ABSTRACT

Physical activity combined with low temperatures can improve physical fitness, the efficiency of many systems, as well as mental well-being. The aim of this study is to investigate the effects of single sessions of various forms of physical activity (running, walking, lying down) conducted in a thermoclimatic chamber at an air temperature of -5°C on the rheological properties of blood in young men.

INTRODUCTION

The study group (n=21) consisted of young men aged 22. The participants (empty stomach, after hydration with 500 ml of water) performed single sessions of various forms of physical activity at an air temperature of -5°C. The research was conducted in the thermoclimatic chamber of Laboratory of Techno-Climatic Research and Heavy Duty Machines (LBT&MR) located on the premises of the Cracow University of Technology (Poland). Blood samples were collected from the subjects before entering the thermoclimatic chamber and after leaving it (fasting, from the antecubital vein in the amount of 10 milliliters into Vacuette EDTA K2 tubes) by a qualified nurse.

Morphological and rheological indicators were determined in the tested blood at the Blood Physiology Laboratory of the University of Physical Education belonging to the Central Scientific and Research Laboratory. The study was approved by the Ethics Committee of the Regional Medical Chamber in Krakow, Poland (approval No.: 171/KBL/OIL/2023) and followed the tenets of the Declaration of Helsinki)

RESULTS

In our study, an increase in red blood cell deformability was observed in the thermoclimatic chamber at an air temperature of –5°C: at a shear stress of 2.19 Pa only between groups No. 2 walking before and after and at a shear stress of 4.24 Pa only between groups No. 1 jogging before and after, and between groups No. 2 walking before and after. For everyone single exercise an increase in red blood cell deformability was also recorded in the chamber at –5°C at a shear stress of 8.23 Pa, at a shear stress of 15.95 Pa, at a shear stress of 30.94 Pa, and at a shear stress of 60.00 Pa after running, walking, and lying down, compared with blood indicators measured before these forms of exercise (Fig. 1). It is likely that the increase in red blood cell deformability at higher shear stress levels serves as a mechanism to facilitate blood flow in men exposed to an air temperature of -5°C. The study of the rheological propeties of blood in a thermoclimatic chamber, where the air temperature was -5°C, reveals specific differences that can be used to combine cold therapy with physical exercise.

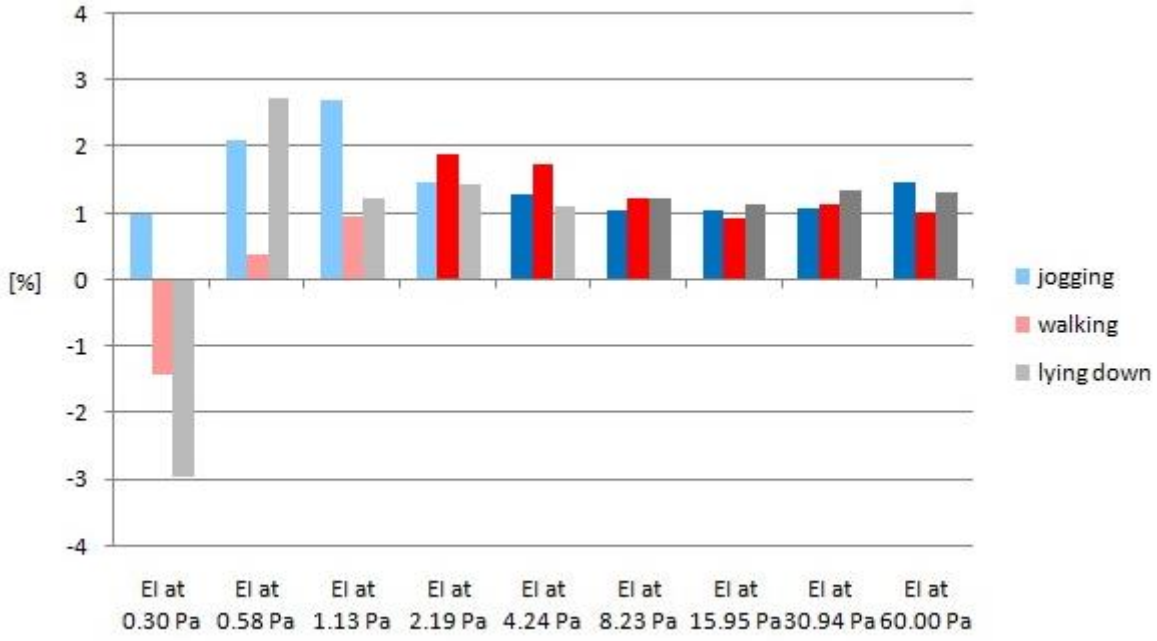

Figure 1. Elongation index (EI)–shear stress (SS) curves for RBC in studied groups. *p < 0.05.

The intervention applied among the subjects in the form of physical effort at a temperature of –5°C in the walking group best demonstrates the adaptation in young men in terms of blood rheological properties, as evidenced by a significant increase in red blood cell deformability.

REFERENCES:

1. Teległów, A.; Mirek, W.; Ptaszek, B.; Maciejczyk, M.; Godawska, D.; Marchewka, J.; Blood Morphological and Biochemical Indicator Characteristics in Men Performing Different Physical Activities in the Cold—A Preliminary Report. Life 2024, 14, 474; https://doi.org/10.3390/life14040474.

Index of contributors